# IDENTIFICATION AND CHARACTERIZATION OF GENES THAT REGULATE MITOCHONDRIAL DYNAMICS IN *CAENORHABDITIS ELEGANS*

By

NATHALY SALAZAR-VASQUEZ

A dissertation submitted to the

School of Graduate Studies

Rutgers, The State University of New Jersey

In partial fulfillment of the requirements

For the degree of

Doctor of Philosophy

Graduate Program in Microbiology and Molecular Genetics

Written under the direction of

Christopher Rongo, Ph.D.

And approved by

_____

_____

_____

_____

New Brunswick, New Jersey

OCTOBER, 2018

ABSTRACT OF THE DISSERTATION

Identification and Characterization of Genes that Regulate Mitochondrial Dynamics in *Caenorhabditis Elegans*

by NATHALY SALAZAR-VASQUEZ

Dissertation Director:

Christopher Rongo, Ph.D.

Mitochondria are essential organelles for eukaryotic cells, particularly for neurons, which have high-energy demands and do not store glycolytic reserves. Instead, neurons rely on mitochondrial oxidative phosphorylation to meet their energy demands. In addition to energy generation, mitochondria also mediate processes as diverse as sugar and fatty acid breakdown, steroid and lipid synthesis, calcium homeostasis, and apoptosis. Given the critical role of mitochondria in cellular physiology, mitochondrial dysfunction contributes to the etiology of multiple diseases and disorders.

Mitochondrial function is regulated by changes in organelle size, number, and morphology, and these mitochondrial dynamics are the result of the balanced processes of fission/fusion and mitophagy. In addition, mitochondria interact with various motor and adaptor proteins for mitochondrial transport within the cell, which is particularly important for meeting the energy needs of distal synapses in neurons. Fission, fusion, mitophagy and transport have been found to be fairly conserved across various organisms. Some of the genes that mediate these processes are known, but we do not fully understand how they are regulated, how they are coordinated with each other or

how these processes change in response to stress or age. Overall, much remains to be understood with respect to mitochondrial dynamics and transport, specifically in neurons.

In the following thesis work I used the model organism *Caenorhabditis elegans* to study mitochondria in neurons. I examined how the dynamics of fusion and fission are affected in response to oxygen deprivation. In addition, I performed a forward genetic screen to identify novel proteins that may play a role or regulate aspects of mitochondrial dynamics and transport in the neuron even under non-stress conditions. Through this screen, I found new alleles of a known player, DRP-1, in the fission pathway. I also identified two novel genes, MTX-2 and UNC-44, that may play a role in the transport of mitochondria out of the cell body. Finally, in collaboration with postdoc Natalia Morsci, I examined how microtubule motors and the fission/fusion machinery work together to regulate mitochondrial dynamics in the *C. elegans* neuron.

These findings point the fact that although the basic machinery of mitochondrial dynamics and transport is somewhat understood, in the neuron and potentially other types of cells, there are additional genes that play important roles. Understanding more about these biological processes can shine light on disruptions of mitochondrial dynamics and transport that are linked to human health.

Dedication

First, I would like to thank my advisor, Dr. Christopher Rongo for his support throughout these years. I am immensely thankful that I was part of your lab and one of your graduate students. It hasn't been an easy journey for me, academically, in research, and personally and I owe it to you that I have made it here despite all those bumps in the road. As a scientist, I am honored to have learned from you and I will take with me all of the skills and training I've received under your mentorship. I would also like to thank all the past and current members of the Rongo lab. To each and every one, thank you for all of the time you took to teach me and to give me advice, you have been incredible colleagues: Dr. Piya Ghose, Dr. Itzamarie Chevere-Torres, Dr. Eunchan Park, Dr. Kishore Joshi, Dr. Stephanie Pyonteck, Dr. Natalia Morsci, Dr. Mehul Vora, Tarmie Matlack and Nanci Kane.

I would also like to thank my dissertation committee for their advice and encouragement during these years: Dr. Monica Driscoll, Dr. Bonnie Firestein, and Dr. Qian Cai. To the Rutgers *C. elegans* researchers for being an amazing community of scientists, especially to Dr. Richard Padgett and Dr. Andrew Singson and their lab members who have always been available for questions, for sharing equipment, and also for all of the amazing feedback during presentations and lab meetings. To the talented undergraduate students, I have had the pleasure of teaching in lab: Carol Nowlen, Calina Noah, and Julia Schoeni.

To all of the staff at the Waksman Institute of Microbiology at the general office and the main office, for their help with everything from getting insurance to getting reimbursed after conferences. A special thanks to Ms. Sue Coletta who has been a great friend and who has helped me during my return to the lab after my maternity leave.

To my heart and soul, my family. To my father Ivan, and mother Maria who have always encouraged me to reach higher than I thought I could. A special thanks to my mother who to this day calls me to give me her blessing and wish me luck. To my siblings Jaime and Angela, for paving the way for me and for being my best friends. To my siblings-in-law Eugenia, Maria, Lydia, Victor and Leon and to my nieces Zoe and Ava and nephews Victor, Aaron, Antonio, Leon, and Daniel for filling our family with so much love and joy. To my extended family, aunts, uncles and cousins. To my mother-in-law, Ana, who is like a new mom to me and who loves me like a daughter. To my husband Luis, who has been my number one supporter from the time I was an undergrad student and throughout graduate school; for always believing in me even when I didn't. To my little miracle, Paulina, my heart is so full now that you are in our lives, words cannot express how much I love you and I hope one day you are proud of what mami did while you were on your way to us.

Table of Contents

# Chapter I- Introduction

## I. History of Mitochondria

### Early Work on Mitochondria

Mitochondria are present in eukaryotic cells and are essential organelles that perform cellular respiration as well as biosynthetic and regulatory functions. Mitochondria were initially speculated to be bacteria within cells but were subsequently identified as granules and sausage-shaped organelles in the early 1900s. Their name was derived from the Greek “mitos” (thread) and “chondros” (grain) (*1*). Initial work on mitochondria also speculated that they might provide some hereditary characteristics, but this fact of mitochondria was overlooked as scientists continued to focus on understanding their role in the oxidative process (*1*).

The endosymbiosis theory proposes that mitochondria are bacteria that infiltrated an earlier nucleus-containing cell, giving rise to the early eukaryotic cells (*2*). Their hypothesized role as infiltrating bacteria is quite fitting in fact, as endosymbiotic theory proposes that mitochondria and the related plant organelle, the chloroplast, originated as alphaproteobacteria (*3*). Given this origin, it is not surprising that mitochondria and chloroplasts are unique because they have a separate genome from the nuclear DNA. This does not necessarily imply that mitochondria (or the chloroplast) are formed and participate in different functions of the cell purely using proteins encoded in their own genomes. In fact, most mitochondrial resident proteins are nuclear encoded.

Mitochondrial DNA (mtDNA) is compact (less than 20 Kb) and only encodes for a subset of required mitochondrial proteins. For example, *C. elegans* mtDNA is less than 14 Kb and encodes 36 genes (*4*). Since only a small portion of proteins are encoded in mtDNA, mitochondria also rely on the import of proteins encoded in the nuclear genome.

## II. *C. elegans* as a Model Organism

In our work we are using the model organism *Caenorhabditis elegans*. This model has many advantages including the ability to be used in gene discovery through genetic screens (*5*). *C. elegans* has two sexes, hermaphrodite and male, which makes it easier to manipulate for crosses but also advantageous to have a sex that can self-fertilize. This nematode is a simple model but has many conserved genes found in mammals. Through the use of genetic and molecular biology techniques we can also benefit by creating transgenic lines to use in the analysis of specific genes and their protein products.

The genome of *C. elegans* is 100 Mb and is fully sequenced, which is important for gene discovery. Today, with the advances of whole-genome sequencing, it is faster to connect a mutant to a causative gene.

Additionally, *C. elegans* has a neuronal system that has been well studied, with all of the neurons and synaptic connections fully mapped in the body. Using this model, we can ask neurobiological questions using genetic mutants as well as transgenic strains to see their effects in an intact system.

## III. Structure and Function of Mitochondria

By the mid 1900s, Albert Lehninger observed that oxidation of fatty acids was occurring in liver homogenates, a process he later attributed to the mitochondria using isolation techniques that were being developed at the same time (*6*). These investigations promoted work that would then demonstrate that mitochondria were performing reactions for the citric acid cycle and that these reactions coincided with the generation of ATP. By the 1960s it was observed that enzymes for both fatty acid oxidation and the citric acid cycle were present inside the mitochondria. With the improvement of mitochondrial isolation methods and other purifying techniques, the

protein complexes that carry out redox reactions associated with respiration were isolated and studied.

## Respiratory Metabolism

Our understanding about the processes that occur in the mitochondria has improved over the years. It is widely recognized that the prominent role of mitochondria is to produce ATP (*7-9*). Cellular energy production is a complex process that includes cytosolic reactions (glycolysis) and both the citric acid cycle in the mitochondrial matrix and oxidative phosphorylation that occurs in the inner membrane and inner membrane space.

The citric acid cycle (also known as the Krebs cycle) utilizes the acetyl-CoA that is produced by glycolysis and transported inside the mitochondria. The main function of this pathway is to oxidize the acetyl-CoA to carbon dioxide while producing reduced nicotinamide-adenine dinucleotide (NADH) and reduced flavin-adenine dinucleotide (FADH2). The subsequent step, the electron cycle transport (ETC), is a process that uses the energy from NADH and FADH2 to generate a proton gradient in the intermembrane space, which will then help in the synthesis of ATP from the ATP synthase complex as protons move through it (*10*).

## Other Functions

Calcium transport for the purpose of storage and buffering is also an important function performed by mitochondria (*11*). Different mechanisms for import and export have been found. Calcium is a very important intracellular second messenger and thus needs to be highly controlled in the cell. In mammals, calcium concentration is typically around 100nM and it has been shown that mitochondrial concentration can reach 500-800 μM (*12, 13*). Additionally, iron/sulfur cluster assembly and biosynthesis of cellular

metabolites are also some of the functions performed by mitochondria in specific cell types (*7*).

## Structure and Morphology

Depending on the cell type, mitochondria have different morphological shapes (branched, tubular, circular, etc.) but their basic structure has remains same: double membrane bound organelles with distinct compartments. A continuous inner membrane creates an intermembrane space with the outer membrane (Fig. 1-1). Bounded inside this inner membrane space is the mitochondrial matrix. The different compartments created by these membranes allow for specific processes to occur including the generation of cellular energy. For example, the matrix contains enzymes that conduct oxidative metabolism of incoming pyruvate and fatty acids. Here, the NAD+ and FAD+ will be reduced to NADH and FADH2 that will be later used for electron transfer in the membrane.

For the purpose of increasing the functional surface area, the inner membrane is highly folded and forms cristae that also serve as the scaffold for the machinery that carries out cellular respiration (*14-16*). There are four respiratory enzyme complexes that are arranged in the inner membrane and form the electron transport chain: NADH dehydrogenase, succinate dehydrogenase, cytochrome bc1, and cytochrome oxidase (*17*). With the exception of succinate dehydrogenase, these complexes translocate protons across the membrane, which serves as the driving force for the generation of ATP. The mitochondrial ATP synthase is an enzyme that is also located in the inner membrane and is responsible for using the proton gradient created by the ETC to synthesize ATP (*10*).

## IV. Mitochondria: Dynamics, Transport and Mitophagy

Advances in microscopy, vital dyes, and fluorescent protein reporters have shown the dynamic characteristics of mitochondria in the cell. Depending on the cell type, mitochondria can either form networks or remain as a more tubular structures. This dynamic ability includes stages of organelle fission and fusion (*18*).

### Fusion and Fission

Mitochondrial fission (division) plays an important role in the distribution of mitochondria in the cell. This is particular necessary for when the cell divides to give to daughter cells (*19*). Compensation for fission occurs by the event of fusion (the merging of two or more mitochondria). Cells use this dynamic equilibrium to meet their specific energy requirements, and they can modulate dynamics when energy demands change (*20*).

Mitochondria can also alter their dynamics during periods of stress. For example, in mouse embryonic fibroblasts, exposure to a number of stressors, including UV irradiation, actinomycin D and cycloheximide treatment, results in stress-induced mitochondrial hyperfusion (SIMH) (*21*). In our lab we have also observed that lack of oxygen (anoxia) is an additional stressor that can trigger mitochondrial hyperfusion (*22*). While the physiological purpose of SIMH remains a mystery, it is clear that mitochondrial dynamics play an important role in maintaining functional mitochondria, and it is thought that fission events might be a way in which mitophagy could accomplish quality control. More recently, mitophagy and mitochondrial dynamics have been of interest for their associations with certain types of neurodegenerative diseases such as the case of Parkinson's disease (*23*).

Mitochondrial fission and fusion events are highly regulated processes that are occurring in various organisms, including *Drosophila*, mammals, and *C. elegans*.

Additionally, fusion and fission dynamics might play significant roles in events such as cell cycle and proliferation. Some of the genes and proteins that are regulating these processes have been identified, but how these processes are regulated is not fully understood (Fig. 1-2). The first fusion protein described was FZO-1, which was found in a genetic screen in *Drosophila melanogaster* for sterile males (*24*). Other proteins have been found to also play a role in fusion in mammals and other model organisms. Mitofusin (Mfn) is the mammalian homolog for FZO-1 (*25*). Further, the protein OPA1 (mammals) and EAT-3 (*C. elegans*) have been shown to mediate the outer and inner membrane fusion events (*26-28*). Similar to other types of fusion of membranes like in the case of vesicle trafficking, FZO-1 proteins will form complexes in trans between the membrane of one mitochondrion and the membrane of another mitochondrion (*29*). In mitochondrial fusion assays, the lack of mitofusins in one of the two merging mitochondria is sufficient to prevent fusion (*30*).

Separate proteins carry out mitochondrial fission. In yeast, FIS-1 for example, is located in the outer membrane and DRP-1, recruited to site of constriction, assist in the fission of the mitochondrial membrane (*31-33*). In the mammalian field, other proteins have been hypothesized to be working to achieve this, Mff, MiD49 and Mid51 (*34*). A key issue that remains unanswered is how DRP-1 is recruited to the mitochondria and some theories point to prior activation of resident proteins like FIS-1 (*33*).

## Transport

The behavior of mitochondria in the cell is a result of interactions with proteins on the outer membrane and components of the cytoskeleton (*35*). Motor proteins in particular have been found to co-localize with mitochondria and microtubules to aid in their movement within the cell (*36*). Intermediate filaments may also play a role in positioning but may function at different times than microtubules (*35*).

In polarized cells like the neurons, for example, biogenesis of mitochondria is thought to occur in the cell body and mitochondria are then transported toward distal processes such as the synapse (anterograde) and also back to the cell body (retrograde). Since mitochondria produce the cellular energy for the neuron it is necessary for these organelles to be present at the site of need. For example, in the synapses mitochondria have been found to cluster to help with production of ATP that will be used in neurotransmission as well as for the buffering of Ca2+ (*37*). In the axons, mitochondria can also be found to cluster in areas of high energy consumption such as areas that have ion pumps (*38*).

Mitochondria are mobilized throughout the cell with the help of motor proteins that have been found to be highly conserved among organisms. In the case of neurons, some of these proteins used for the anterograde and retrograde movement of mitochondria include: Kinesin-1(KIF5), MIRO, Milton, Syntaphilin, KLP6, Myosin, Dynein and others (*39-45*). (Fig. 1-3)

Kinesin-1(KIF5), plays a role in the anterograde mitochondrial transport along the axon. Kinesin consists of monomers that have kinesin heavy chain subunits that contain an N-terminal motor domain and tail domain; these then form homodimers (KHC). In addition, two kinesin light chains subunits associate with the tail of the motor subunits (KLC) and also help to connect the motor to cargo. (*46, 47*) In the case of *C. elegans,* the kinesin-1(KIF5)'s orthologue is the protein UNC-116. Similar to their role in mammals, UNC-116 in the worm has also been found to be required for transporting membrane-bound organelles including mitochondria. (*48-51*)

MIRO and Milton are motor adaptor proteins that associate with mitochondria and the kinesin KIF5 and were first found in the *Drosophila* model. Milton was first identified in photoreceptor mutants and was found to be a protein associated with mitochondria and the motor proteins, since Milton mutants lacked mitochondria in the

axons and synapses (*40*). MIRO was identified in an EMS screen. Mutants lacking MIRO had a short lifespan and defects in locomotion as well as accumulation of mitochondria at neuromuscular junctions. Expression of MIRO in the neurons of these mutants was able to restore the wild-type phenotype, ruling out the involvement in muscle in the locomotion defect. This data suggests that MIRO and Milton work in the anterograde transport of mitochondria in neurons and are the adaptors interacting with the kinesin motor (*41*).

However, recent work in the worm has found that the *C. elegans* MIRO gene doesn't have a defect of mitochondrial density and thus may not be playing a direct role as adaptor in the worm (*52*). From the three MIRO orthologues reported in the worm, none of them were shown to alter mitochondrial density in the ALM process (*52*). Instead, this report found that there is a different regulation occurring. Their results suggest that UNC-16/JIP3 and UNC-76/FEZ1 help regulate mitochondrial density in the ALM. They do so by regulating kinesin levels, multiple alleles for the *unc-16* and *unc-76* genes show a significant increase of mitochondrial density and elevated levels of Kinesin-1. In addition, UNC-16/JIP3 and UNC-76/FEZ1 might be regulating mitochondrial transport in the retrograde direction. Mutants of *unc-16* and *unc-76,* have reduced retrograde transport which might be caused by reduced availability of dynein complex subunits. These mutants show greatest accumulation of mitochondria at the distal end of the ALM neuron. (*52*)

Myosin V and VI play a role in movement of mitochondria along actin. In *Drosophila* RNAi experiments, depletion of myosin V caused an increase of mitochondrial transport and an increase in mitochondrial length in the axons. By contrast, depletion of myosin VI increased the transport of mitochondria but in the retrograde direction. This report described the role of both of these myosins in the mitochondrial transport along the axons but in opposite directions (*44*). There are a few

other proteins involved in other aspects of transport, one of those Syntaphilin, is used for docking of mitochondria along the axons. Also the Dynein motor, which is essential for retrograde movement, has also been previously described. Although some of the proteins playing a role in mitochondrial transport have been described in recent literature, there is still a need to understand more about this process and the mechanisms that are regulating and conducting this transport.

### Mitophagy

The process of removing cellular components is called autophagy. For this process an autophagosome encapsulates the targeted component and engulfs it for removal. This process has been found to also occur for damaged mitochondria that cannot be repaired by the process of fusion to other mitochondria (*53*). Proteins that are key in carrying out the process in mammals were first found while investigating patients that had Parkinson's Disease. In other organisms such as yeast, screens have helped find additional proteins necessary for mitophagy. (*53, 54*) Recent work has found that Parkin and PINK1 genes mediate mitophagy in cell culture, but it is not clear what their roles are in vivo. (*54-56*) In yeast, the protein Atg32 is the one that is necessary for the removal of mitochondria through mitophagy. (*57*) The model for the Parkin and PINK1 removal focuses on the fact that PINK1 is a resident mitochondrial protein, once this protein accumulates (because of failure to import and degrade), then Parkin protein is recruited to the mitochondria. Parkin then plays a role in the recruitment of the autophagosome as well as helping degrade mitochondrial proteins.

## V. Mitochondrial Diseases

Mutations that affect the mitochondrial proteins involved in maintaining structure, dynamics, or metabolism can influence changes in cell growth and cell death. Studies

using the *Saccharomyces cerevisiae* model organism were some of the first to elucidate that mutations in mtDNA or nuclear DNA coding for proteins directed for the mitochondria could critically affect the health of the cell (*58*). The petite mutants, for example, were first discovered in yeast due to their small colony phenotype. It was later found that this phenotype was caused by either mutations in the mtDNA (rho+), deletions of mtDNA (rho-), or no mtDNA (rho0) (*58*). These mutants have defects in respiration or oxidative phosphorylation, and they form small colonies. Additional mutants have been more recently found, and they include nuclear genes that are required for the mitochondria.

Dysfunctional mitochondria in humans can cause disease, and this has been of research interest in recent decades. For example, Holt and his colleagues found patients with mitochondrial myopathies to have deletions in their mtDNA (*59*). Since this publication, many others have described mitochondrial mutations, including point mutations in genes, as causes for disease including: myoclonus epilepsy and ragged red fibers (MERFF), Kearns-Sayre syndrome (KSS), mitochondrial encephalomyopathy (MELAS), neuropathy, ataxia, retinis pigmentosa (NARP) and others (*60*). One disease to note is the Dominant Optic Atrophy, which is caused by mutations in the nuclear gene OPA1. Mutations in this gene impair mitochondrial fusion, which leads to dysfunctional mitochondria (*61*). This defect primarily affects the retinal ganglion cells, which transmit the visual information to the brain. When these cells die there is no visual information transmitted. Clinically this is inherited in a dominant manner and is the most common form of neuropathy, and patients suffer from loss of visual acuity from an early age. Overall, in many of these diseases multiple organs are affected because the mutations in either mitochondrial DNA or mitochondrial targeted proteins.

## VI. Key Questions Addressed in this Thesis

Because mitochondria are essential organelles and especially important for neuronal health it is important to try and understand how mitochondria are regulated as well as how these function in response to stress. In this thesis we wanted to understand how mitochondrial dynamics change in response to oxygen deprivation. Second, we wanted to know what additional proteins are regulating mitochondrial dynamics and transport. Finally, we also want to ask how motor proteins interact with the machinery of the fusion and fission in the neuron. For all of this work we are employing the model organism *C. elegans.*

## VII. Figures

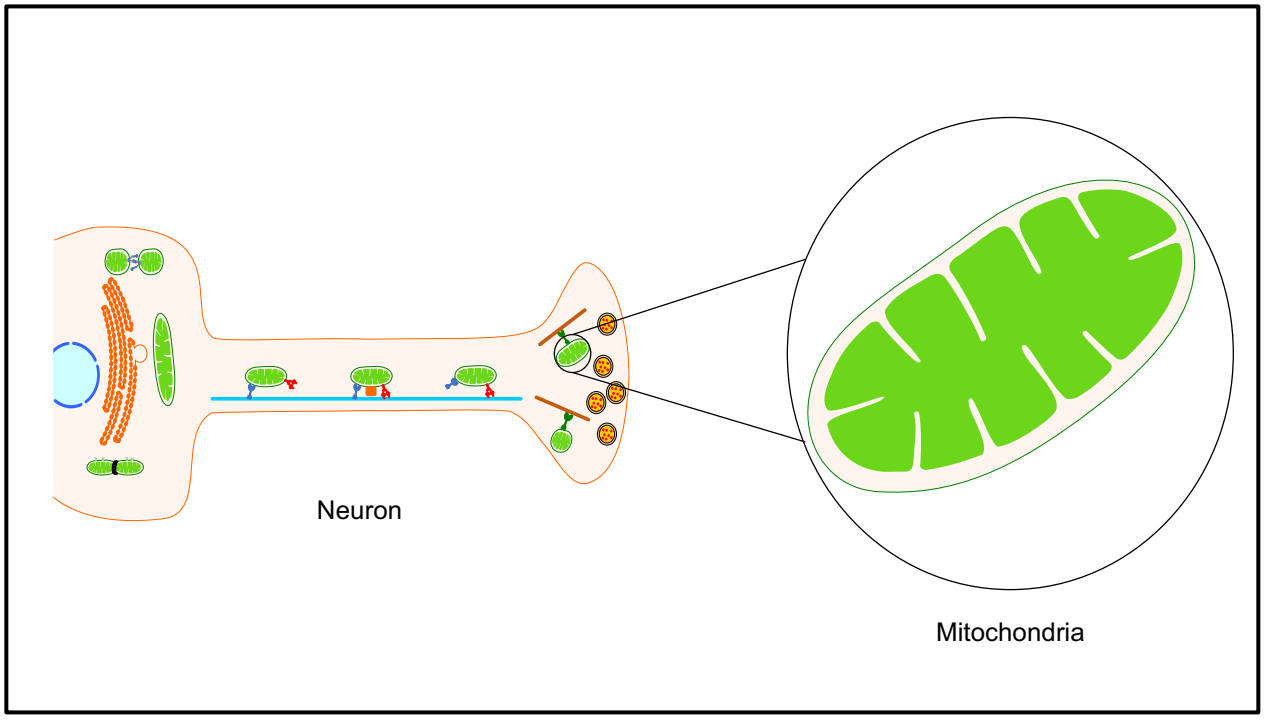


Figure 1.1

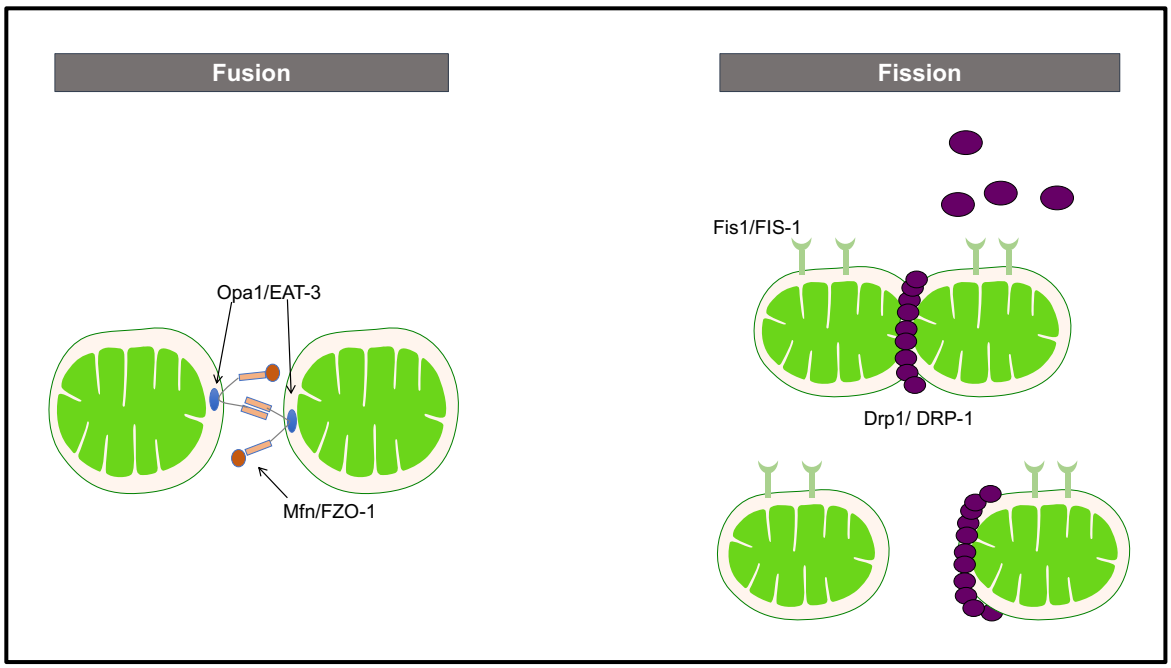


Figure 1.2

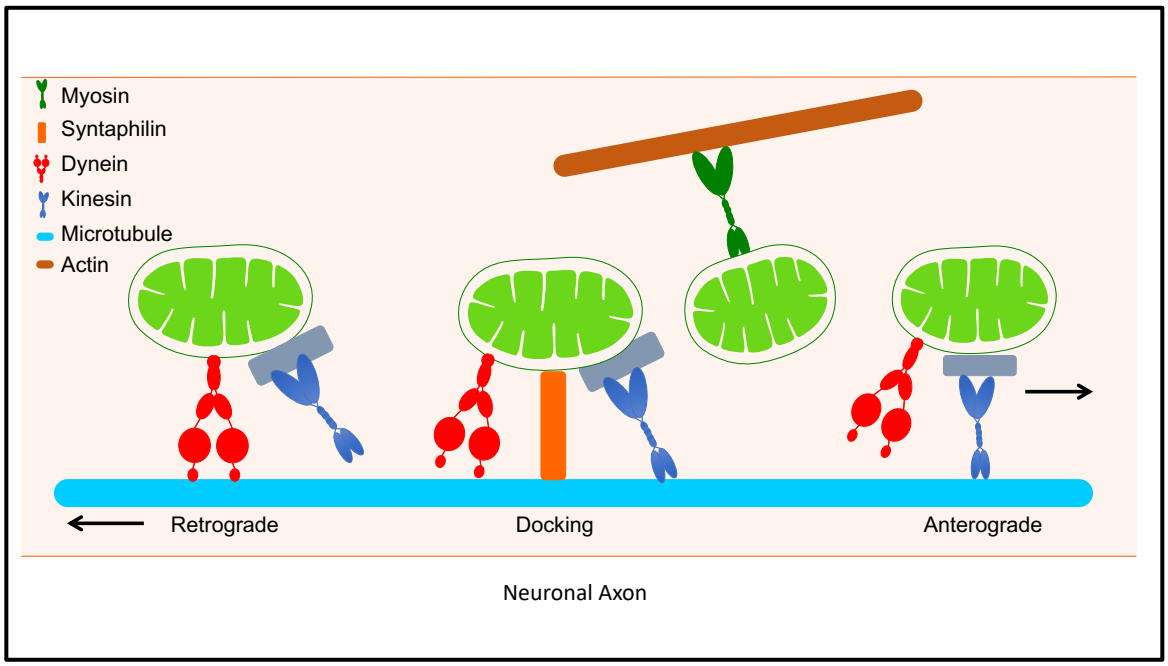


Figure 1.3

## VIII. Figure Legends

Figure 1.1

Schematic of Mitochondria as a double membrane organelle.

Figure 1.2

Mitochondrial fusion and fission events. Mitochondria fusion carried out by mitochondrial proteins Opa1/EAT-3 and Mfn/FZO-1. Mitochondrial fission carried out by the recruitment of the protein Drp1/DRP-1 with the help of membrane proteins such as Fis1/FIS-1.

Figure 1.3

Scheme of mitochondrial transport along the axon. Retrograde transport using Dynein and anterograde transport being carried out by Kinesin and adaptor proteins along microtubules. Docking of mitochondria occurring by the use of Syntaphilin. Short length transport using Myosin along actin filaments.

# Chapter II- Anoxia-Reoxygenation Regulates Mitochondrial Dynamics Through the Hypoxia Response Pathway SKN-1/Nrf, and Stomatin Protein STL-1/SLP2

Piya Ghose[1,2*], Eun Chan Park[1*], Alexandra Tabakin[1], Nathaly Salazar-Vasquez[1,3], and Christopher Rongo[1]

*[1] The Waksman Institute, Department of Genetics, Rutgers The State University of New Jersey, Piscataway, New Jersey, United States of America.*

*[2] The Graduate Program in Neuroscience, Rutgers The State University of New Jersey, Piscataway, New Jersey, United States of America.*

*[3] The Graduate Program in Genetics and Microbiology, Rutgers The State University of New Jersey, Piscataway, New Jersey, United States of America.*

**These authors made equal contributions*

To Whom Correspondence Should Be Addressed:

Christopher Rongo

Waksman Institute/Rutgers University

190 Frelinghuysen Rd.

Piscataway, NJ 08854

Phone (908) 445-0955

Fax (732) 445-5735

Email: rongo@waksman.rutgers.edu

Running Title: Anoxia and Mitochondrial Dynamics

Author Contributions

The chapter presented here is added as published in the PLOS Genetics Journal December 2013, Volume 9, Issue 12 (*22*). Minor formatting changes for figure numbers, legends and references have been made for consistency in this document.

I conducted the anoxia survival and recovery from suspended animation experiments that contributed to Figure 1 and Figure 3R in the publication. The first authors, Dr. Piya Ghose and Dr. Eunchan Park designed the experiments along with Dr. Christopher Rongo and all wrote the manuscript. Dr. Alexandra Tabakin was an undergraduate student in the lab and conducted a lot of the imaging and quantification.

## I. Abstract

Many aerobic organisms encounter oxygen-deprived environments and thus must have adaptive mechanisms to survive such stress. It is important to understand how mitochondria respond to oxygen deprivation given the critical role they play in using oxygen to generate cellular energy. Here we examine mitochondrial stress response in *C. elegans*, which adapt to extreme oxygen deprivation (anoxia, less than 0.1% oxygen) by entering into a reversible suspended animation state of locomotory arrest. We show that neuronal mitochondria undergo DRP-1-dependent fission in response to anoxia and undergo refusion upon reoxygenation. The hypoxia response pathway, including EGL-9 and HIF-1, is not required for anoxia-induced fission, but does regulate mitochondrial reconstitution during reoxygenation. Mutants for *egl-9* exhibit a rapid refusion of mitochondria and a rapid behavioral recovery from suspended animation during reoxygenation; both phenotypes require HIF-1. Mitochondria are significantly larger in *egl-9* mutants after reoxygenation, a phenotype similar to stress-induced mitochondria hyperfusion (SIMH). Anoxia results in mitochondrial oxidative stress, and the oxidative

response factor SKN-1/Nrf is required for both rapid mitochondrial refusion and rapid behavioral recovery during reoxygenation. In response to anoxia, SKN-1 promotes the expression of the mitochondrial resident protein Stomatin-like 1 (STL-1), which helps facilitate mitochondrial dynamics following anoxia. Our results suggest the existence of a conserved anoxic stress response involving changes in mitochondrial fission and fusion.

## II. Author Summary

Oxygen deprivation plays a role in multiple human diseases ranging from heart attack, ischemic stroke, and traumatic injury. Aerobic organisms use oxygen to generate cellular energy in mitochondria; thus, oxygen deprivation results in energy depletion. Low oxygen can be catastrophic in tissues like the nervous system, which has high-energy demands and few glycolytic reserves. By contrast, other cells, including stem cells and cancerous cells within tumors, adapt and thrive in low oxygen. We are just beginning to understand how different organisms and even different cell types within the same organism respond to low oxygen conditions. The response of mitochondria to oxygen deprivation is particularly critical given their role in aerobic energy production. In addition, mitochondria actively injure cells during oxygen deprivation through the generation of reactive oxygen species, the disruption of calcium homeostasis, and the activation of cell death pathways. Here we use a genetic approach to show that mitochondria undergo fission during oxygen deprivation and refusion upon oxygen restoration. The hypoxia response pathway and the oxidative stress response pathway together modulate this response. We identify a new factor, stomatin-like protein, as a promoter of mitochondrial fusion in response to oxygen deprivation stress. Our findings uncover a new mechanism – regulated mitochondrial dynamics – by which cells adapt to oxygen deprivation stress.

## III. Introduction

Oxygen is critical for the survival of obligate aerobic organisms, and such organisms have evolved stress responses to avoid or offset damage when confronted with low oxygen (hypoxia) or no oxygen (anoxia) in their natural environment. Indeed, many species have evolved mechanisms that allow them to adapt to oxygen deprivation and its consequences for prolonged periods (*62-65*). Yet even within the same species, adaptation to oxygen deprivation varies dramatically according to tissue type, age, and sex (*66-70*). Within humans, oxygen deprivation can be a normal physiological condition; for example, a low oxygen microenvironment is required for stem cells to maintain their undifferentiated state (*71*). Oxygen deprivation is also a critical facet of multiple human pathologies. Cancerous cells have been observed to adapt to the hypoxic microenvironment of solid tumors, and this adaptive response can promote malignancy (*72*). Oxygen deprivation also has devastating consequences during ischemic stroke and heart attack (*73-75*). A better understanding of the responses to oxygen deprivation stress should therefore lend itself to the development of new therapies for treating diseases ranging from ischemic damage to cancer.

Oxygen deprivation has major consequences for mitochondria in particular given their role as the hub for aerobic metabolism and ATP generation. Mitochondria play an active role in cellular injury during oxygen deprivation (e.g., during ischemia and reperfusion) through the generation of reactive oxygen species (ROS), the disruption of calcium homeostasis, and the activation of cell death signaling pathways (*76-78*). Given the potential threat from mitochondria during oxygen deprivation, cells execute stress responses that include changes in mitochondrial biogenesis and removal (*79*). Mitochondria exist in a dynamic state of fission and fusion, and this balance can be tipped by stress or disease towards fission and subsequent autophagy/mitophagy of the fragmented mitochondrial products (*80*). Mitochondria sometimes respond to stress by

showing increased levels of fusion, including a form of augmented fusion mediated by the prohibitin-like SLP-2 protein, termed stress-induced mitochondrial hyperfusion (SIMH) (*21*). While the exact purpose for these changes in morphological dynamics is unclear, regulated mitochondrial dynamics appear to be particularly important in neurons, which have high energy demands but little in the way of glycolytic reserves. Correspondingly, altered mitochondrial dynamics are observed in multiple forms of neurodegeneration, which is particularly sensitive to mitochondrial function (*81, 82*).

*C. elegans* is used as a model for oxygen deprivation stress response. Soil nematodes naturally encounter environmental conditions with variable oxygen concentrations (*83, 84*). Under conditions of hypoxia (~1% oxygen), *C. elegans* decreases its oxygen consumption and alters its locomotion and aerotaxis behaviors, but continues to develop and reproduce (*85-90*). Under conditions of anoxia (<0.1% oxygen), *C. elegans* undergoes developmental arrest and enters a state of suspended animation, eventually dying after long term exposure (*84, 91-94*).

*C. elegans* also exhibits different signaling responses to anoxia and hypoxia. For example, in response to hypoxia *C. elegans* employs the conserved hypoxia response pathway. When oxygen levels are sufficiently high, the prolyl hydroxylase EGL-9 uses molecular oxygen, 2-oxoglutarate, and iron to hydroxylate key proline side chains on HIF-1, the hypoxia-inducible factor, resulting in HIF-1 protein degradation (*85, 95-98*). Under hypoxic conditions, HIF-1 remains stable, acting as a transcription factor to regulate gene expression (*99, 100*). The signaling response pathway to anoxia is less well understood, but mutations in the insulin/IGF signaling pathway, the AMP Kinase (AMPK) pathway, and the p38 MAP Kinase (MAPK) pathway can sensitize *C. elegans* to anoxia-induced death (*92, 101-103*). These signaling molecules are implicated in responding to oxidative stress and ROS, suggesting that ROS and alterations in

mitochondria might contribute to anoxia-induced damage, although the exact cellular and molecular mechanisms remain unclear.

Here we use cell biological and genetic approaches to address how *C. elegans* mitochondria respond to anoxia. We show that anoxia induces mitochondrial fission in *C. elegans* neurons, whereas reoxygenation results in mitochondrial refusion. We show that the hypoxia response pathway and the oxidative stress response factor SKN-1/Nrf promote mitochondrial refusion during reoxygenation. Specifically, we find that mitochondria undergo hyperfusion when EGL-9 activity is absent, an effect that is similar to that of SIMH in stressed mammalian cells. We show that SKN-1/Nrf promotes the expression of STL-1, the *C. elegans* ortholog of SLP-2, a key mediator of mammalian SIMH, and that both SKN-1/Nrf and STL-1 are essential for the hyperfusion observed during reoxygenation following anoxia. Our results suggest that anoxia regulates mitochondrial dynamics through the hypoxia response pathway and the oxidative stress pathway by promoting hyperfusion during recovery, and that the mitochondrial resident protein STL-1 is required for this specific stress response.

## IV. Results

### Anoxia promotes suspended animation and eventually death in *C. elegans*

To examine the effects of anoxia on adult *C. elegans*, we raised wild-type embryos and larvae under normoxic conditions and then shifted developmentally synchronized animals (24 hours following the L4 larval molt) to anaerobic biobags (anoxia) at 20$^{o}$C for various lengths of time (Figure 2-1A). We then returned the animals back to normoxic conditions (reoxygenation) and allowed them to recover for 24 hours. Greater than 95% of wild-type animals survived 24 hours of short-term anoxia; however, about half survived 48 hours of long-term anoxic exposure, and fewer than 10% survived 72 hours of anoxia (Figure 2-1B), rates similar to those previously reported for solid agar

culturing (*92, 93, 104*). Upon anoxic exposure, animals entered into a previously described state of suspended animation in which they did not move (*84*). Suspended animation was rapidly reversible upon reoxygenation, with nematodes emerging from suspension at a rate that reflected the duration of the initial anoxic exposure (Figure 2-1C).

Anoxia promotes DRP-1-dependent mitochondrial fission

We sought to understand the cell biological mechanism behind anoxia-induced suspended animation in *C. elegans*. Given the sensitivity of neurons to oxygen levels, we focused our attention on neurons. We also considered the critical role mitochondria play in both neuronal function and oxygen consumption, and we proceeded to test specifically whether mitochondria in *C. elegans* neurons respond to changes in ambient oxygen. To visualize neuronal mitochondria, we generated transgenic animals expressing a mitochondrial matrix-directed leader sequence attached to GFP (MitoGFP) in the command interneurons using the *glr-1* promoter. We obtained two independently integrated transgenic lines, called *odIs70* and *odIs71*, which showed no apparent differences other than chromosomal position. Fluorescently labeled mitochondria from these lines appeared as elongated structures and smaller circular puncta along the ventral cord neurites of these neurons, and they showed a more reticulate orientation in the neuronal cell bodies (Figure 2-2A and data not shown).

Various cellular stresses can induce changes in mitochondrial dynamics (*21, 80, 81, 105*). We tested whether the stress of anoxia exposure could regulate mitochondrial dynamics in *C. elegans* neurons expressing MitoGFP. We found that 24 hours of anoxia resulted in the loss of elongated mitochondria (Figure 2-2B) such that the average length of ventral cord mitochondria decreased by 40% and total number decreased by 30% (Figure 2J,K). Within minutes of reoxygenation, we observed a reversal towards longer

mitochondria, and within a few hours mean mitochondrial length and number were restored to pre-anoxic levels (Figure 2-2C,J,K).

We reasoned that the changes that we observed in mitochondrial length in response to anoxia could be due to changes in mitochondrial dynamics, including fission and fusion. To test this possibility, we examined neuronal mitochondria in mutants that were either defective for fission (e.g., *drp-1* mutants) or fusion (e.g., *eat-3* mutants). Mutants for *drp-1* contained a smaller number of individual mitochondria, and these mitochondria were far more elongated than ever observed in wild type (Figure 2-2D,J,K), consistent with impaired fission. By contrast, under normoxia mitochondria from mutants for the mitofusin *eat-3* were smaller than wild type and similar in size to those found in anoxia-exposed animals (Figure 2-2G,J), although more numerous (Figure 2-2K), consistent with a block in fusion. If the reduction in mitochondrial size during anoxia is a result of changes in fission/fusion dynamics, then mutations in *drp-1* should block the effects of anoxia on mitochondrial length, and mutations in *eat-3* should preclude any additional reduction in size caused by anoxia. We examined *drp-1* mutants following anoxia and during reoxygenation, and we observed that mitochondria underwent bead-like swelling (Figure 2-2E,F) but did not complete fission into smaller organelles (Figure 2-2J), suggesting that anoxia triggers the formation of constriction sites that fail to become severed due to the absence of DRP-1. Moreover, mitochondria in *eat-3* mutants showed no change in size following anoxia and reoxygenation compared to wild type (Figure 2-2G,H,I). Taken together, our results suggest that anoxia can induce changes in mitochondrial size that are dependent on the mitochondrial dynamics machinery.

The hypoxia response pathway regulates mitochondrial hyperfusion upon anoxia recovery

One possible mechanism by which neurons might sense anoxia and respond by regulating their mitochondrial dynamics is through the hypoxia response pathway, including its key components: EGL-9 and HIF-1 (*85*). We examined MitoGFP in the molecular null loss of function mutants *egl-9(sa307)* and *hif-1(ia4)* (*106, 107*). Neuronal mitochondria from both mutants were indistinguishable from those of wild type under both normoxic and anoxic conditions (Figure 2-3A-H,P,Q), indicating that this pathway is not the mechanism by which neurons sense anoxia and facilitate anoxia-induced fission. Surprisingly, mitochondrial size in *egl-9* mutants was restored in 10 minutes upon reoxygenation post-anoxia compared to an hour in wild type, suggesting a more rapid fusion rate (data not shown). Moreover, the total extent of mitochondrial fusion in *egl-9* mutants upon post-anoxia reoxygenation was excessive, resulting in elongated structures (Figure 2-3F,P,Q), which we refer to as “hyperfused” mitochondria. Introduction of a wild-type *egl-9* transgene with its expression restricted to the command interneurons by the *glr-1* promoter completely rescued the changes in mitochondrial dynamics following reoxygenation observed in *egl-9* mutants (Figure 2-3M-O, P,Q), suggesting that EGL-9 has a cell-autonomous function for regulating mitochondrial dynamics in response to oxygen deprivation stress.

EGL-9 regulates multiple developmental and behavioral processes through its negative regulation of HIF-1 function (*86, 87, 108, 109*). If EGL-9 were regulating mitochondria through HIF-1, then elongated mitochondria should not be observed in *egl-9* mutants that also lack *hif-1* activity. We found that mean mitochondrial size in *egl-9 hif-1* double mutants resembled that of wild-type animals (Figure 2-3J-L,P,Q), indicating that HIF-1 is required for EGL-9 to regulate mitochondria in response to anoxia-reoxygenation. Interestingly, the mitochondrial number of *egl-9 hif-1* double mutants was not restored upon reoxygenation, suggesting that EGL-9 might regulate mitochondrial number independent of HIF-1 (Figure 2-3Q).

We also found that *egl-9* mutants rapidly emerged from suspended animation upon reoxygenation compared to wild type (Figure 2-3R), similar to the rapid rate of mitochondrial refusion observed in these mutants. By contrast, *hif-1* mutants showed a slight but significant decrease in their rate of emergence, and *hif-1* mutations blocked the rapid emergence observed in *egl-9* mutants. We obtained a transgene that expresses a wild-type EGL-9 cDNA under the control of a pan-neuronal promoter (*89*), introduced it into *egl-9* mutants, and found that it completely restored the emergence behavior to the slower rate observed in wild-type animals (Figure 2-3R). Our data indicate that EGL-9 activity in the nervous system is sufficient to regulate suspended animation behavior following anoxia treatment.

Because *egl-9* mutants show an increase in mitochondrial fusion upon reoxygenation, we reasoned that increased mitochondrial fusion by itself might explain the rapid emergence of *egl-9* mutants from suspended animation. We tested this possibility by examining the rate at which mutants with altered fusion/fission dynamics reemerged from suspended animation. Whereas half of wild-type animals were awake and moving within 10 minutes of reoxygenation following 24 hours of anoxia, less than 10% of *drp-1* mutants and no *eat-3* mutants had emerged from suspended animation at the same time point (data not shown), suggesting that the dynamic nature of mitochondrial morphology per se might be required for animals to adapt and respond to anoxic stress. Alternatively, the complete block of fission or fusion in these mutants might compromise organismal health so as to preclude drawing informative conclusions from stress-induced behavioral assays.

## Mitochondrial hyperfusion requires the canonical mitochondrial fusion machinery

The elongated, hyperfused mitochondria observed in reoxygenated *egl-9* mutants could be due to altered activity of the canonical mitochondrial fission or fusion

machinery. Alternatively, hyperfusion could be a novel form of mitochondrial fusion. To test these possibilities, we examined double mutants between *egl-9* and either *drp-1* or *eat-3*. Mitochondria from *egl-9 eat-3* double mutants were similar in size to those from *eat-3* single mutants, (Figure 2-4A-L,M,N), suggesting that EAT-3 is required for the mitochondrial hyperfusion observed in *egl-9* mutants upon reoxygenation. In addition, we did not observe any additional increase in mitochondrial size in *egl-9 drp-1* double mutants compared to the single mutants (Figure 2-4G-I,M,N), suggesting that anoxia-reoxygenation cannot cause additional mitochondrial fusion in the absence of DRP-1. These findings suggest that the hyperfusion observed in *egl-9* mutants during reoxygenation is not likely to be due to a novel fission/fusion mechanism but instead relies on the canonical mitochondrial dynamics machinery.

One simple mechanism by which anoxia might regulate mitochondrial dynamics would be through the enhanced recruitment, turnover, or stabilization of the mitochondrial dynamics machinery during reoxygenation (*110-112*). To test this possibility, we generated a transgene to express an N-terminally tagged DRP-1 protein under the control of the *glr-1* promoter. We introduced this transgene into nematodes and observed that GFP::DRP-1 was localized to punctate structures in neuron cell bodies (data not shown) and along the ventral cord neurites (Figure 2-S1A). We also visualized the *C. elegans* mitofusin EAT-3 by introducing a similar EAT-3::GFP chimeric transgene into nematodes; EAT-3::GFP was localized to puncta, similar to GFP::DRP-1 (Figure 2-S1D). We exposed animals carrying these transgenes to anoxia and reoxygenation; however, we did not observe any significant changes in GFP::DRP-1 or EAT-3::GFP subcellular localization (Figure 2-S1B,C,E,F). We also examined the localization of these proteins in *egl-9* mutants under the same conditions, but did not observe significant changes (data not shown). These results suggest that anoxia and

EGL-9 might regulate mitochondrial dynamics by a mechanism other than DRP-1 or mitofusin recruitment.

## Anoxia induces mitochondrial oxidative stress in neurons

A similar mitochondrial hyperfusion has also been observed in cultured mammalian cells exposed to various stresses, a process termed Stress-Induced Mitochondrial Hyperfusion (SIMH) (*21*). In addition, anoxia survival rates in *C. elegans* are influenced by mutations in the insulin/IGF signaling and p38 MAPK pathways, which respond to oxidative stress and ROS (*92, 101-103*). We therefore reasoned that neuronal mitochondria might generate ROS upon anoxic exposure. To test this directly, we generated *odIs111*, a stably integrated transgenic line that expresses MitoROGFP (ROGFP attached to a mitochondrial matrix-directed leader sequence). The fluorescent protein ROGFP (Reduction-Oxidation-sensitive Green Fluorescent Protein) is a modified version of GFP that contains multiple introduced cysteine substitutions, resulting in a protein that upon oxidation demonstrates a rapid, reversible shift in its peak excitation absorbance from 490 nm to 400 nm (*113, 114*). We captured confocal images of animals that express MitoROGFP using 405 nm and 476 nm excitation maxima. Under normoxic conditions, MitoROGFP was localized to puncta along ventral cord neurites, similar to MitoGFP, and had a stronger emission when excited by 476 nm compared to 405 nm (Figure 2-5A,C). To test whether MitoROGFP can report mitochondrial oxidative stress, we exposed nematodes to hydrogen peroxide ($H_2O_2$), a commonly used agent for causing oxidative stress in *C. elegans* (*115*). We found that $H_2O_2$ increased the ability of 405 nm light and decreased the ability of 476 nm light to evoke MitoROGFP fluorescence, resulting in 65% increase in the 405/476 excitation ratio (Figure 2-5G). We also exposed animals expressing MitoROGFP to anoxic conditions and found a shift in emission maxima similar to that of $H_2O_2$ treatment (Figure 2-5B,D, E-G), suggesting

that neuronal mitochondria produce ROS and undergo oxidative stress upon anoxic treatment.

SKN-1 is required for mitochondrial hyperfusion following anoxia-reoxygenation

Given that anoxic mitochondria produce ROS, we considered that the oxidative stress response pathway might be required for the corresponding changes in mitochondrial dynamics during anoxia. The transcription factor SKN-1/Nrf is required for the oxidative stress response in *C. elegans* and mammals, and SKN-1/Nrf can associate with mitochondria, where it could directly sense mitochondrial ROS production (*115, 116*). Once activated, SKN-1 enters the nucleus and promotes the transcription of phase II detoxifying enzymes and antioxidants to mitigate the harmful effects of oxidative stress (*117, 118*). To test whether SKN-1 is required for anoxia-induced mitochondrial hyperfusion, we introduced the MitoGFP transgene into *skn-1* mutants and observed a slight reduction in mitochondrial size in these mutants (Figure 2-6A,D,J,K). Nevertheless, exposure to anoxia could still trigger an additional reduction in the average mitochondrial size in these mutants, and mitochondrial size was restored after reoxygenation, similar to wild type (Figure 2-6A-F,J,K). Interestingly, anoxia did not trigger a decrease in mitochondrial number in *skn-1* mutants, suggesting that SKN-1 might be required for changes in mitochondrial number during anoxia. We also examined MitoGFP in *egl-9 skn-1* double mutants and found that the elongated mitochondria observed in *egl-9* mutants were completely absent when *skn-1* mutations were introduced (Figure 2-6G-I,J,K), indicating that SKN-1 is required for anoxia-induced mitochondrial hyperfusion. In addition, mutations in *skn-1* reduced the accelerated recovery of *egl-9* mutants from suspended animation following anoxia (Figure 2-6L), suggesting that SKN-1 helps mediate functional recovery from anoxia.

SKN-1 regulates the expression of prohibitin-like STL-1/SLP-2

To identify potential transcriptional targets of SKN-1 that could explain its role in mitochondrial hyperfusion, we screened through potential SKN-1 binding sites identified in ChIP-seq experiments performed by the modENCODE consortium. A SKN-1 binding region occurs ~500 bp upstream of the start site of the gene *stl-1* (*119*). STL-1 is the lone possible ortholog of mammalian Stomatin-Like Protein 2 (SLP-2), a mitochondrial inner membrane protein required for SIMH in cultured cells (*21*), with 59% identity and 77% similarity at the protein level to human SLP-2 (STOML2) (*120*). Like SLP-2, STL-1 contains a conserved N-terminal mitochondrial leader sequence and a single SPFH domain (*121*) along its sequence (Figure S2). Conservation between STL-1 and rodent and human SLP-2, as well as a potential Drosophila ortholog, extends along the entire protein (Figure 2-S3).

To confirm that STL-1 is present in neurons, we generated $P_{stl\text{-}1}$*::GFP,* a transgene that contains 1 kilobase of sequence upstream from the *stl-1* start codon fused to sequences for GFP (Figure 2-S4A). We introduced $P_{stl\text{-}1}$*::GFP* into the nematode germ line to generate transgenic animals and observed GFP expression in all tissues (Figure 2-S4B,C,D). We also generated $P_{stl\text{-}1}$*::STL-1::GFP*, which contains the same sequences as in $P_{stl\text{-}1}$*::GFP*, as well as the complete open reading frame and introns, resulting in a translational fusion to GFP (Figure 2-S4A); we observed a similar expression pattern using this transgene (Figure 2-7G and data not shown).

To confirm that STL-1, like SLP-2, is a mitochondrial resident protein, we examined its subcellular localization using two approaches. First, we generated a transgene containing a STL-1::GFP translational chimera under the control of the *glr-1* neuronal promoter. We also generated a separate transgene that contains the mitochondrial resident marker TOM-20::mCherry under the control of the *glr-1* promoter (*122*). We generated transgenic lines and observed that both TOM-20::mCherry and

STL-1::GFP were localized to elongated structures in a similar fashion to that of MitoGFP in neuron cell bodies and the ventral cord neurites (Figure 2-7A-D). In addition, we found that TOM-20::mCherry and STL-1::GFP were colocalized (Figure 2-7E,F). As a second approach, we stained live nematodes expressing $P_{stl\text{-}1}$*::STL-1::GFP* with MitoTracker. Whereas MitoTracker cannot penetrate far enough into *C. elegans* tissues to stain neuronal mitochondria, it can label mitochondria in the hypodermis (*123*). Hypodermal mitochondria are arranged in elongated networks, and we found that STL-1::GFP was localized to these MitoTracker-decorated networks (Figure 2-7G,H,I). These results indicate that STL-1 is localized to mitochondria in *C. elegans*, similar to SLP-2 in mammalian cells.

To test whether *stl-1* expression is activated by anoxic exposure and oxidative stress through SKN-1, we first exposed nematodes to the herbicide paraquat, which causes mitochondria to generate superoxide anions (*115, 124*). We then isolated total mRNA from these nematodes and measured *stl-1* mRNA levels by qRT-PCR. Paraquat treatment triggered a two-fold increase in *stl-1* mRNA levels in wild type (Figure 2-7J). We also examined *stl-1* levels in nematodes exposed to anoxia and found a similar increase (Figure 2-7J). In contrast, we did not observe an increase in *stl-1* mRNA levels in *skn-1* mutants exposed to either paraquat or anoxia (Figure 2-7J), indicating that SKN-1 is required for *stl-1* regulation by oxidative stress and anoxia.

## STL-1 is required for mitochondrial hyperfusion following anoxia-reoxygenation

Given its similarity to SLP-2, we reasoned that STL-1 is required for mitochondrial hyperfusion following anoxia. We obtained *stl-1(tm1544),* a mutant that contains a deletion removing half of the *stl-1* gene, including most of the SPFH domain, and results in a frameshift and a premature stop eleven codons following the deletion (Figure 2-S2, 2-S4). Mutants for *stl-1* had no obvious defects in viability, fertility,

development, movement, or gross health under standard laboratory conditions (data not shown). We introduced our $P_{glr\text{-}1}$*::MitoGFP* transgene into *stl-1* mutants and found that there were normal numbers and sizes of mitochondria in these mutants compared to wild type (Figure 2-8A-G, M, N). We exposed *stl-1* mutants to anoxia followed by reoxygenation and observed the same changes in mitochondria morphology in these mutants that we observed in wild type (Figure 2-8H,I,M,N). We generated double mutants between *stl-1* and *egl-9* to test whether STL-1 is required for the hyperfusion that occurs in anoxia-treated *egl-9* mutants. We found that mitochondrial shape and size in reoxygenated *egl-9* mutants was restored to wild-type levels when STL-1 activity was removed (Figure 2-8L, M), indicating that STL-1 is required for the anoxia-induced hyperfusion observed in these mutants. Mutations in *stl-1* did not restore mitochondrial number in reoxygenated *egl-9* mutants, suggesting that EGL-9 regulates mitochondrial number independently from STL-1 (Figure 2-8N). Mutations in *hif-1* and *stl-1* when combined did not have an additive effect in suppressing hyperfusion in *egl-9* mutants (Figure 2-8P). Interestingly, mutations in *stl-1* partially reduced the accelerated recovery of *egl-9* mutants from suspended animation following anoxia, suggesting that STL-1-mediated hyperfusion of mitochondria helps mediate functional recovery from anoxia (Figure 2-8Q).

If STL-1 is directly mediating hyperfusion in neuronal mitochondria, then it should be required in the same cells as the mitochondria that we are observing. To test this possibility, we generated a transgene containing an inverted repeat of the *stl-1* gene under the control of the *glr-1* promoter to knock down *stl-1* levels solely in the command interneurons by heritable double-stranded RNA interference (*125*). We introduced this $P_{glr\text{-}1}$*::stl-1(RNAi)* transgene into *egl-9* mutants and found that it had no effect on mitochondrial morphology under normoxia or anoxia conditions. However, the hyperfusion typically observed following anoxia was blocked in *egl-9* with the $P_{glr\text{-}1}$*::stl-*

*1(RNAi)* transgene (Figure 2-8O), suggesting that STL-1 functions cell-autonomously to promote hyperfusion.

One possible explanation for why *stl-1* mutations suppress the effects of *egl-9* mutations is that STL-1 could be part of the hypoxia response pathway, acting to promote HIF-1 function. We think that this is unlikely for several reasons. First, we tested whether HIF-1 levels are regulated by STL-1. EGL-9 negatively regulates HIF-1 by promoting HIF-1 ubiquitin-dependent proteolysis (*85*). We generated a transgene containing a HIF-1::GFP chimera under the control of the *glr-1* promoter. We introduced this $P_{glr\text{-}1}$*::HIF-1::GFP* transgene into the nematode germ line to generate a transgenic line and observed low-level nuclear HIF-1::GFP accumulation in the neurons of transgenic animals exposed to normal oxygen (Figure 2-9A). We next crossed this same transgenic line into either *egl-9* mutants or *stl-1* mutants. In *egl-9* mutants, we observed a significant increase in nuclear HIF-1::GFP levels (Figure 2-9B,E). By contrast, we observed little change in nuclear HIF-1::GFP in *stl-1* mutants (Figure 2-9C,E). In addition, mutations in *stl-1* did not block the increase in nuclear HIF-1::GFP observed in *egl-9* mutants (Figure 2-9D,E). Thus, EGL-9 negatively regulates HIF-1 in *C. elegans* neurons, but HIF-1 turnover does not appear to be regulated by STL-1.

We also examined whether STL-1 promotes HIF-1 function by measuring the levels of *nhr-57*, a known transcriptional target of HIF-1 under conditions of hypoxia (*126, 127*). We found that anoxia treatment resulted in a four-fold increase in *nhr-57* transcript levels relative to those found in animals under normoxia (Figure 2-9F). The levels of *nhr-57* were unchanged in normoxic and anoxic *hif-1* mutants relative to normoxic wild type (Figure 2-9F), indicating that HIF-1 transcriptional activity is increased in response to anoxia, similar to observations of nematodes under hypoxia (*127*). As expected, *nhr-57* levels were dramatically elevated in *egl-9* mutants but not in *egl-9 hif-1* double mutants (Figure 2-9F). By contrast, mutants for *stl-1* contained similar

levels of *nhr-57* mRNA compared to wild type. Moreover, *nhr-57* mRNA levels in *egl-9 stl-1* double mutants were unchanged relative to *egl-9* single mutants, suggesting that STL-1 is not required for HIF-1 to regulate its canonical transcriptional targets. Finally, anoxia induced an increase in *stl-1* mRNA levels in *egl-9* and *hif-1* mutants, similar to the wild-type response (data not shown). Taken together, our results suggest that STL-1 functions independently of EGL-9 and the canonical hypoxia response pathway to promote mitochondrial hyperfusion.

## V. Discussion

Here we have shown that oxygen levels regulate mitochondrial dynamics in *C. elegans* neurons, and that the canonical hypoxia response pathway, the oxidative stress response factor SKN-1/Nrf, and the prohibitin-like protein STL-1 can modulate this response (Figure 2-10). When oxygen levels are sufficiently high, mitochondria exist as a mixture of small and elongated dipolar structures continually undergoing fission and fusion in equilibrium. Under conditions of anoxia, this equilibrium shifts such that smaller mitochondria predominate. In addition, nematodes respond to anoxia by ceasing their movement, entering into suspended animation until conditions improve. Prolonged anoxia results in lethality. However, if the conditions of anoxia are reversed and reoxygenation occurs before the onset of long-term damage, then the animals can emerge from suspended animation and resume their normal development and behavior. Reoxygenation also results in the restoration of the mitochondrial equilibrium to the size distribution that existed prior to the original anoxic stress. Whereas the hypoxia response pathway is not required for the anoxia-induced shift towards smaller mitochondria, it does appear to regulate mitochondrial reconstitution during reoxygenation. In the absence of EGL-9 activity, reoxygenated mitochondria become elongated beyond what is observed prior to anoxia, indicative of hyperfusion. This

anoxia-induced hyperfusion is reminiscent of the SIMH that is observed in stressed mammalian cells in culture. Indeed, the mitochondrial hyperfusion that we observed here requires the prohibitin-like STL-1, the *C. elegans* ortholog of SLP-2, a key mediator of SIMH in mammalian cells. Moreover, the expression of STL-1 also requires the transcription factor SKN-1, which is activated by oxidative stress in mitochondria during anoxia. Interestingly, these signaling pathways are also important for modulating the rate at which anoxic animals emerge from suspended animation. We favor a model in which extreme oxygen deprivation activates the hypoxia response pathway and, through the resulting mitochondrial oxidative stress, the transcription factor SKN-1. SKN-1 in turn promotes the expression of the mitochondrial resident STL-1 to augment the rate and extent of mitochondrial refusion upon the restoration of normal oxygen levels. This resulting augmentation results in a more rapid restoration of nervous system function.

*C. elegans*, like many metazoans, encounters zones of low oxygen in its natural environment (*83*). Generally, nematodes use specialized sensory neurons and a rapid aerotaxis response pathway to migrate towards areas with an oxygen concentration range of 5-15% (*88, 128, 129*). This response is short term (on the order of seconds to minutes), allowing the animal to avoid areas of low oxygen without making dramatic changes in cellular metabolism.

Sometimes the aerotaxis pathways are not sufficient or activated in time to prevent nematodes from entering a hypoxic environment (~1% oxygen). The conserved hypoxia response pathway becomes activated both to offset the cellular stress of hypoxia in all tissues and to modulate an additional locomotory circuit behavioral response that allows the animals to escape the hypoxic region (*85, 90*). The EGL-9 prolyl hydroxylase is the oxygen sensor under these conditions, inhibiting HIF-1. EGL-9 also promotes the activity of glutamate receptors within the command interneurons through a HIF-1-independent mechanism, thereby favoring local foraging behavior.

Under hypoxic conditions, EGL-9 becomes inactivated and HIF-1 becomes derepressed, resulting in the upregulation of hypoxia response genes that promote cellular survival under low oxygen conditions; this response includes a rather dramatic shift in strategy for cellular energy production away from oxygen-dependent, mitochondrial-based oxidative phosphorylation and towards anaerobic energy production mechanisms like glycolysis. Hypoxia also results in glutamate receptor activity becoming repressed in the command interneurons, resulting in a switch from local foraging behavior to escape behavior. This is a medium-term response (on the order of minutes to hours) and a sound “escape” strategy, as it allows nematodes to continue to generate sufficient ATP under limited oxygen conditions to propel locomotory behavior so that the animal can flee to areas of higher oxygen concentration.

A more potentially debilitating scenario occurs when nematodes encounter environments of nearly complete oxygen deprivation (anoxia). Under these conditions, maximizing energy production can become a risk rather than an asset, particularly for mitochondria, which generate ROS and release calcium to the cytosol during anoxia. The cellular stress response strategy shifts from maximizing energy production to minimizing energy production and ameliorating oxidative stress. Interestingly, we observed a decrease in both mitochondrial size and number after anoxic exposure, which could be consistent with cells removing potentially dangerous mitochondria during anoxic stress, perhaps by mitophagy, although this remains to be shown. At the organismal level, the stress response strategy also shifts, from one of escape, which requires significant energy production to support locomotion, to one of suspended animation, which minimizes both energy requirements and damage from the associated oxidative stress. This response is long term (on the order of hours to days) and meant to maximize survival during long periods of anoxia until environmental conditions change

for the better. Once oxygen is restored, mitochondria become fused again and the original mitochondria number and morphology become restored.

Several signaling pathways modulate survival during anoxia. Mutants lacking the insulin/IGF-like receptor DAF-2 survive for longer periods under anoxia, either because they have elevated expression of genes that offset cellular damage and proteotoxicity, or because they have a reduced metabolic rate (*92, 102, 130*). Mutants lacking one of the p38 MAPK pathways also survive anoxia better than do wild-type animals (*101*). Preconditioning animals through changes in diet or high temperature growth can also increase survival to subsequent anoxia, perhaps by building up carbohydrate stores in advance of the anoxic period through the activation of AMPK (*103*).

Our results demonstrate that the EGL-9/HIF-1 hypoxia response pathway is also critical for modulating the response to anoxic stress – a novel role for this pathway. Mutants lacking EGL-9 recover from anoxia-induced suspended animation more rapidly than do wild-type animals; this phenotype can be rescued by restoring EGL-9 solely to the nervous system, suggesting that the suspended animation that is triggered by anoxia might be a regulated function of the nervous system rather than a systemic shutdown of all tissues. Mutants lacking *egl-9* also survive anoxia better than wild-type animals do (data not shown), suggesting that HIF-1, while not required for animals to survive anoxia (*104*), can promote anoxia survival when its levels are elevated. In this way, *egl-9* mutants provide a model for studying the cellular changes that occur when HIF-1 signaling is elevated due to normal cellular physiology (e.g., in stem cells) or as part of a cellular pathology (e.g., in solid tumors). We speculate that HIF-1 regulates the expression of yet unknown genes involved in mitochondrial dynamics, resulting in fission/fusion machinery that is primed to mediate rapid and extensive changes in mitochondrial morphology and function.

Anoxia results in oxidative stress at mitochondria. Interestingly, a subpopulation of SKN-1 protein is localized at mitochondria, presumably to sense the local oxidation environment (*116*). We believe that mitochondrial ROS produced during anoxia activates SKN-1, which in turn promotes mitochondrial hyperfusion and rapid recovery from suspended animation. SKN-1 likely regulates the expression of multiple genes that regulate mitochondrial dynamics and promote recovery from suspended animation following anoxia. One such direct target is STL-1, the *C. elegans* ortholog of the mammalian SLP-2 required for SIMH. STL-1/SLP-2 might mediate hyperfusion by regulating and/or recruiting the fusion/fission machinery (*21, 131*). While we did not observe changes in the levels or subcellular localization of machinery components like DRP-1 and EAT-3, it remains possible that anoxia and STL-1 regulate this machinery post-translationally. Alternatively, STL-1/SLP-2 might promote hyperfusion and mitochondrial function by regulating cardiolipin enrichment in mitochondria (*132*).

For reasons that remain unclear, SIMH hyperfusion results in mitochondria that produce higher ATP levels during stress (*21, 133*). Mitochondrial hyperfusion similar to SIMH also occurs in *C. elegans* mutants impaired for electron transport chain activity, further suggesting a relationship between mitochondrial dynamics and the production of cellular energy (*134*). Increased energy production from hyperfused mitochondria cannot be explained by fusion alone, as the downregulation of fission proteins leads to less ATP production, most likely due to unbalanced fission/fusion dynamics damaging mitochondria (*20, 135, 136*). Perhaps hyperfusion facilitates the restoration of cellular energy by maximizing mitochondrial membrane and cristae, or dilutes damaged mitochondrial contents through intermixing with functional mitochondria. SIMH, the description of which has been restricted to mammalian tissue culture cells, likely has a similar role, and our findings would indicate that SIMH occurs *in vivo*.

## VI. Materials and Methods

### Strains

Animals were grown at 20°C on standard NGM plates seeded with OP50 *E. coli*. Some strains were provided by the *Caenorhabditis* Genetics Center. Strains were backcrossed to our laboratory N2 strain. The following strains were used: *drp-1(cq5), eat-3(ad426), egl-9(sa307), hif-1(ia4), skn-1(tm3411), stl-1(tm1544), odIs70[$P_{glr-1}$::MitoGFP, unc-119(+)], odIs71[$P_{glr-1}$::MitoGFP, unc-119(+)], odEx[$P_{glr-1}$::EGL-9A, ttx-3::rfp], nEx[$P_{ric-19}$::GFP::EGL-9(+), $P_{unc-25}$::mCherry], odIs111[$P_{glr-1}$::MitoROGFP, ttx-3;;rfp], odEx[$P_{stl-1}$::GFP, ttx-3::rfp], odEx[$P_{stl-1}$::STL-1::GFP, ttx-3::rfp], odIs124[$P_{glr-1}$::STL-1::GFP, ttx-3::rfp], odIs125[$P_{glr-1}$::STL-1::GFP, ttx-3::rfp], odIs121[$P_{glr-1}$::TOM-20(N-terminus)::mCherry, ttx-3::rfp], odIs122[$P_{glr-1}$::TOM-20(N-terminus)::mCherry, ttx-3::rfp], odEx[$P_{glr-1}$::HIF-1::GFP], odEx[$P_{glr-1}$::stl-1(RNAi), ttx-3::rfp], odEx[$P_{glr-1}$::GFP::DRP-1, ttx-3::rfp],* and *odEx[$P_{glr-1}$::EAT-3::GFP, ttx-3::rfp].*

### Transgenes and Germline Transformation

The *$P_{glr-1}$::MitoGFP* transgenic plasmid (pOR775) was generated by ligating a PstI/KpnI fragment containing the aspartate aminotransferase mitochondrial leader sequence and GFP sequences from pPD96.32 (A. Fire) into pV6, a vector containing the *glr-1* promoter (a gift from Villu Maricq, University of Utah). The *$P_{stl-1}$::STL-1::GFP* transgenic plasmid (pOR763) was generated by using PCR to amplify the *stl-1* genomic locus plus 1 kb of promoter from fosmid WRM0612bG12, and then by using Gateway® to introduce the product into a vector containing a C-terminal GFP. The *$P_{stl-1}$::GFP* transgenic plasmid was generated using a similar approach, but without the *stl-1* coding sequences. Several transgenes were generated by using PCR to amplify cDNA from an OpenBiosystems clone followed by Gateway® recombination to introduce the product into a vector containing the *glr-1* promoter and C-terminal GFP; these include *$P_{glr-1}$::STL-*

*1::GFP* (pOR776), $P_{glr\text{-}1}$*::TOM-20::mCherry* (pOR769 – contains the first 162 nucleotides of the cDNA), and $P_{glr\text{-}1}$*::EAT-3::GFP* (pOR750). The $P_{glr\text{-}1}$*::GFP::DRP-1* transgenic plasmid (pOR655) was generated by using PCR to amplify cDNA from an OpenBiosystems clone followed by Gateway® recombination to introduce the product into a vector containing the *glr-1* promoter and an N-terminal GFP. The $P_{glr\text{-}1}$*::MitoROGFP* transgenic plasmid (pOR809) was generated by chemically synthesizing a ROGFP (Genscript) optimized for *C. elegans* expression based on GFP from pPD96.32. Mitochondrial leader sequence was then added as described above for pOR775. The neuronal-specific EGL-9 rescuing transgene, *nEx[*$P_{ric\text{-}19}$*::GFP::EGL-9(+),* $P_{unc\text{-}25}$*::mCherry]*, was a kind gift from Dengke Ma and Bob Horvitz (MIT).

To knock down the *stl-1* gene, we generated a transgene that synthesized a sense and an antisense mRNA under the control of the *glr-1* promoter (*137*). The *stl-1* cDNA was amplified by PCR (forward primer 5'-AAAATGGCGCTAACTAATCGACTTTTAATG-3' and reverse primer 5'-TCACTTTTTCTTATTGCTCAATGAGTCGTAAAC-3') and subcloned into pCR8 (Invitrogen) by the TOPO cloning reaction, resulting in sense and antisense donor vectors. The donor cDNAs were then moved into pOR298, a destination vector containing the *glr-1* promoter and *unc-54* 3'UTR, resulting in an *stl-1* sense transgene and an *stl-1* antisense transgene. Plasmids for the sense and antisense transgenes were equally mixed (50 ng/µl each) and introduced into *C. elegans* as described below.

Transgenic strains generated in this study were isolated after microinjecting various plasmids (5–50 ng/µl) described above using the indicated transgenic marker (typically *ttx-3::rfp*, a gift from Oliver Hobert, Columbia University, unless otherwise indicated). All resulting transgenes were introduced into the germ line and followed as extrachromosomal arrays. All nematodes were cultured according to standard approaches.

## Anoxia-Reoxygenation

NGM plates seeded with a small lawn of OP50 were used. Approximately 50 N2 (wild-type) animals of L4 stage were picked onto the small amount of food on the plate. Transparent AnaeroPack®-Anaero sachets were used to create an anoxic environment, as described above. Methylene blue test strips inside each sachet were used to confirm anaerobic conditions. To normalize each experimental replicate, all genotypes were placed into the same sachet for the times indicated, and control genotypes were carefully evaluated for suspended animation behavior to verify that anoxic conditions were generated. To initiate reoxygenation, plates were recovered from the sachet and returned to standard laboratory conditions for the times indicated.

## Oxidative Stress Induction

To induce oxidative stress, L4 stage synchronized animals were treated with 200 mM $H_2O_2$ (Fisher-Scientific) in M9 buffer for 1 hr or 150 mM methyl viologen dichloride hydrate (Paraquat, Sigma) in M9 buffer for 1 hr.

## Behavioral Video-Quantified Emergence Assay

AnaeroPack®-Anaero sachets were used to create an anoxic environment, as described above. Upon reoxygenation, plates were immediately video recorded to observe the animals as they emerged from suspended animation. Videos of 700 pixels x 700 pixels were captured at 30 FPS using a Nikon Camera (Mod. No. 352500) and Streampix acquisition software (Version 3.46.0).

## Behavioral Simultaneous Emergence Assay

Strains were synchronized accordingly, and at L4 stage approximately 50 animals were picked to NGM plates seeded with OP50. A wild-type control was included along with the mutant strains, which were outcrossed six times to the control. Following 24 hours of anoxia treatment, the plates were removed and simultaneously quantified for the number of animals in suspended animation versus moving (emerged) at time zero and after 10 minutes.

## Fluorescence Microscopy

GFP-, RFP-, and mCherry-tagged fluorescent proteins were visualized in nematodes by mounting larvae on 2% agarose pads with levamisole. AnaeroPack®-Anaero sachets were used to create an anoxic environment, as described above. Fluorescent images were observed using a Zeiss Axioplan II. A 100X (N.A. = 1.4) PlanApo objective was used to detect GFP and RFP signals. Imaging was done with an ORCA charge-coupled device (CCD) camera (Hamamatsu, Bridgewater, NJ) using iVision v4.0.11 (Biovision Technologies, Exton, PA) software. Exposure times were chosen to fill the 12-bit dynamic range without saturation.

The quantification of ventral nerve cord fluorescent mitochondria was done using ImageJ (*138*) to automatically threshold the images and then determine the outlines of fluorescent objects in ventral cord neurites. ImageJ was used to quantify both the shape and the size of all individual fluorescent mitochondria along the ventral cord. Mitochondrial size was measured as the maximum diameter for each outlined fluorescent object. Object number was calculated by counting the average number of puncta per 100 microns of neurite length.

$P_{glr\text{-}1}$::HIF::GFP images for the PVC neuron cell bodies were taken using a confocal microscope equipped with the confocal imager (CARV II; BD) and a 40X Plan

Neofluar objective, NA 1.3 (Carl Zeiss). Exposure times were chosen to fill the 12-bit dynamic range without saturation. The quantification of HIF-1::GFP fluorescence intensity in the nucleus was conducted using iVision v4.0.11 (BioVision Technologies) software. After background signals were subtracted, total nuclear HIF-1::GFP pixel intensity was divided by the area to get the mean nuclear intensity value.

Real Time qRT-PCR Measurements

Total RNAs were extracted with Trizol (Invitrogen Co., Carlsbad, CA). L4 stage worms (10-20 animals each) were resuspended in 250µl of Trizol and lysed by one round of freezing (by liquid nitrogen) and thawing (60 °C) with subsequent vigorous vortexing in 4 °C for 30 min. PCR was performed in an Eco real-time qPCR system (Illumina, San Diego,CA) using iScriptTM One-Step RT-PCR Kit With SYBR® Green (Bio-Rad Laboratories Inc., Hercules, CA) in 20 µL reactions with 20 ng of RNA template. We used as forward (5'-AGAAGCGTGGGTTGTAGAAAG-3') and reverse (5'-TGTAATGGCTCCTTGCTCAG-3') primers, respectively, for *stl-1*. We used as forward (5'-CGTGATTGCAGACTTGAAAGC-3') and reverse (5'-GCGTTTGACTTCCATCGTTTG-3') primers, respectively, for *nhr-57*. We used as forward (5'-ACCATGTACCCAGGAATTGC-3') and reverse (5'-TGGAAGGTGGAGAGGGAAG-3') primers, respectively, for *act-1*. Samples were measured two to three times and average values were used for the calculation of relative fold changes. The relative levels of *stl-1* and *nhr-57* mRNA were normalized to the levels of *act-1* mRNA in each preparation. For each experiment, the value for wild type normoxia was set to 1 and other values were normalized accordingly.

### Confocal Imaging of MitoROGFP

To measure the MitoROGFP redox transition after anoxia and $H_2O_2$ exposure, images were collected on a Leica SP5 II confocal microscope (Leica Microsystems, Exton, PA) using a 63X (N.A.=1.4) oil immersion lens. Samples were alternately excited between a 30% 405 nm UV laser and a 30% 476 nm visible laser with a sequential line scanning method. The emission detection was configured for HYD1 photon counting at 508-513 nm. Images were processed using Leica LAS-AF software (version 2.0.0), Image J, and Adobe Photoshop CS3 (Adobe systems). To compare the intensities of each mitochondrion between two excitation wavelengths (405 nm and 476nm), the same mitochondrial ROIs were chosen to obtain intensity values for both excitation wavelengths. The 405/476 ratios in each experiment were normalized to the values of wild type normoxia.

### MitoTracker Staining

Mitotracker (Invitrogen M7512) stock (1mM in DMSO) was diluted in M9 to a 1:1000 working solution. Animals carrying the $P_{stl\text{-}1}$*::STL-1::GFP* translational reporter were incubated in this solution for one hour at room temperature and subsequently washed, transferred to standard NGM plates, and allowed to recover for 30 minutes in the dark prior to imaging as describe above.

## VII. Acknowledgements

We thank Andy Fire, the *C. elegans* Genetics Center, Villu Maricq, Dengke Ma, Oliver Hobert, Bob Horvitz, Alex van der Bliek, and Shohei Mitani for reagents and strains. We thank Roshni Shah and Erica Kent for technical assistance with *stl-1*. We thank Monica Driscoll and Stephanie Pyonteck for comments on the manuscript.

VIII. Figures

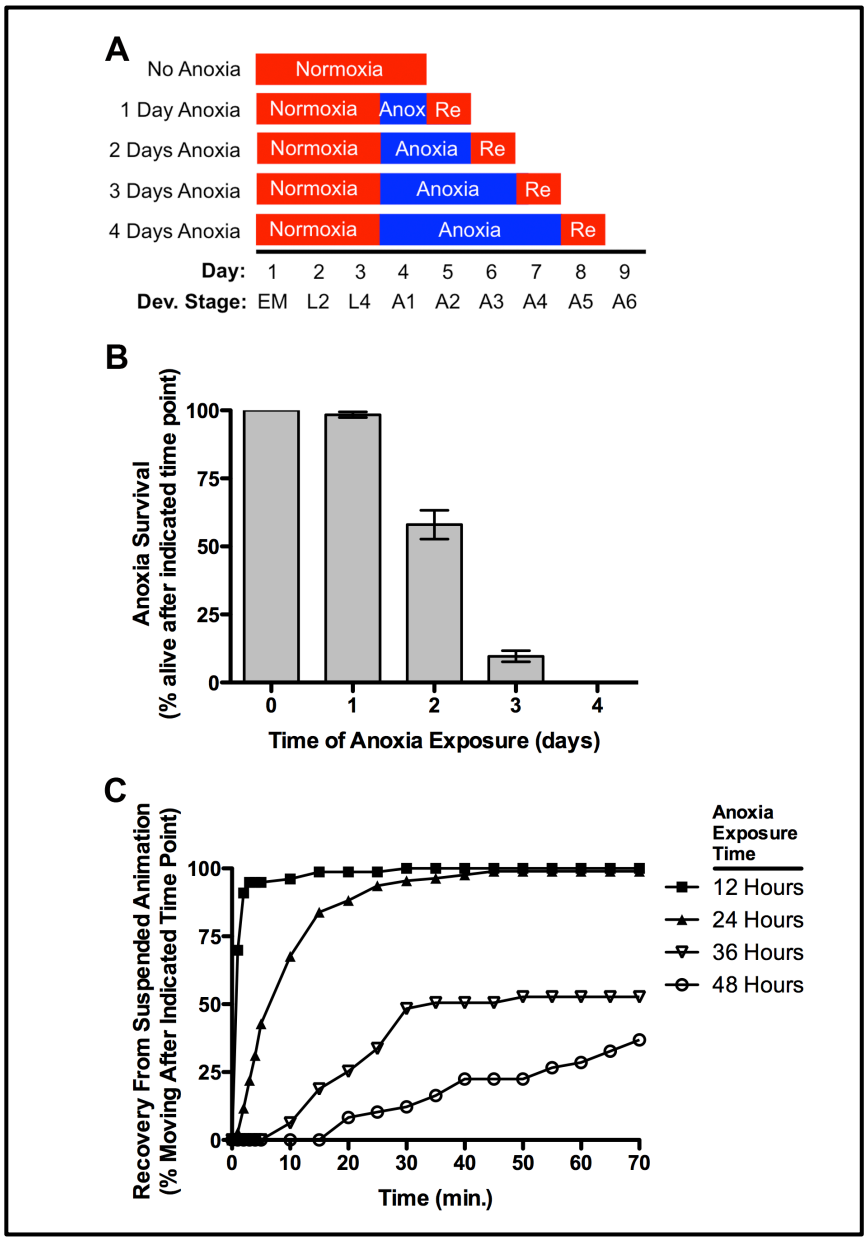


Figure 2-1

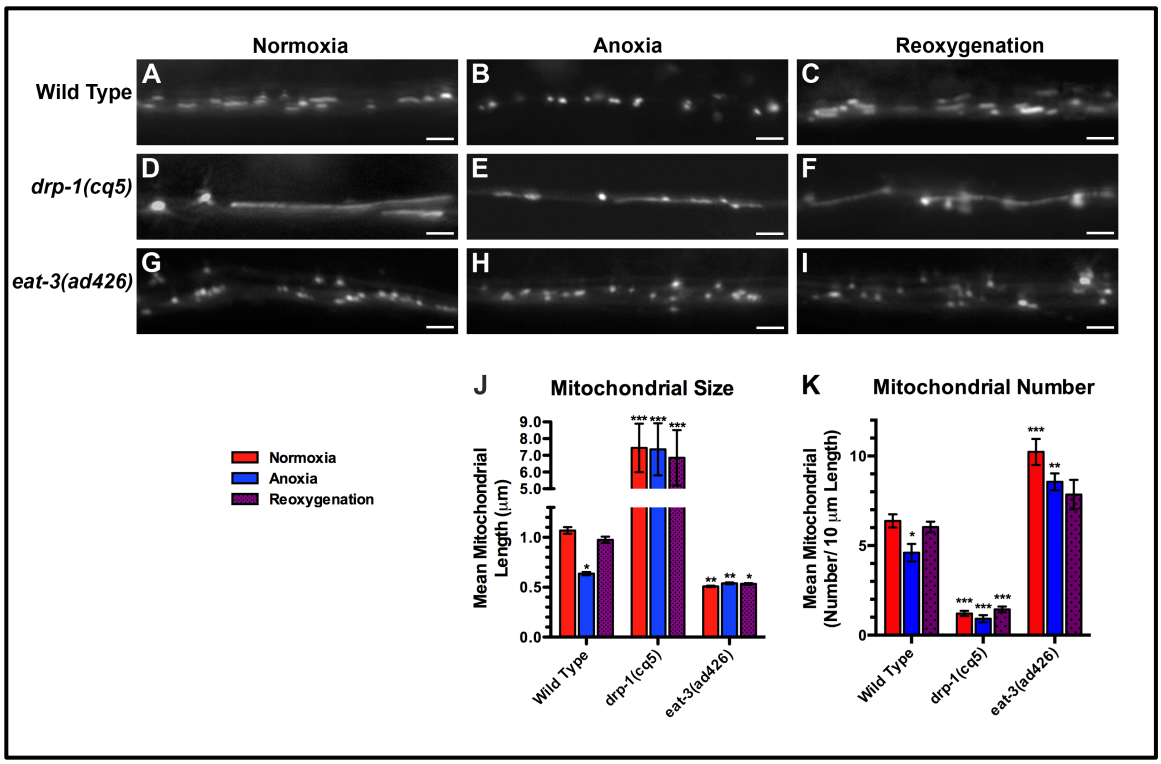
Normoxia
Anoxia
Reoxygenation
Wild Type
drp-1(cq5)
eat-3(ad426)
A
B
C
D
E
F
G
H
I
Normoxia
Anoxia
Reoxygenation
J
Mitochondrial Size
Mean Mitochondrial Length (μm)
9.0
8.0
7.0
6.0
5.0
1.0
0.5
0.0
Wild Type
drp-1(cq5)
eat-3(ad426)
K
Mitochondrial Number
Mean Mitochondrial (Number/ 10 μm Length)
10
5
0
Wild Type
drp-1(cq5)
eat-3(ad426)

Figure 2-2

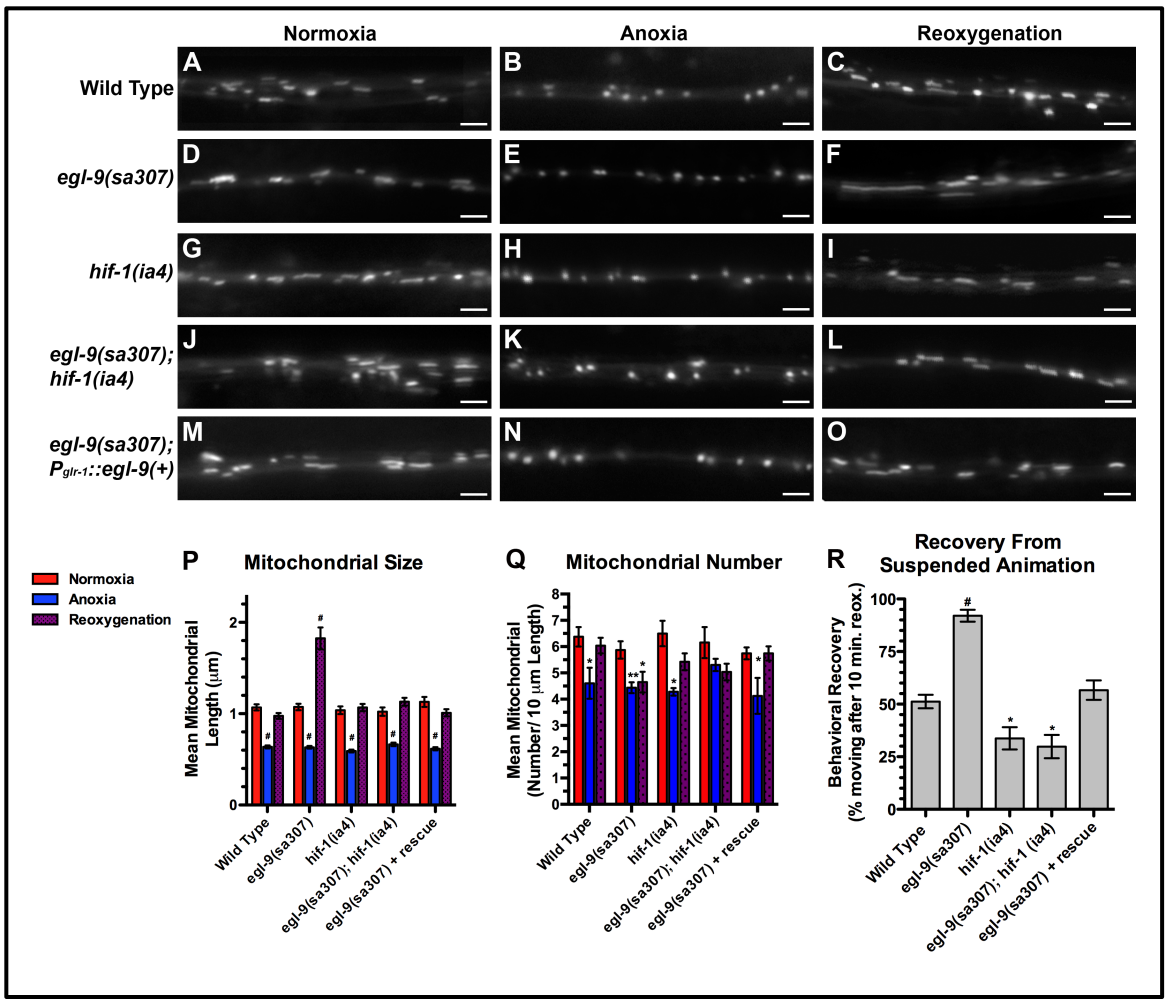
Normoxia
Anoxia
Reoxygenation
Wild Type
egl-9(sa307)
hif-1(ia4)
egl-9(sa307); hif-1(ia4)
egl-9(sa307); Pglr-1::egl-9(+)
A
B
C
D
E
F
G
H
I
J
K
L
M
N
O
Normoxia
Anoxia
Reoxygenation
P
Mitochondrial Size
Mean Mitochondrial Length (μm)
Q
Mitochondrial Number
Mean Mitochondrial (Number/ 10 μm Length)
R
Recovery From Suspended Animation
Behavioral Recovery (% moving after 10 min. reox.)
Wild Type
egl-9(sa307)
hif-1(ia4)
egl-9(sa307); hif-1(ia4)
egl-9(sa307) + rescue

Figure 2-3

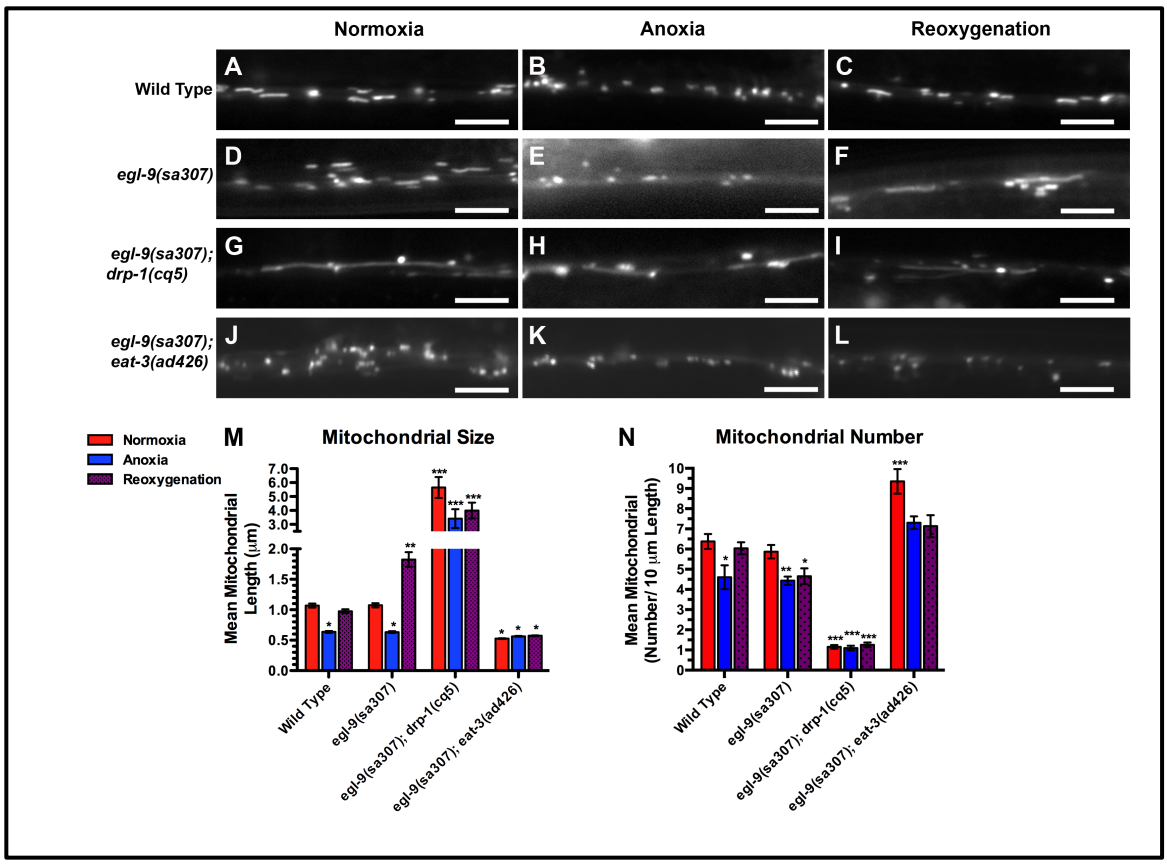
Normoxia
Anoxia
Reoxygenation
Wild Type
egl-9(sa307)
egl-9(sa307); drp-1(cq5)
egl-9(sa307); eat-3(ad426)
A
B
C
D
E
F
G
H
I
J
K
L
Normoxia
Anoxia
Reoxygenation
M
Mitochondrial Size
Mean Mitochondrial Length (μm)
N
Mitochondrial Number
Mean Mitochondrial (Number/ 10 μm Length)
Wild Type
egl-9(sa307)
egl-9(sa307); drp-1(cq5)
egl-9(sa307); eat-3(ad426)

Figure 2-4

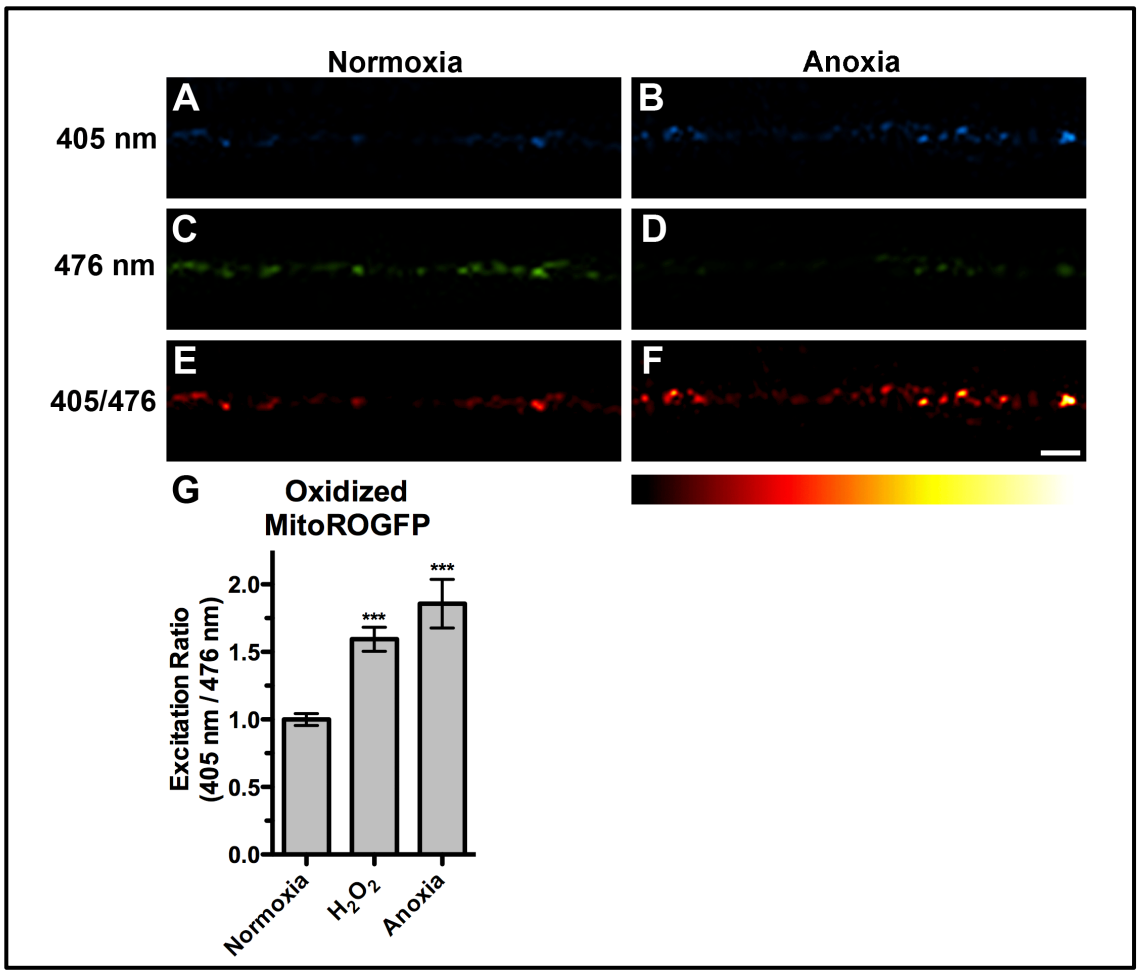
Normoxia
Anoxia
405 nm
476 nm
405/476
A
B
C
D
E
F
G
Oxidized
MitoROGFP
Excitation Ratio
(405 nm / 476 nm)
2.0
1.5
1.0
0.5
0.0
***
***
Normoxia
H2O2
Anoxia

Figure 2-5

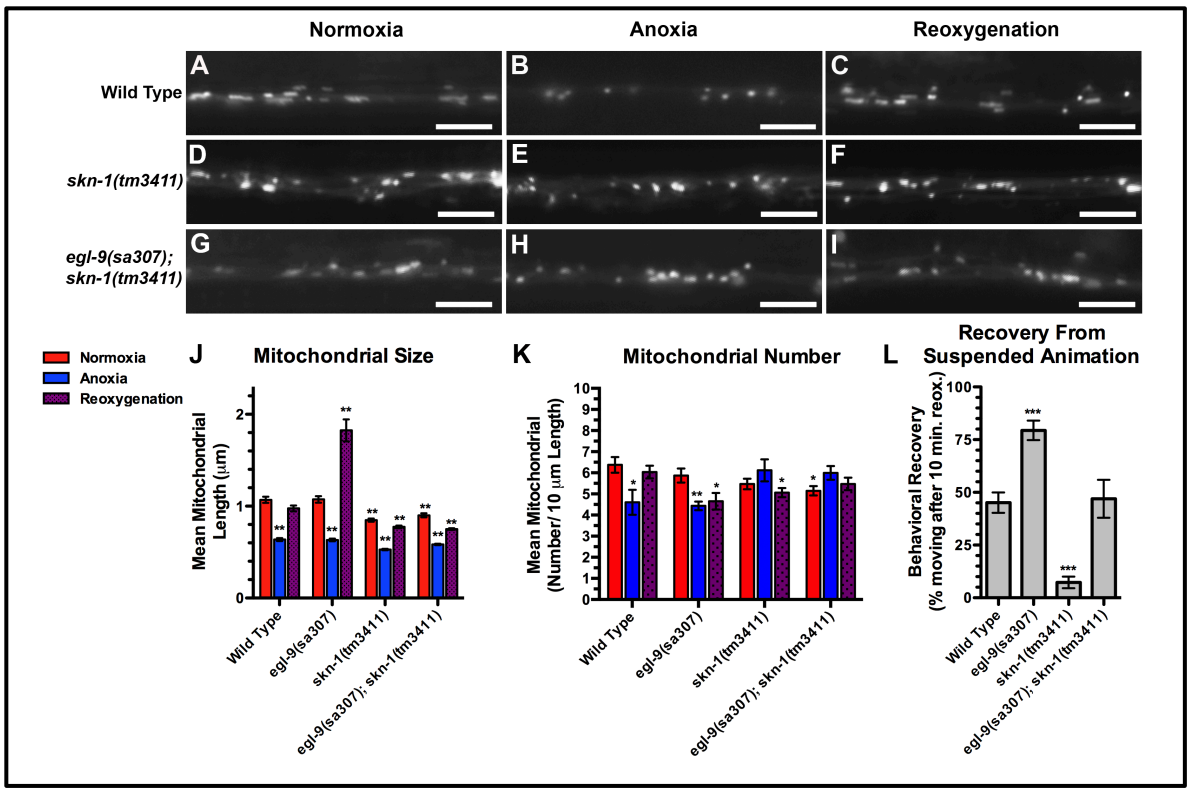
Normoxia
Anoxia
Reoxygenation
Wild Type
skn-1(tm3411)
egl-9(sa307); skn-1(tm3411)
A
B
C
D
E
F
G
H
I
Normoxia
Anoxia
Reoxygenation
J
Mitochondrial Size
Mean Mitochondrial Length (μm)
K
Mitochondrial Number
Mean Mitochondrial (Number/ 10 μm Length)
L
Recovery From Suspended Animation
Behavioral Recovery (% moving after 10 min. reox.)
Wild Type
egl-9(sa307)
skn-1(tm3411)
egl-9(sa307); skn-1(tm3411)

Figure 2-6

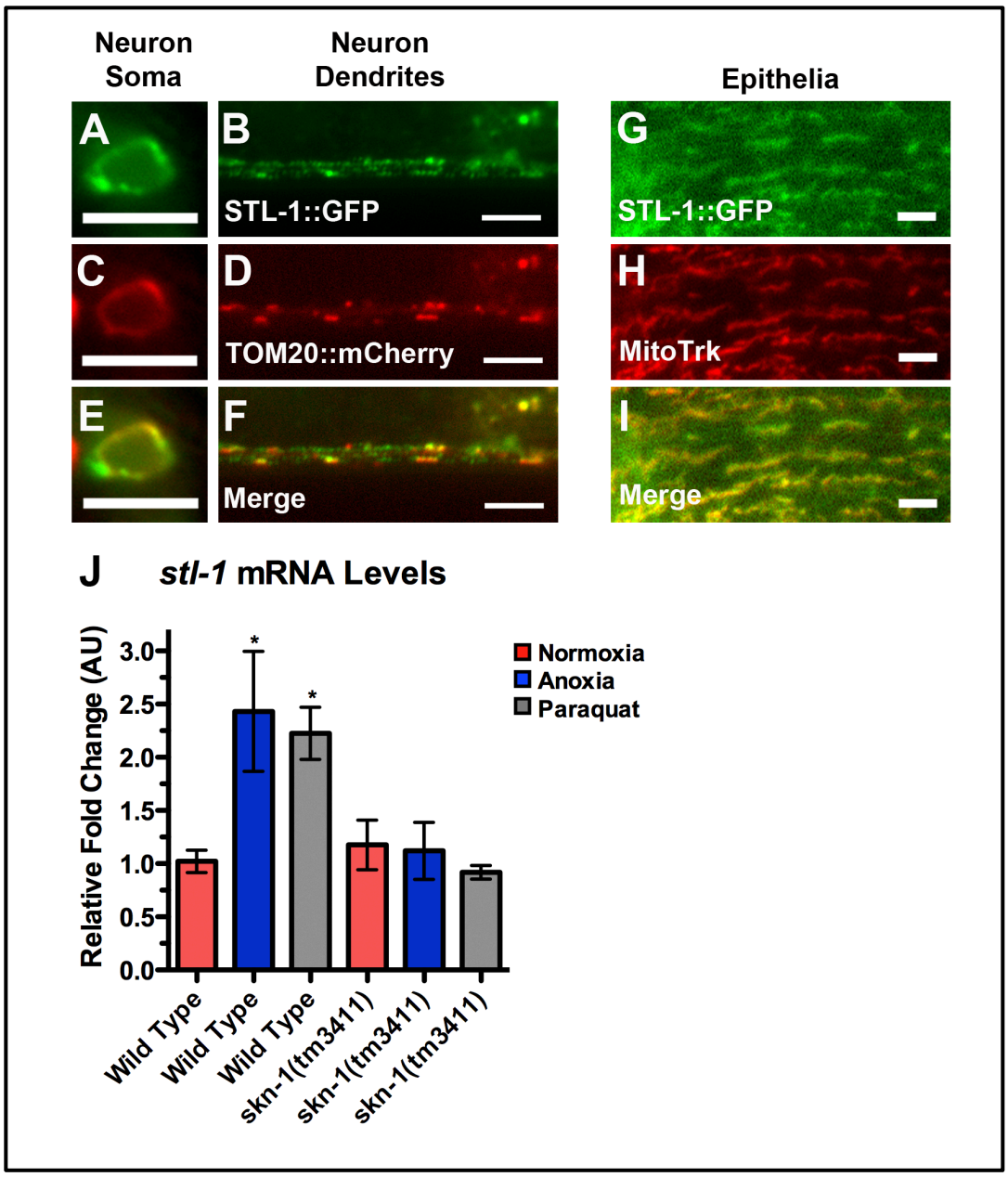
Neuron Soma
Neuron Dendrites
Epithelia
A
B
STL-1::GFP
G
STL-1::GFP
C
D
TOM20::mCherry
H
MitoTrk
E
F
Merge
I
Merge
J
stl-1 mRNA Levels
Relative Fold Change (AU)
3.0
2.5
2.0
1.5
1.0
0.5
0.0
*
*
Normoxia
Anoxia
Paraquat
Wild Type
Wild Type
Wild Type
skn-1(tm3411)
skn-1(tm3411)
skn-1(tm3411)

Figure 2-7

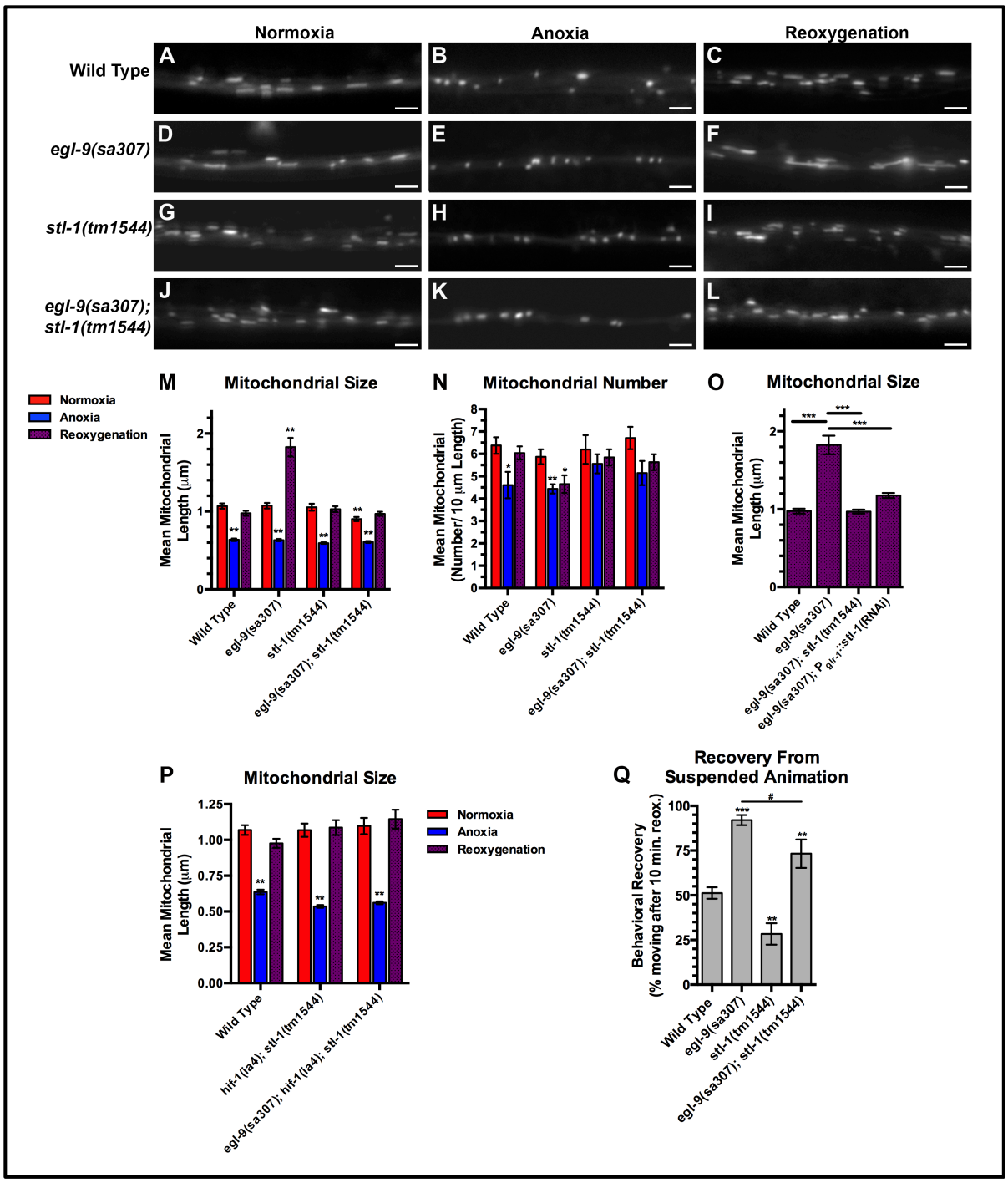
Normoxia
Anoxia
Reoxygenation
Wild Type
egl-9(sa307)
stl-1(tm1544)
egl-9(sa307); stl-1(tm1544)
A
B
C
D
E
F
G
H
I
J
K
L
M
Mitochondrial Size
Mean Mitochondrial Length (μm)
Wild Type
egl-9(sa307)
stl-1(tm1544)
egl-9(sa307); stl-1(tm1544)
N
Mitochondrial Number
Mean Mitochondrial (Number/ 10 μm Length)
O
Mitochondrial Size
egl-9(sa307); stl-1(tm1544)
egl-9(sa307); Pgly-1::stl-1(RNAi)
P
Mitochondrial Size
hif-1(ia4); stl-1(tm1544)
egl-9(sa307); hif-1(ia4); stl-1(tm1544)
Q
Recovery From Suspended Animation
Behavioral Recovery (% moving after 10 min. reox.)

Figure 2-8

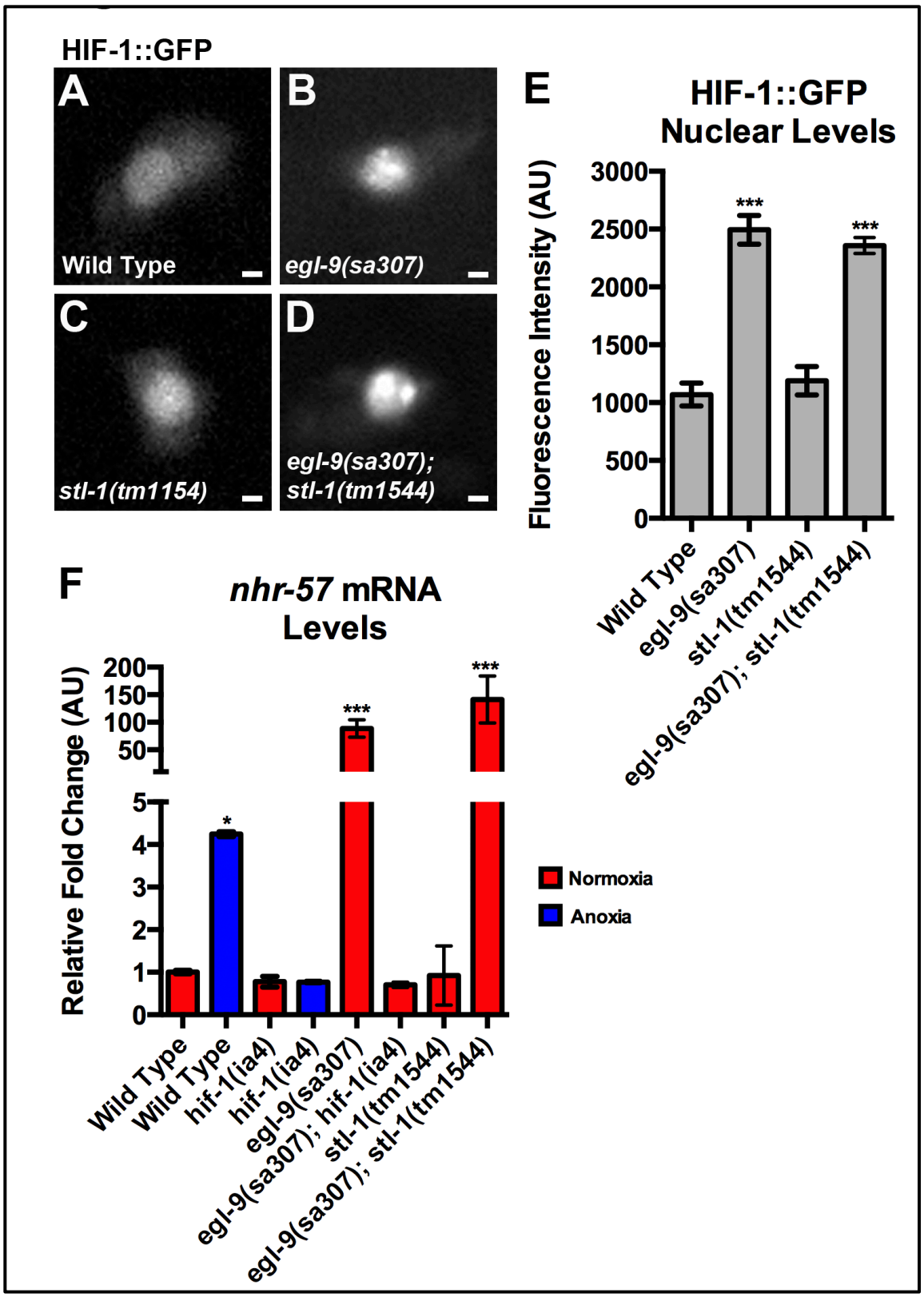
HIF-1::GFP
A
Wild Type
B
egl-9(sa307)
C
stl-1(tm1154)
D
egl-9(sa307);
stl-1(tm1544)
E
HIF-1::GFP
Nuclear Levels
Fluorescence Intensity (AU)
3000
2500
2000
1500
1000
500
0
***
***
Wild Type
egl-9(sa307)
stl-1(tm1544)
egl-9(sa307); stl-1(tm1544)
F
nhr-57 mRNA
Levels
Relative Fold Change (AU)
200
150
100
50
5
4
3
2
1
0
*
***
***
Normoxia
Anoxia
Wild Type
Wild Type
hif-1(ia4)
hif-1(ia4)
egl-9(sa307)
egl-9(sa307); hif-1(ia4)
stl-1(tm1544)
egl-9(sa307); stl-1(tm1544)

Figure 2-9

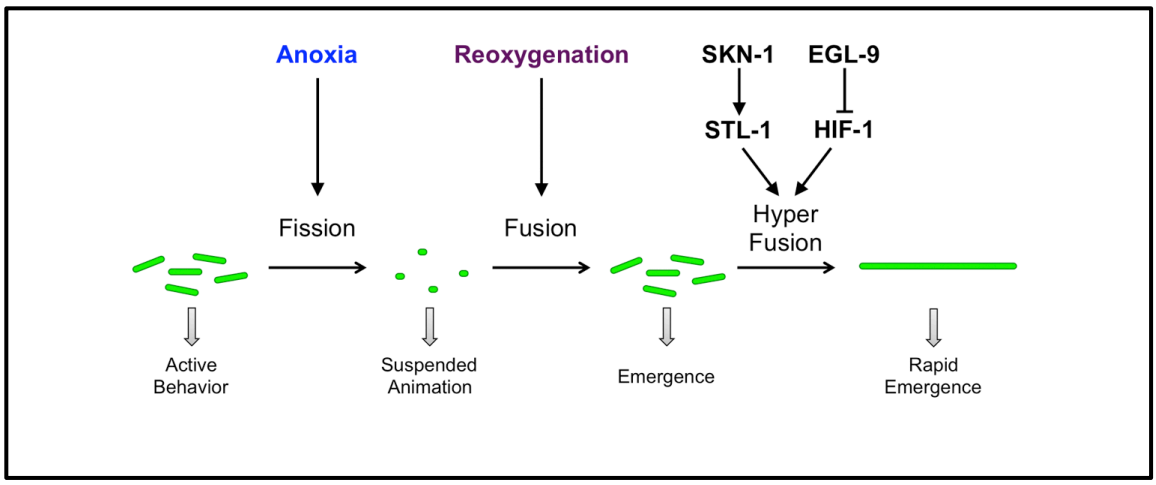


Figure 2-10

## IX. Figure Legends

Figure 2-1. Anoxia promotes suspended animation and eventually death in *C. elegans* (A) Protocol for *C. elegans* anoxia treatment. The x-axis indicates time (in days since fertilization) and developmental stage ("EM" for embryo, "L2" and "L4" for respective larval stages, and "A1-A6" for the indicated day of mature adulthood). Boxes indicate the treatment during that particular period, with red indicating exposure to a normoxic environment (or the 1-day reoxygenation, labeled as "Re") and blue indicating exposure to an anoxic environment. (B) Mean percentage of animals surviving after the given exposure time to anoxia. Error bars indicate SEM. (C) Mean percentage of animals moving (i.e., recovered from suspended animation) at the given time point following reoxygenation (post-anoxia). Individually plotted lines represent recovery following 12 (filled squares), 24 (filled triangles), 36 (empty triangles), and 48 (empty circles) hours of anoxia exposure. N=15-35 animals per condition and/or genotype.

Figure 2-2. Anoxia promotes DRP-1-dependent mitochondrial fission.
The fluorescence of MitoGFP was observed along ventral cord neurites of (A,B,C) wild-type animals, (D,E,F) *drp-1(cq5)* mutants, and (G,H,I) *eat-3(ad426)* mutants under

conditions of (A,D,G) normoxia, (B,E,H) following 24 hours of anoxia, or (C,F,I) following 3 hours of reoxygenation post-anoxia. (J,K) Quantification of the mean (J) length and (K) number of mitochondria along the ventral cord for the indicated genotypes and conditions. Red bars indicate normoxia, blue bars indicate anoxia, and purple stippled bars indicate reoxygenation. ANOVA followed by Dunnett's multiple comparison to wild type, normoxia (*p<0.05, **p<0.01, ***p<0.001). N=15-35 animals per condition and/or genotype. Error bars indicate SEM. Bar, 5 μm.

Figure 2-3. The hypoxia response pathway regulates mitochondrial hyperfusion upon anoxia recovery.

The fluorescence of MitoGFP was observed along ventral cord neurites of (A,B,C) wild-type animals, (D,E,F) *egl-9(sa307)* mutants, (G,H,I) *hif-1(ia4)* mutants, (J,K,L) *egl-9(sa307) hif-1(ia4)* double mutants, and (M,N,O) *egl-9* mutants with a transgene expressing the wild-type EGL-9A cDNA from the *glr-1* promoter. Conditions included (A,D,G,J,M) normoxia, (B,E,H,K,N) following 24 hours of anoxia, or (C,F,I,L,O) following 3 hours of reoxygenation post-anoxia. (P,Q) Quantification of the mean (P) length and (Q) number of mitochondria along the ventral cord for the indicated genotypes and conditions. (R) Quantification of behavioral recovery (number of animals moving after 10 minutes of reoxygenation) of animals following 24 hours anoxia. Red bars indicate normoxia, blue bars indicate anoxia, and purple stippled bars indicate reoxygenation. ANOVA followed by Dunnett's multiple comparison to wild type, normoxia (#p<0.001, **p<0.01, *p<0.05). N=15-35 animals per condition and/or genotype. Error bars indicate SEM. Bar, 5 μm.

Figure 2-4. Anoxia-induced mitochondrial hyperfusion requires the canonical mitochondrial fusion machinery.

The fluorescence of MitoGFP was observed along ventral cord neurites of (A,B,C) wild-type animals, (D,E,F) *egl-9(sa307)* mutants, (G,H,I) *egl-9(sa307) drp-1(cq5)* double mutants, and (J,K,L) *egl-9(sa307) eat-3(ad426)* double mutants under conditions of (A,D,G,J) normoxia, (B,E,H,K) following 24 hours of anoxia, or (C,F,I,L) following 3 hours of reoxygenation post-anoxia. (M,N) Quantification of the mean (M) length and (N) number of mitochondria along the ventral cord for the indicated genotypes and conditions. Red bars indicate normoxia, blue bars indicate anoxia, and purple stippled bars indicate reoxygenation. ANOVA followed by Dunnett's multiple comparison to wild type, normoxia (***$p<0.001$, **$p<0.01$, *$p<0.05$). N=15-35 animals per condition and/or genotype. Error bars indicate SEM. Bar, 5 μm.

Figure 2-5. Anoxia induced mitochondrial oxidative stress

The fluorescence of MitoROGFP emitted at a 510 nm wavelength was captured from mitochondria along ventral cord neurites illuminated with either (A,B) 405 nm or (C,D) 476 nm light from animals either under (A,C,E) normoxic conditions or (B,D,F) anoxic conditions. (E,F) Ratiometric images were generated from epifluorescence excited by 405 nm light relative to epifluorescence excited by 476 nm light. The ratio has been false colored with the indicated heat map, with high intensity indicative of ROGFP fluorescence in a more oxidative environment. (G) Quantification of mean light ratios evoked by the two excitation wavelengths at individual mitochondria from animals exposed to the given conditions. ANOVA followed by Dunnett's multiple comparison to animals exposed to normoxia (***$p<0.001$). N=10-15 animals per condition. Error bars indicate SEM. Bar, 5 μm.

Figure 2-6. SKN-1 is required for anoxia-induced mitochondrial hyperfusion.
The fluorescence of MitoGFP was observed along ventral cord neurites of (A,B,C) wild-type animals, (D,E,F) *skn-1(tm3411)* mutants, and (G,H,I) *egl-9(sa307) skn-1(tm3411)* double mutants under conditions of (A,D,G) normoxia, (B,E,H) following 24 hours of anoxia, or (C,F,I) following 3 hours of reoxygenation post-anoxia. (J,K) Quantification of the mean (J) length and (K) number of mitochondria along the ventral cord for the indicated genotypes and conditions. (L) Quantification of behavioral recovery (number of animals moving after 10 minutes of reoxygenation) of animals following 24 hours anoxia. Red bars indicate normoxia, blue bars indicate anoxia, and purple stippled bars indicate reoxygenation. ANOVA followed by Dunnett's multiple comparison to wild type, normoxia (***p<0.001, **p<0.01, *p<0.05). N=15-35 animals per condition and/or genotype. Error bars indicate SEM. Bar, 5 μm.

Figure 2-7. STL-1 resides at mitochondria and is regulated by SKN-1.
The fluorescence of (A,B) STL-1::GFP from a $P_{glr\text{-}1}$*::STL-1::GFP* transgene, and (C,D) TOM20::mCherry from a $P_{glr\text{-}1}$*::TOM20::mCherry* transgene, was observed in (A,C,E) command interneuron cell bodies, including PVC, and (B,D,F) ventral cord neurites of wild-type animals. (E,F) Merged images. The fluorescence of (G) STL-1::GFP from a $P_{stl\text{-}1}$*::STL-1::GFP* transgene was observed in the hypodermal epithelia of wild-type animals stained with (H) MitoTracker Red. (I) Merged image. (J) Mean levels of *stl-1* mRNA (relative to wild type) as measured by qRT-PCR in the indicated genotypes and conditions. Red bars indicate normoxia, blue bars indicate anoxia, and gray bars indicate paraquat treatment. Bar, 5 μm.

Figure 2-8. STL-1 is required for anoxia-induced mitochondrial hyperfusion.
The fluorescence of MitoGFP was observed along ventral cord neurites of (A,B,C) wild-type animals, (D,E,F) *egl-9(sa307)* mutants, (G,H,I) *stl-1(tm1544)* mutants, and (J,K,L) *egl-9(sa307) stl-1(tm1544)* double mutants under conditions of (A,D,G,J) normoxia, (B,E,H,K) following 24 hours of anoxia, or (C,F,I,L) following 3 hours of reoxygenation post-anoxia. (M-P) Quantification of the mean (M,O,P) length and (N) number of mitochondria along the ventral cord for the indicated genotypes and conditions. (Q) Quantification of behavioral recovery (number of animals moving after 10 minutes of reoxygenation) of animals following 24 hours anoxia. Red bars indicate normoxia, blue bars indicate anoxia, and purple stippled bars indicate reoxygenation. ANOVA followed by Dunnett's multiple comparison to wild type, normoxia (***$p<0.001$), or by Bonferoni's multiple comparison test for the indicated comparison (#$p<0.01$). N=15-35 animals per condition and/or genotype. Error bars indicate SEM. Bar, 5 μm.

Figure 2-9. STL-1 is not part of the EGL-9/HIF-1 pathway.
(A-D) The fluorescence of HIF-1::GFP from the PVC neuron cell body of (A) wild-type animals, (B) *egl-9(sa307)* mutants, (C) *stl-1(tm1544)* mutants, and (D) *egl-9(sa307) stl-1(tm1544)* double mutants. (E) Quantification of the mean fluorescence level in the nuclei for the indicated genotypes under normoxic conditions. (F) Mean levels of *nhr-57* mRNA (relative to wild type) as measured by qRT-PCR in the indicated genotypes and conditions. Red bars indicate normoxia and blue bars indicate anoxia. ANOVA followed by Dunnett's multiple comparison to wild type, normoxia (*$p<0.05$, ***$p<0.001$). N=3-5 replicates per condition and/or genotype. Error bars indicate SEM. Bar, 1 μm.

Figure 2-10. Model for anoxia-induced mitochondrial hyperfusion.
Under conditions of normoxia in wild-type neurons, mitochondria undergo a balance of fission and fusion. Exposure to anoxia shifts the balance towards smaller and fewer mitochondria by promoting the canonical fission process. Reoxygenation shifts the balance back towards elongated mitochondria by promoting the canonical fusion process. Depending on the dual activities of the hypoxia response pathway (EGL-9 and HIF-1) and the oxidative stress pathway (SKN-1 and STL-1), reoxygenation can trigger hyperfusion, rapidly resulting in enlarged mitochondria. Mitochondrial dynamics in turn affect the suspended animation behavior of the animal. Hyperfused mitochondria, perhaps through a more efficient generation of ATP, allow neurons to rapidly resume function and rapidly re-emerge from suspended animation. Green ellipses indicate mitochondria distributed along neurites. Arrows indicate stimulatory interactions, whereas T-bars indicate inhibitory interactions.

## X. Supplemental Figures

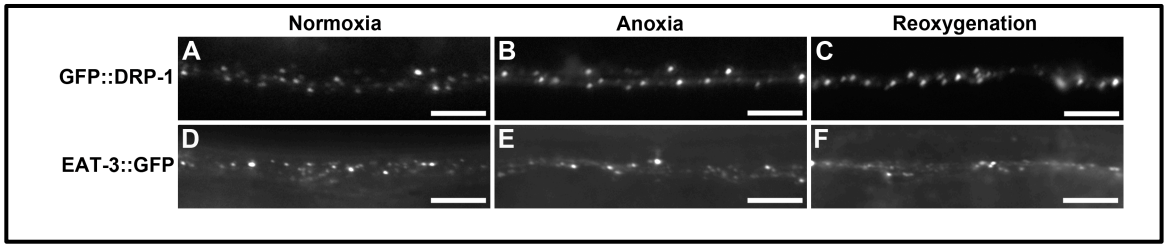


Figure 2-S1

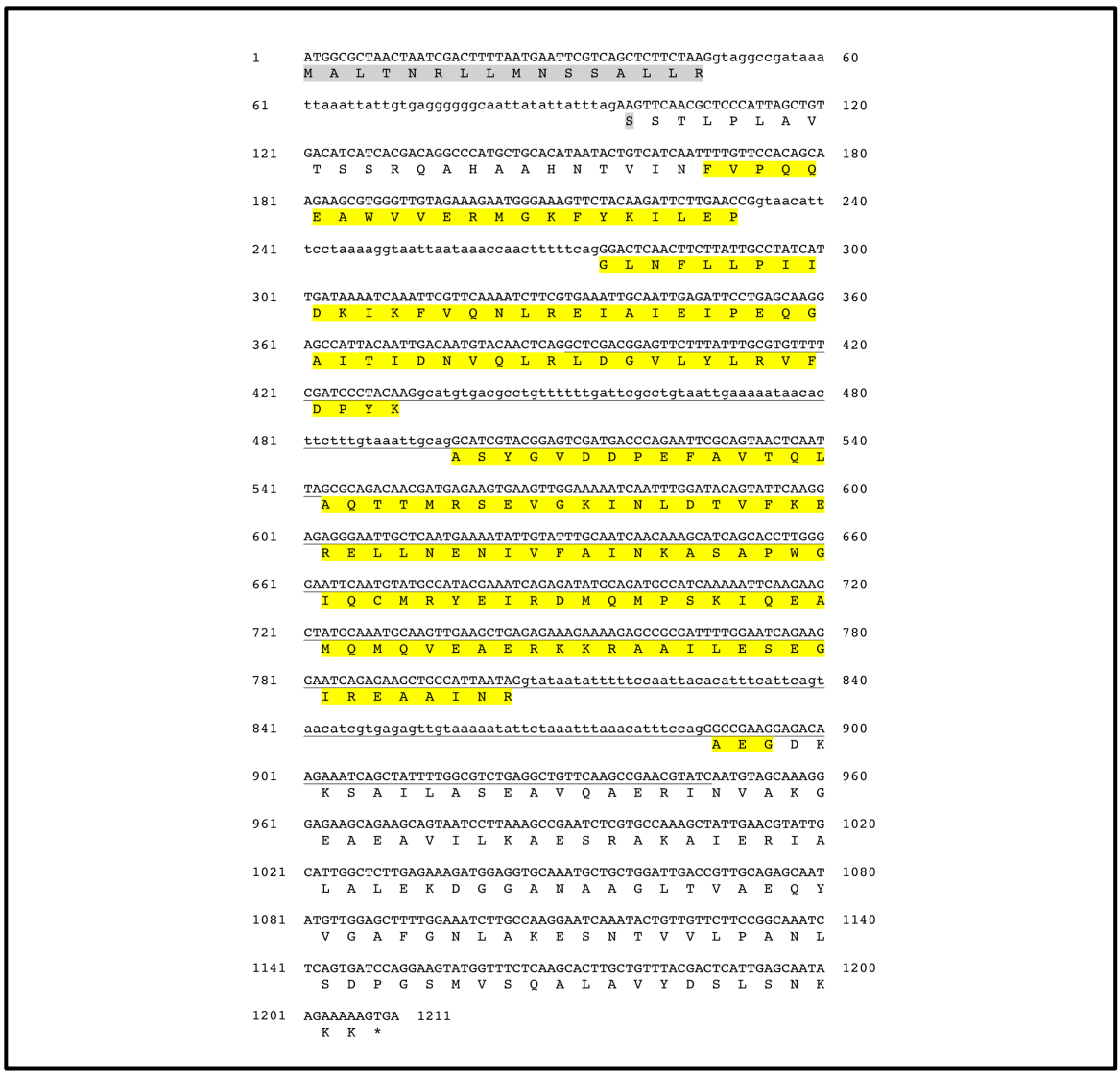
1 ATGGCGCTAACTAATCGACTTTTAATGAATTCGTCAGCTCTTCTAAGgtaggccgataaa 60
M A L T N R L L M N S S A L L R
61 ttaaattattgtgaggggggcaattatattatttagAAGTTCAACGCTCCCATTAGCTGT 120
S S T L P L A V
121 GACATCATCACGACAGGCCCATGCTGCACATAATACTGTCATCAATTTTGTTCCACAGCA 180
T S S R Q A H A A H N T V I N F V P Q Q
181 AGAAGCGTGGGTTGTAGAAAGAATGGGAAAGTTCTACAAGATTCTTGAACCGgtaacatt 240
E A W V V E R M G K F Y K I L E P
241 tcctaaaaggtaattaataaaccaacttttttcagGGACTCAACTTCTTATTGCCTATCAT 300
G L N F L L P I I
301 TGATAAAATCAAATTCGTTCAAAATCTTCGTGAAATTGCAATTGAGATTCCTGAGCAAGG 360
D K I K F V Q N L R E I A I E I P E Q G
361 AGCCATTACAATTGACAATGTACAACTCAGGCTCGACGGAGTTCTTTATTTGCGTGTTTT 420
A I T I D N V Q L R L D G V L Y L R V F
421 CGATCCCTACAAGgcatgtgacgcctgtttttttgattcgcctgtaattgaaaaataacac 480
D P Y K
481 ttctttgtaaattgcagGCATCGTACGGAGTCGATGACCCAGAATTCGCAGTAACTCAAT 540
A S Y G V D D P E F A V T Q L
541 TAGCGCAGACAACGATGAGAAGTGAAGTTGGAAAAATCAATTTGGATACAGTATTCAAGG 600
A Q T T M R S E V G K I N L D T V F K E
601 AGAGGGAATTGCTCAATGAAAATATTGTATTTGCAATCAACAAAGCATCAGCACCTTGGG 660
R E L L N E N I V F A I N K A S A P W G
661 GAATTCAATGTATGCGATACGAAATCAGAGATATGCAGATGCCATCAAAAATTCAAGAAG 720
I Q C M R Y E I R D M Q M P S K I Q E A
721 CTATGCAAATGCAAGTTGAAGCTGAGAGAAAGAAAAGAGCCGCGATTTTGGAATCAGAAG 780
M Q M Q V E A E R K K R A A I L E S E G
781 GAATCAGAGAAGCTGCCATTAATAGgtataatatttttccaattacacatttcattcagt 840
I R E A A I N R
841 aacatcgtgagagttgtaaaaatattctaaatttaaacatttccagGGCCGAAGGAGACA 900
A E G D K
901 AGAAATCAGCTATTTTGGCGTCTGAGGCTGTTCAAGCCGAACGTATCAATGTAGCAAAGG 960
K S A I L A S E A V Q A E R I N V A K G
961 GAGAAGCAGAAGCAGTAATCCTTAAAGCCGAATCTCGTGCCAAAGCTATTGAACGTATTG 1020
E A E A V I L K A E S R A K A I E R I A
1021 CATTGGCTCTTGAGAAAGATGGAGGTGCAAATGCTGCTGGATTGACCGTTGCAGAGCAAT 1080
L A L E K D G G A N A A G L T V A E Q Y
1081 ATGTTGGAGCTTTTGGAAATCTTGCCAAGGAATCAAATACTGTTGTTCTTCCGGCAAATC 1140
V G A F G N L A K E S N T V V L P A N L
1141 TCAGTGATCCAGGAAGTATGGTTTCTCAAGCACTTGCTGTTTACGACTCATTGAGCAATA 1200
S D P G S M V S Q A L A V Y D S L S N K
1201 AGAAAAAGTGA 1211
K K *

Figure 2-S2

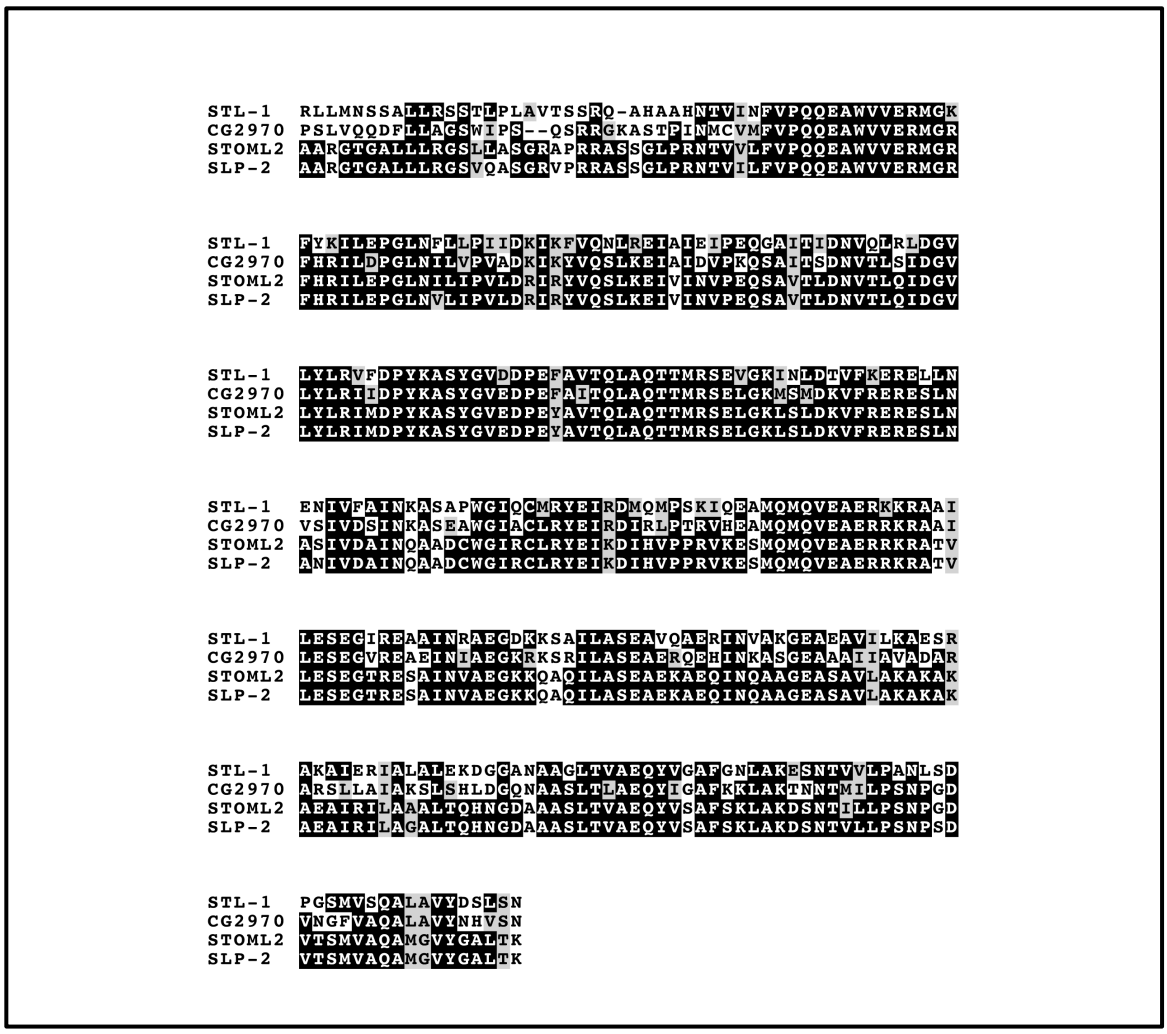
STL-1 RLLMNSSALLRSSTLPLAVTSSRQ-AHAAHNTVINFVPQQEAWVVERMGK
CG2970 PSLVQQDFLLAGSWIPS--QSRRGKASTPINMCVMFVPQQEAWVVERMGR
STOML2 AARGTGALLLRGSLLASGRAPRRASSGLPRNTVVLFVPQQEAWVVERMGR
SLP-2 AARGTGALLLRGSVQASGRVPRRASSGLPRNTVILFVPQQEAWVVERMGR
STL-1 FYKILEPGLNFLLPIIDKIKFVQNLREIAIEIPEQGAITIDNVQLRLDGV
CG2970 FHRILDPGLNILVPVADKIKYVQSLKEIAIDVPKQSAITSDNVTLSIDGV
STOML2 FHRILEPGLNILIPVLDRIRYVQSLKEIVINVPEQSAVTLDNVTLQIDGV
SLP-2 FHRILEPGLNVLIPVLDRIRYVQSLKEIVINVPEQSAVTLDNVTLQIDGV
STL-1 LYLRVFDPYKASYGVDDPEFAVTQLAQTTMRSEVGKINLDTVFKERELLN
CG2970 LYLRIIDPYKASYGVEDPEFAITQLAQTTMRSELGKMSMDKVFRERESLN
STOML2 LYLRIMDPYKASYGVEDPEYAVTQLAQTTMRSELGKLSLDKVFRERESLN
SLP-2 LYLRIMDPYKASYGVEDPEYAVTQLAQTTMRSELGKLSLDKVFRERESLN
STL-1 ENIVFAINKASAPWGIQCMRYEIRDMQMPSKIQEAMQMQVEAERKKRAAI
CG2970 VSIVDSINKASEAWGIACLRYEIRDIRLPTRVHEAMQMQVEAERRKRAAI
STOML2 ASIVDAINQAADCWGIRCLRYEIKDIHVPPRVKESMQMQVEAERRKRATV
SLP-2 ANIVDAINQAADCWGIRCLRYEIKDIHVPPRVKESMQMQVEAERRKRATV
STL-1 LESEGIREAAINRAEGDKKSAILASEAVQAERINVAKGEAEAVILKAESR
CG2970 LESEGVREAEINIAEGKRKSRILASEAERQEHINKASGEAAAIIAVADAR
STOML2 LESEGTRESAINVAEGKKQAQILASEAEKAEQINQAAGEASAVLAKAKAK
SLP-2 LESEGTRESAINVAEGKKQAQILASEAEKAEQINQAAGEASAVLAKAKAK
STL-1 AKAIERIALALEKDGGANAAGLTVAEQYVGAFGNLAKESNTVVLPANLSD
CG2970 ARSLLAIAKSLSHLDGQNAASLTLAEQYIGAFKKLAKTNNTMILPSNPGD
STOML2 AEAIRILAAALTQHNGDAAASLTVAEQYVSAFSKLAKDSNTILLPSNPGD
SLP-2 AEAIRILAGALTQHNGDAAASLTVAEQYVSAFSKLAKDSNTVLLPSNPSD
STL-1 PGSMVSQALAVYDSLSN
CG2970 VNGFVAQALAVYNHVSN
STOML2 VTSMVAQAMGVYGALTK
SLP-2 VTSMVAQAMGVYGALTK

Figure 2-S3

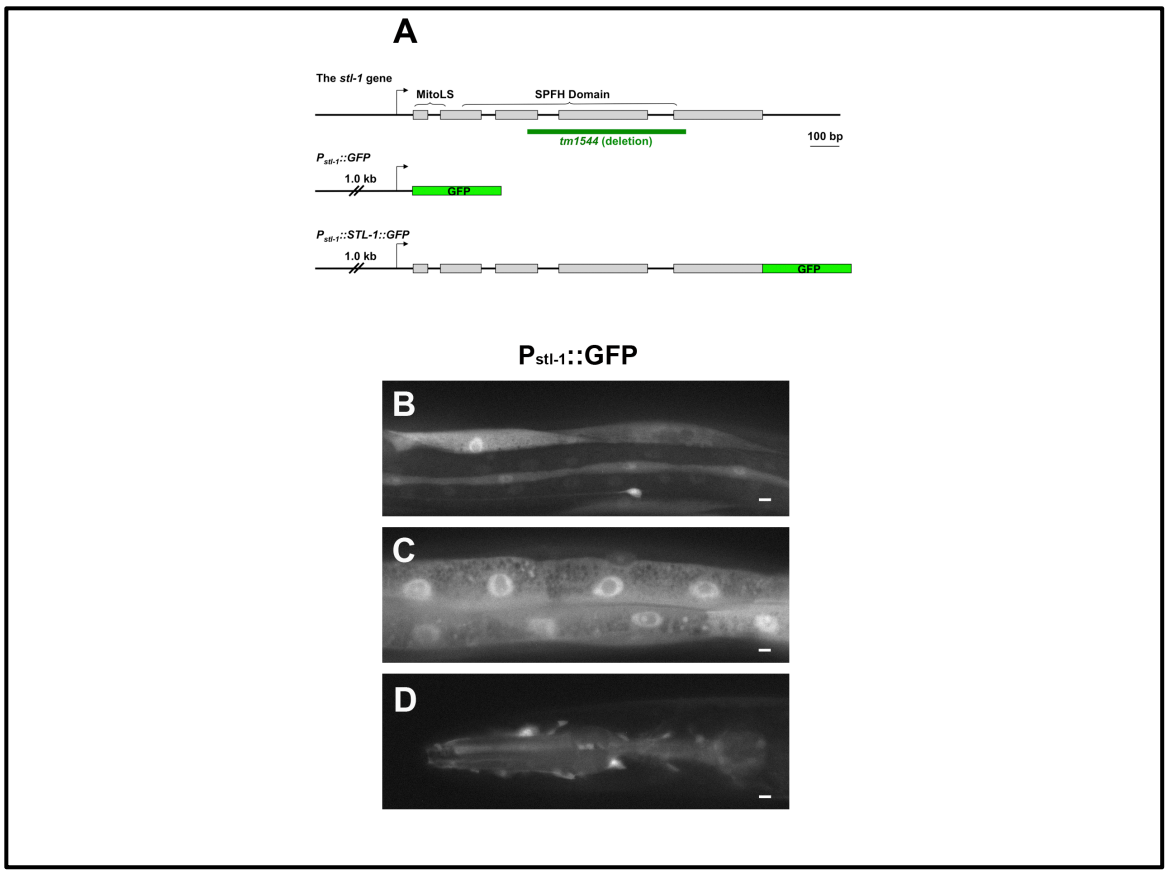


Figure 2-S4

## XI. Supplemental Figure Legends

Figure 2-S1. Anoxia does not grossly alter the recruitment of mitochondrial dynamics machinery.

The fluorescence from either (A-C) GFP::DRP-1 or (D-F) EAT-3::GFP was observed along ventral cord neurites of wild-type nematodes under conditions of (A,D) normoxia, (B,E) following 24 hours of anoxia, or (C,F) following 8 hours of reoxygenation after anoxic exposure. Bar, 5 μm.

Figure 2-S2. Organization of the *stl-1* gene.

Genomic sequences of the *stl-1* gene, from the start of translation to the end of translation, are shown, with DNA on the top line and protein sequence listed below. For DNA, capital letters indicate exonic sequences. Numbers are based on nucleotides starting from the ATG. Protein sequence highlighted in gray indicates the predicted mitochondrial localization signal. Protein sequence highlighted in yellow indicates the predicted SPFH domain. Underlined DNA sequences indicate the nucleotides missing in the *tm1544* deletion mutant.

Figure 2-S3. STL-1 is a prohibitin-like ortholog for mitochondrial resident SLP-2.

The amino acid alignment of *C. elegans* STL-1 with its putative homologs in humans (STOML2), mice (SLP-2), and *Drosophila* (CG2970).

Figure 2-S4. STL-1 is broadly expressed in most tissues.

(A) Schematic of *stl-1* genomic DNA organization and associated transgenes for examining STL-1 expression and subcellular localization. Boxes indicate coding sequences within exons. The arrows indicate the start site of transcription. Brackets indicate regions that encode the indicated protein domains. The green line indicates the region of genomic DNA deleted in the *tm1544* mutant. The green box indicates GFP sequences for the indicated reporter transgenes. (B-D) Fluorescence from $P_{stl\text{-}1}$*::GFP* in (B) body wall muscles, (C) intestinal epithelia, and (D) pharynx and head neurons. Bar, 5μm.

# Chapter III- Identification of Novel Genes that Participate in Mitochondrial Transport and Dynamics

## I. Abstract

Mitochondria serve important and necessary functions in the eukaryotic cell. They exist in a dynamic equilibrium of fusion, fission and mitophagy. In addition, mitochondria, especially in polarized cells like neurons need to be transported to distal areas of need. All of these processes are not fully understood. Given the critical role of mitochondria in neuronal physiology, mitochondrial dysfunction contributes to the etiology of multiple neurological diseases. Identification of the factors that regulate or contribute to mitochondrial dynamics, transport, and mitophagy in neurons should help us further understand such diseases.

Identification of the factors that regulate or contribute to mitochondrial dynamics, transport, and mitophagy in neurons should help us to further understand such diseases. Here I identify genes that are working in conjunction with the dynamics machinery and motor proteins to both regulate mitochondrial morphology and transport within the cell. To identify these proteins, I conducted an F1 clonal screen using EMS mutagenesis. I isolated eleven different mutants, three of which are new alleles of the *drp-1* gene, three of which are mitochondrial fission mutants with a lesser degree of elongation, and three mutants that may be playing a role in mitochondrial transport.

With these isolated mutants we can then find the causative genes and further investigate how these genes are working in relation to fission and fusion or during the process mitochondrial transport.

## II. Introduction

Mitochondrial function is directly influenced by changes in fission/fusion dynamics, transport and mitophagy. We know some of the proteins that directly play a

role in the joining of mitochondrial membranes for fusion, in the recruitment and membrane scission during fission, and also in the transport of mitochondria. We do not fully understand what governs these proteins or how they interact with one another.

We use the model organism *C. elegans* to study mitochondria. These nematodes are transparent, allowing us to study their cells and organelles in vivo. Additionally, we can further understand how proteins participate and cooperate with each other during mitochondrial fission and fusion events and during transport. By using available alleles for known fission and fusion factors as well as motor proteins, we can see examples of mitochondrial defects in the dendritic and axons, including small and punctate size (fusion mutants), elongated size (fission mutants), and changes in the number of mitochondria (transport mutants).

Previous work in our lab showed that other non-canonical machinery can regulate mitochondrial dynamics. We have seen that in response to oxygen deprivation both the Hypoxia Response Pathway as well as SKN-1 and STL-1 can regulate mitochondrial dynamics in the *C. elegans* neuron (*22*). In addition, other non-canonical proteins have also been shown to regulate transport in the neuron as well. The *ric-7* gene, which is required for synaptic transmission, was also shown to interact with mitochondria and help with transport out of the cell body (*51*). This report also mentioned that *ric-7* does not play a role in other cell types in regard to mitochondrial distribution, suggesting that there are tissue-specific regulators of mitochondrial dynamics and transport. As these proteins were not identified for their role in mitochondrial dynamics and transport using conventional approaches in the field, it suggests that there could be additional proteins that also regulate these processes that could be uncovered through a genetic approach.

In order to ask what these new proteins are and how they function in these processes (and specifically in the neuron), we performed a genetic screen. This forward

genetic approach helped us find novel proteins that are mediate mitochondrial dynamics and transport. We isolated mutants with elongated mitochondria and with reduced numbers of mitochondria outside the cell body. In this section, I describe our screen as well as the mutants that were isolated.

## III. Materials and Methods

### Strains and Reagents

Animals were grown at 20ºC on standard NGM plates seeded with OP50 E. coli. Some strains were provided by the *Caenorhabditis* Genetics Center. The following strains were used: *drp-1(cq5), eat-3(ad426), unc-116(e2310), ric-7(n2657), odIs70[Pglr-1::MitoGFP, unc-119(+)]*, *C. elegans* N2, and CB4856 *C. elegans* Hawaiian. For mapping, the following strains were used to generate double reporter strains with our mitochondrial reporter *odIs70*: EG7835 I, EG7866 II, EG7898 III, EG7911 IV, EG7944 V, EG7943 V, EG7988 X. All of these strains contain the reporter *Peft-3p::TdTomato::H2B::unc-54* that was mapped to the center of each chromosome.

### EMS Mutagenesis

The *odIs70* mitochondrial reporter strain was used as a starter strain to perform the mutagenesis screen. Synchronized worms were grown by a bleaching method of synchronization and seeding to NGM plates. At the L4 stage they were washed off and collected in 15 mL centrifuge tube using glass Pasteur pipettes to avoid loss. Washing steps were done by centrifuging to pellet animals, removing supernatant without touching the pellet and adding fresh M9. These first washes were done twice. Pelleted worms were resuspended with 3 mL of fresh M9 buffer. To prepare tubes for deactivation of EMS, 10 mL 1N NaOH were added to the 15mL centrifuge tubes for waste (5 wash waste tubes) and in one glass conical centrifuge 1 mL of M9 for the

mutagenesis. Working in a chemical hood, 20 ul of EMS (Ethyl methanesulfonate, Sigma # M0880) were added to the glass conical tube that had the M9 buffer, 3 mL of worm mixture was then added, capped and secured with parafilm. This worm/EMS mixture was incubated at room temperature on a nutator inside the hood for 4 hours. Final concentration of EMS was 47 mM.

After incubation and using a dedicated centrifuge to spin the worms down, supernatant containing EMS was aspirated with disposable pipettes and discarded in the first inactivation waste tube. 4mL of M9 were then added to the worm pellet to resuspend and mix. Worms were centrifuged to remove supernatant to be discarded in the second inactivation waste tube. Washes were done three additional times to ensure proper EMS removal. During last wash, worms were resuspended using 1mL of M9 and seeded to a clean NGM plate for recovery using a glass Pasteur pipette to avoid loss of animals.

After a 30 min recovery, 150 healthy-looking late L4 animals were picked to be use as P0s for that mutagenesis. The P0 plate was then incubated at 20$^{o}$C. The next day, 100 adult P0 animals were selected and transferred to new NGM plates (4 P0s per plate for a total of 25 plates) and incubated for 3 days.

From the P0 plates, single L4 animals (F1s) were selected to individual plates for self-fertilization. From each mutagenesis round performed, roughly 150-225 F1 plates were set up for screening to avoid potential issues due to: parent death, crawling out of the plate and lost, or contamination.

## Screening

Animals were screened using an inverted confocal microscope, Leica TCS SP2 microscope and MatTek 60 mm glass bottom dishes. Using 20 mM solution of levamisole in M9, a sample of the population from each F1 plate was screened by

partially washing a small area of the plate and decanting the worms in solution to a microcentrifuge tube. This population of worms (F2-F3) was then allowed to settle for a few minutes and then a sample was taken from the bottom of the tube and placed onto the plate glass slide. Using 63x magnification, the “sample drop” containing the animals was screened for any of the expected mitochondrial phenotypes. Any F1 plate that yielded a phenotype of interest was kept for confirmation using a secondary screening.

The secondary screen was done on an Epiflourescent Microscope. Using 5% agarose pads with 20 mM levamisole. 10-20 animals from the F1 plate were selected for confirmation. If a phenotype was observed again, the F1 plate was kept as containing a possible mutant found in the initial screen. If possible, animals were recovered from the pad to try and isolate a homozygose

From the F1 plates that were confirmed, approximately 25 animals were singled to find a homozygote mutant plate. The F1 plates were kept at 15 deg. Celsius until the mutant was considered “isolated” and frozen down. If homozygotes were not found, this step was then repeated again.

## Outcrossing

After isolating a homozygote line for the mutants, N2 wild type was used to outcross the strain and eliminate background mutations. For this, N2 males were crossed to L4 hermaphrodites. In the next generation, cross progeny males that had the mitochondrial reporter were picked and used to then cross to N2 hermaphrodites. The F1 generation of this second outcrossing that carried the mitochondrial reporter were then selected to self-fertilize. The following generation was then selected again for self-fertilization.

Any F2 plates with a 1:2:1 phenotype ratio was kept. The F3 generation was screened using 5% agarose pads to check for a homozygous animal. After finding the

mutant again, these were recovered and that F2 plate was used to select individual animals to self-fertilize once more. This process, of two outcrossing back to back, was repeated twice for a few of our mutants from the screen (Table 3-1)

The J-72 mutant presents a Dpy and Unc phenotype that is very strong. For this outcross, J-72 animal hermaphrodites were used with an abundance of males in order for mating to occur. The cross progeny males with a mitochondrial reporter were used for crossing to N2 hermaphrodites again. The progeny of this cross (F1) were selected based on the reporter and selected for self-fertilization. The plates that showed a 1:2:1 ratio was very easy to score because of the presence of Dpy and Unc worms. These plates were kept and the Dpy and Unc progeny were picked to self-fertilize the next generation. Once they gave enough progeny their phenotypes were scored. Both the Dpy and Unc phenotype were linked to the mitochondrial defect and this was confirmed during the outcrossing.

## Chromosomal linkage Mapping

Using the *TdTomato::H2B* fusion from the *eft-3* promoter, which result in red nuclei in the hypodermis we crossed into our mitochondrial reporter. Double reporter males were then used for crossing to our mutants. Crosses were performed to mutant hermaphrodites for each chromosome for the selected mutants. The cross progeny of was then selected based on the red balancer. These F1 progeny were selected for self-fertilization. The F2 generation was used for screening ratios of mitochondrial phenotype. The non-Red animals were mounted on 5% agarose pads and a 20mM levamisole drop to score. Assuming close linkage to the reporter if on the same chromosome these non-Red animals would all have the mitochondrial phenotype. Assuming the mutation is on another chromosome, only ¼ of non-Red animals would show the mitochondrial phenotype. Animals were scored for each cross and the results

were noted to make a definitive call after crossing to all chromosomal reporters (Table 3-2).

## Candidate-Based Screen

Literature search was done to find genes that were uncoordinated and that were located to the linkage group that our J-72 mutant mapped to. From the list of available genes (Table 3-4) we ordered available alleles. Because of the wide range of the "uncoordinated" phenotypes we narrowed the list even further and prioritized the genes that showed strong uncoordinated phenotypes. Based on this, we performed crosses of these strains to our mitochondrial reporter *odIs70* to see if any of these gave a phenocopy of what we see in mutant J-72.

## Complementation Testing

I performed complementation crosses with known alleles of *drp-1* for the mutants that showed strong elongation of mitochondria in the ventral nerve cord. The available alleles were: *drp-1(cq5)* and *drp-1(tm1108)* and these strains were crossed into our *odIs70* mitochondrial reporter. Crosses were set up with homozygous lines of the mutants: D-27, P-94, and N-64. Males of our known *drp-1* alleles were used to cross with hermaphrodites of our screen mutants. The F1 generation was then screened for the mitochondrial phenotype by selecting 50 animals. If the mutation failed to complement the allele, then the mutant phenotype will be seen in all animals screened. As a negative control, a cross of wild-type *odIs70* with our mutants and known alleles was also performed. In this case, the F1 generation would show that the wild-type strain would complement the mutation and give a wild-type phenotype. As a positive control, both known alleles were crossed to each other, the F1 generation would fail to

complement each other and the phenotype shown will be the elongated mitochondrial phenotype.

For the mutant J-72, the complementation cross was designed differently. The J-72 mutant is very uncoordinated and dumpy and the potential candidates were also similar in phenotype. Because of this we crossed these hermaphrodites (J-72, *unc-44*, and *unc-33*) to wild-type *odIs70* males. These heterozygous (Het) F1 hermaphrodites and males were used for the complementation cross. For example, a Het *unc-44*; *odIs70* male was crossed to a Het J-72; *odIs70* hermaphrodite. The F1 animals from this new cross are then screened for the mitochondrial phenotype as well as the uncoordinated and dumpy phenotypes. If the gene fails to complement the mutation, these phenotypes would be present in ¼ of the F1 generation. If the gene complements the mutation all of the F1 progeny will have wild-type phenotypes. As controls, we used the wild-type *odIs70* strain to cross into as well as its own Het J-72; *odIs70*.

### Sanger Sequencing

Oligos were designed to span the length of the gene and these could be used for amplification and sequencing (Table 3-3). Wild-type and mutant animals were lysed for use in the PCR amplification of the *drp-1* gene. Using a combination of oligos, we wanted to amplify sections that overlap each other. After amplification, 5 ul of the PCR samples was used to check on 1% Agarose gel with Ethidium Bromide to label DNA. Amplifications with a clear band, the remaining reaction was cleaned up with with Qiagen's QIAquick PCR Purification Kit (Cat. No. 28104). If multiple bands were found, a gel extraction was done using Qiagen's QIAquick Gel Extraction Kit (Cat. No. 28704).

All final DNA samples were then measured for the DNA concentration and sent to the sequencing facility Genewiz. Sequencing data received from them was then used

to align and check to the reference *drp-1* transcript (T12E12.4a), available via Wormbase.

## IV. Results

### Forward Mutagenesis Screen

We conducted the EMS mutagenesis to use for screening of novel genes that regulate mitochondrial dynamics and transport in the *C. elegans* neuron. We screened 2,449 F1 plates (4,898 haploid genomes). Because we expected phenotypes that showed either mitochondrial fusion defects (small mitochondria), mitochondria fission defects (large mitochondria), or defects in transport of mitochondria (fewer mitochondria or no mitochondria present in the ventral nerve cord), we had to validate the initial screen of the population, with a second screen of a smaller sample of the population. This was done to confirm these were true mutants and not false positives. This step proved to be very important because during the first rounds of screening most of the F1 plates that were kept based on phenotype of “smaller mitochondria” we ruled out as false positives during the second round of analysis. This is indicative how mitochondria can react based on stress-like factors like manipulation during the screen. We were very careful to score phenotypes during the second round and further to make sure the phenotypes were observed and could be homozygosed.

### Classes of mutants isolated

After the completion of the screen, we were able to isolate 11 mutants, with 6 mutants that showed elongated mitochondrial phenotypes, 3 that showed reduced mitochondria density in the ventral nerve cord, and 2 that showed phenotypes that were not mitochondrial related but were of potential interest to other projects in the lab (Figure 3-1). Within the elongated mitochondrial group, we found that three of these (D-27, N-64

and P-94) showed a strong phenotype, whereas the three others (B-104A, T-7, T-17) had milder phenotypes. The other three mutants (J-72, M-6 and V-128) showed a decrease of mitochondrial density in the ventral nerve cord. Finally, mutant O-101 showed ectopic expression of our mitochondrial reporter in non-neuronal cells, suggesting a mutation in a gene that restricts neuronal gene expression, and B-104B showed neurite outgrowth in the tail region, which our lab has recently showed is regulated by Wnt signaling and RPM-1.

## Outcrossing mutants

The EMS mutagen was used at a dose that usually triggers many mutations along each haploid genome besides just the one linked to the phenotype of interest. If a mutation causes a phenotype of interest, then there is still a need to homozygose the mutant and also to outcross it to a wild-type strain to eliminate background mutations. This is an important step because other background mutations can make the animals unhealthy and harder to propagate, and such mutations could also affect the phenotype itself. In our case, this step was useful because a few mutants showed other phenotypes that were found to be linked to the mitochondrial phenotype as well (Table 3-1). These additional phenotypes were found to be useful during outcrossing and also harder to score some aspects of the mitochondrial phenotype. In the case of J-72, this mutant showed a decrease in mitochondrial morphology but also an uncoordinated, dumpy and axonal guidance defect. Both the Dpy and Unc phenotypes were used during the outcrossing but the axonal guidance defect makes it harder to account for all of the neuronal processes that otherwise would be present in the ventral nerve cord (Figure 3-2). Because of this complication, we opted to quantify both the ventral nerve cord mitochondrial density and also the number of interneurons' dendritic axons that were found outside of the bundle. (Figure 3-2)

In the case of the V-128 mutant, after the outcrossing to wild type N2, in addition to the fewer mitochondria in the VNC we see that this mutant has a partial sterility phenotype as well as a gradient of mitochondrial density. The anterior VNC has more mitochondria than the posterior VNC.

After the outcrossing of the majority of our mutants we assigned these strain names from the Rongo Lab designation (Table 3-5). From here on we will be using both "od" designation and the original mutant name for ease of reference.

## Chromosomal Linkage Mapping Results

One of the first steps to uncovering the identity of the genes associated with these mutations was to map these mutants to chromosomal linkage groups and if possible narrow down the area within a chromosome closer to where the gene is located. Chromosomal mapping was performed for a few of these mutants and the results are summarized in (Table 3-2). Because of this initial mapping approach, we were able to map M-61(*od102*), J-72 (*od101*), P-94 (*od98*) and N-64 (*od97*) to chromosome IV and mutant V-128 to chromosome III. Further mapping was done with additional fluorescent reporters with the J-72 (*od101*) mutant for markers in the LG IV. With this approach we found that our J-72 (*od101*) mutation maps to the right arm of the chromosome and close to the center between 0.09 cM and 4.47 cM. (Table 3-6)

## New Alleles of *drp-1* gene

With the use of forward genetic screens, we can find new genes that participate in biological processes by screening for phenotypes of interest. In the case of our screen, we were able to find mutants that showed defects in mitochondrial dynamics and transport and therefore potential genes that participate in these pathways. As a "proof of concept," isolating known genes is indicative of the effectiveness of the screen. Because

we had mutants that were very similar in phenotype to known *drp-1* alleles, we performed complementation testing with said mutants and available alleles of *dpr-1*. We confirmed that a few of our strong elongation mutants are new alleles of *drp-1*. The mutants D-27, N-64 and P-94 have since been assigned the following allele names: *drp-1(od96), drp-1(od97),* and *drp-1(od98)* respectively.

Additionally, while conducting the complementation crosses, we also wanted to confirm the identity of these mutants and thus designed oligos to use for Sanger sequencing of the *drp-1* gene. Some areas of the gene were difficult to amplify but with different combinations of them we were able to amplify and send these DNA amplifications for sequencing. After analyzing the sequencing results we were able to pinpoint the polymorphisms present in each of these strains. (Figure 3-3) The following changes were found in these new alleles: the *drp-1(od96)* had a nonsense mutation R425Stop, the *drp-1(od97)* had a missense mutation G352R, and *drp-1(od98)* had a missense mutation D223N.

## V. Discussion

Gene discovery is considered an important tool for our understanding of biological phenomena, even now in the age of DNA sequencing. Because our model organism provides the ability to do gene discovery in the intact animal, we can carry out forward genetic screens and look for mutant phenotypes for specific biological processes. This chapter has described how we were able to carry out such a screen and what was done to understand what mutants were isolated.

Our screen was conducted as a forward clonal screen in order to find and recover any potential lethal or sterile mutants. We expected that some of the mutants with mitochondrial defects might be sterile or lethal because mitochondria conduct very important and essential processes, and thus introducing mutations that affect the

morphology and even their distribution within the cell could potentially cause lethal effects. We did not find any mutant phenotypes that were lethal and needed to be maintained as heterozygotes, but we assume this is because even though we screened close to 5,000 haploid genomes we have not saturated the screen. Our screen was conducted by sampling L4 animals, if there were to be any lethal mutants they could potentially not be making past the L1 stage. One of our mutants isolated, V-128 (*od105*), was found to be partially sterile but did not need to be maintained as a heterozygous or over a balancer. The sterility phenotype seems to linked to the phenotype but not as penetrant. We find that the screen might be close to saturation only because we seem to be isolating multiples alleles of *drp-1* gene.

The initial phenotypes we expected from carrying out this screen included: mitochondrial defects of fusion (small mitochondria in the VNC), mitochondrial defects in fission (large mitochondria in the VNC), defects in mitochondrial transport (reduction or lack of mitochondria in the VNC), or biogenesis or mitophagy defects (reduction or lack of mitochondria in the VNC or increase of mitochondria number in the VNC). During the first rounds of screening, we saw that a lot of the mutants isolated for mitochondrial fusion defects were false positives. If we were to focus on finding new genes in this category, we would need to design the screen differently and potentially carry out a modifier suppressor screen (e.g., a suppressor screen of *drp-1)* (*139*). With our current approach, we were not able to find mutants that had a defect in fusion but rather we were isolating plates that were showing this phenotype because of environmental stress rather than because of a mutation affecting mitochondrial fusion.

The mutants that we were able to isolate were ones with large mitochondria and with fewer mitochondria in the VNC. I believe these classes were easier to isolate because we were screening a population of worms on a drop of solution rather than individual animals on a pad. The latter would be a perfect scenario to find slight changes from wild

type but would make it incredibly laborious to screen. At this point there isn't a faster more efficient way to screen for these types of changes in the neuron in a high throughput manner.

Of the six mutants that we isolated and that showed elongated mitochondria, we now know that three of these are new alleles of *drp-1* gene: *drp-1(od96), drp-1(od97),* and *drp-1(od98).* The other three mutants, B-104A(*od99*), T-7 (*od104*), and T-17, we have yet to identify causative genes. These three show a phenotype that is milder than any of the new alleles of *drp-1,* which might mean that they play a secondary role in mitochondrial fission but not a primary role like the DRP-1 protein, which is recruited to the mitochondria to play a role in the membrane scission (*140*).

We were able to sequence and confirm the DNA changes of the three *drp-1* alleles that we isolated in our screen. The *drp-1(od96)* mutant is caused by a nonsense mutation that changes an Arginine (R) to a premature stop codon at position 425, which clearly can lead to the production of a truncated protein or the inability for the protein to be functional even if the protein is translated. The *drp-1(od97)* mutant is a missense mutation that causes an amino acid change of Glycine (G) to Arginine (R) at position 352. Finally, the *drp-1(od98)* mutant is caused by a missense mutation that causes a change of Aspartate (D) to Asparagine (N) at position 223.

Earlier this year, work was published on the structural basis of DRP-1 for receptor binding and constriction of the mitochondria (*34*). The work by Kalia et al. was able to look at the crystal structures of wild-type, full length human DRP1 protein binding to a mitochondrial receptor that recruits DRP1 and helps assemble it around the mitochondria for constriction. Because the human and worm DRP1 proteins are highly conserved, we can map out our new alleles and examine which domains are mutated. Our *drp-1(od98)* allele maps to the equivalent side chain that in the human form seems to be important for the interaction with receptor MID49 (*34*). Even though MID49 does

not have a clear orthologue in the worm, the functional importance of this residue suggests that this same domain might interact with other outer mitochondrial receptors for similar functions. The *drp-1(od97)* allele seems to be in the equivalent 1st Stalk domain. Kalia et al. indicate that the stalk is part of the loop that helps for both receptor binding and oligomer geometry (*34*). Again, in the case of the worm allele, the change from a neutral and small amino acid to a basic and large amino acid could be disrupting similar interactions, thereby demonstrating a functional, in vivo role for these residues.

The screen also resulted in mutants B-104A(*od99*), T-7 (*od104*), and T-17 that had elongated mitochondria but milder than what we see in *drp-1* mutants (Figure 3-1B). We have not mapped these mutants to either a linkage group or have any additional analysis at the moment. The mutant B-104A(*od99*) came out of the F1 plate B-104. The initial mutant showed two different phenotypes that proved to be unlinked after outcrossing to N2 wild type. We were able to isolate lines for each of those phenotypes. The mutant B-104A(*od99*) had the mild mitochondria elongation and B-104B(*od100*) has a neurite outgrown defect that was only seen because mitochondria were also present in the overgrown neurite process. We kept the B-104B(*od100*) for future analysis in our lab even though the neuronal mitochondria in this mutant appears wild type. In a very similar way, another mutant from the screen, O-101(*od103*), was also isolated because under closer observation and higher magnification, we were able to find that the mutant had ectopic expression of the mitochondrial reporter in the hypodermis. We suspect that O-101(*od103*) might be a mutation in a gene that epigenetically restricts neuronal expression, which would be of interest. We outcrossed this mutant to eliminate background mutations. We have added this mutant in our database for any future analysis in the lab.

As noted earlier, we were also able to isolate mutants with phenotypes related to defects of mitochondrial transport and that were isolated based on the decrease of

mitochondrial density in the VNC. The three mutants with decreased mitochondrial density are J-72 (*od101*), M-61(*od102*) and V-128(*od105*). For the J-72 (*od101*) mutant and V-128 (*od105*) mutant, other phenotypes were also linked to the mitochondrial phenotypes and were noted during the outcrossing to N2 wildtype strain. The J-72 (*od101*) mutant showed axonal guidance defects as well as severe uncoordinated and dumpy phenotypes. The axonal guidance defect was confirmed by using a cytosolic reporter expressed in only the interneurons P*glr-1*::mRFP (*odIs6*) (Figure 3-2B). This reporter labels the *glr-1* interneurons with a red marker that contrasts the green mitochondria. We see that a few of the neuronal processes that are normally present in the Ventral Nerve Cord bundle are being redirected to the lateral sides of the worm. Additionally, we quantified the number of axons that are misguided and found that anywhere between 1-4 axons are found outside of the VNC bundle, on both the anterior to posterior and posterior to anterior directions. (Figure 3-2E) Keeping this in mind, we believe that this could skew our mitochondrial density quantification slightly but a more thorough analysis needs to be done to confirm this.

The other two phenotypes present in J-72(*od101*), Unc and Dpy, were very useful for both the initial chromosomal mapping and for finding candidates based on phenotype. During the first genetic screens in *C. elegans* performed by Sydney Brenner, a lot of the visual phenotypes were exhausted and we know the genes that cause such mutations (*5*). Because of this, we have a list of genes that cause the uncoordination phenotype and with that we were able to narrow down to a list of candidates of Unc genes in chromosome IV. After crossing these genes to our mitochondrial reporter, we found that the *unc-44* and *unc-33* genes phenocopied J-72(*od101*) in the reduction of mitochondrial density, the axonal guidance defect, the uncoordination and the small body size. After complementation testing and sequencing

analysis, we confirmed that *unc-44* and not *unc-33* is the causative gene of J-72 (*od101*).

The *unc-44* gene is the ankyrin gene in *C. elegans.* The *unc-44* gene has been shown to be essential for correct outgrowth of axons (*141*). The abnormality seen in these mutants include the inability for chemosensory and mechanosensory neurons to reach their targets (*142*). The *unc-44* gene in *C. elegans* was also found to encode several ankyrin isoforms (*142*). Ankyrins are proteins that help with the interaction of membrane proteins and cytoskeleton, thus becoming important during at the neuronal growth cone. They include several transmembrane domains, Spectrin-Binding domains, and Akyrin Repeats (*142*). With this in mind, the fact that we see fewer mitochondria present in the axons might be because the connections made between the membrane and the cytoskeleton are either causing the transport defect by hindering the movement of mitochondrial motors. For this we would need to explore how other motors and cargo are distributed when our mutation is in the background.

The V-128(*od105*) mutant was also isolated because of mitochondrial transport defects, when outcrossing we were able to see that this mutant also had a partial sterility phenotype. Both of these phenotypes are linked. What we see in the adult worm is the lack of a noticeable gonad even at later stages of adulthood. The strain does not need to be kept as a heterozygote or over a balancer because it is not as penetrant and it does have plenty of adult animals that are able to reproduce and give off progeny for propagation. The mitochondrial phenotypes observed in the V-128(*od105*) mutant include a decrease in mitochondrial density, a gradient of density decrease from the anterior to posterior parts of the worm and larger sized mitochondria. All of these seem to be linked and remain after outcrossing to wild type N2.

Overall the screen produced nine mutants that had defects in either mitochondrial fission or defects in transport. We believe that the screen is not yet

saturated but is very close since we were able to isolate multiple new alleles of the *drp-1* gene. In the next chapter, I will discuss what strategies we implemented for mapping and ultimately cloning the mutants from this screen.

## VI. Figures and Tables

| Mutant Name | Phenotypes | Number of Outcrosses to N2 |
|---|---|---|
| D-27 | Strong elongated mitochondria | 2 |
| B-104A | Mild elongated mitochondria | 2 |
| B-104B | Neurite Outgrowth | 2 |
| J-72 | Fewer mitochondria, axonal guidance defect, Dpy, Unc | 5 |
| M-61 | Fewer mitochondria | 2 |
| N-64 | Strong elongated mitochondria | 4 |
| O-101 | Ectopic expression of mitochondrial reporter | 2 |
| P-94 | Strong elongated mitochondria | 2 |
| T-7 | Mild elongated mitochondria, smaller body size | 1 |
| T-17 | Mild elongated mitochondria | 0 |
| V-128 | Fewer mitochondria, partially sterile, density gradient along the VNC | 5 |

Table 3-1

| Mutant Name | Linkage Group I | Linkage Group II | Linkage Group III | Linkage Group IV | Linkage Group V | Linkage Group X |
|---|---|---|---|---|---|---|
| D-27 | No linkage analysis performed | | | | | |
| B-104A | No linkage analysis performed | | | | | |
| B-104B | No linkage analysis performed | | | | | |
| J-72 | Not linked | Not linked | Not linked | Linked | Not linked | Not linked |
| M-61 | Not linked | Not linked | Not linked | Linked | Not linked | Not linked |
| N-64 | Not linked | Not linked | Not linked | Linked | Not linked | Not linked |
| O-101 | No linkage analysis performed | | | | | |
| P-94 | No linkage analysis performed | | | | | |
| T-7 | No linkage analysis performed | | | | | |
| T-17 | No linkage analysis performed | | | | | |
| V-128 | Not linked | Not linked | Linked | Not linked | Not linked | Not linked |

Table 3-2

| Primer Name | Sequence (5'-3') |
|---|---|
| Outside Left | CAA ACA TCA TTT CGC AAC TGC CTC |
| Inside Left #0.5 | CTG ATC GTG TAA CTG GAG TG |
| Inside Left #1 | CGA CAA CAA ACT GAT CGT G |
| Inside Right #2 | GGA GTT CCA TTT CTG CTA G |
| Inside Left #3 | GAA ACA ACT GAG CTA TGC GGA G |
| Inside Left #1.5 | CGT TGA GAT GCG TTG AGC TG |
| Inside Right #1.5 | CAG CTC AAC GCA TCT CAA CG |
| Inside Right #3 | CGC TCT TTC TCC GGT TGA TG |
| Inside Left #2 | CAA CAA CAG CAG CAA TCC |
| Inside Right #1 | CGG CGT TGC CGA ATA ATC |
| Inside Right #0.5 | GCC ATG TCT TCA GTT TCA GC |
| Outside Right | CAG TGC TAT TGG CGC ATG TTG |
| 2nd Set Inside Left #1.5 | CCA TCG TTG AGA TGC GTT GAG CTG GTA C |
| 2nd Set Inside Right #1.5 | GTA CCA GCT CAA CGC ATC TCA ACG ATG G |
| 2nd Set Outside Left | CCAA ACA TCA TTT CGC AAC TGC CTC GTC |
| 2nd Set Outside Right | CCA GCA GTG CTA TTG GCG CAT GTT GAG |

Table 3-3

| Gene name | Transcript | Linkage Group | Known phenotypes | Available strains |
|---|---|---|---|---|
| unc-129 | C53D6.2 | IV | Axonal Guidance/outgrowth | NW987(ev554) |
| unc-17 | ZC416.8 | IV | small, Anxonal guidance | CB933 (e245); CB113 (e113) |
| unc-22 | ZK617.1 | IV | small, mitochondira muscle variant | BC177 (s17), BC18 (s13) |
| unc-24 | F57H12.2 | IV | NO Mito or Neuro Phenotype | CB138(e138), CB1172(e1172) |
| unc-26 | JC8.10 | IV | small | CB205(e205), CB1196(e1196) |
| unc-30 | B0564.10 | IV | small, axonal outgrowth variant | CB845(e191), CB318 (e318) |
| unc-31 | ZK897.1 | IV | NO Mito or Neuro Phenotype | CB169(e169), CB928(e928) |
| unc-33 | Y37E11C.1 | IV | dumpy, curly, axon trajectory and outgrowth variant | CB204(e204), CB572(e572) |
| unc-43 | K11E8.1 | IV | axon morphology variant, mitochondria morphology (muscle), small | MT2605 (n1186), MT1092 (n498) |
| unc-44 | B0350.2 | IV | dumpy, curly, dendrite development variant, axon guidance and outgrowth variant | CB362(e362), CB1197 (e1197) |
| unc-5 | B0273.4 | IV | axondendritic polarity variant, axon branching, outgrowth and guidance variant, | CB152 (e152), |
| unc-77 | WBGene00003557 | IV | mitochondria morphology variant (muscle), short | DR1089 (e625) |
| unc-8 | R13A1.4 | IV | ventral nerve cord abnormal, short | CB15 (e15) CB49 (e49) |
| unc-82 | WBGene00015212 | IV | mitochondria morphology variant (muscle) | CB1220 (e1220), VC2535 (gk1124) |

Table 3-4

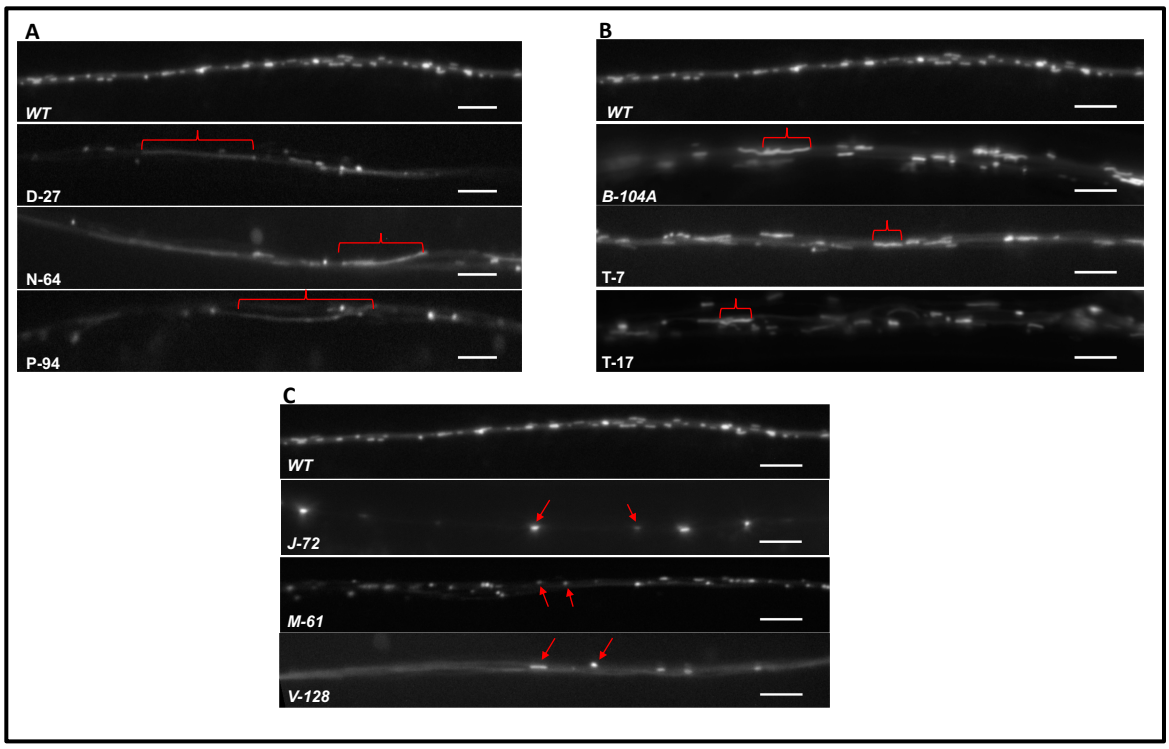


Figure 3-1

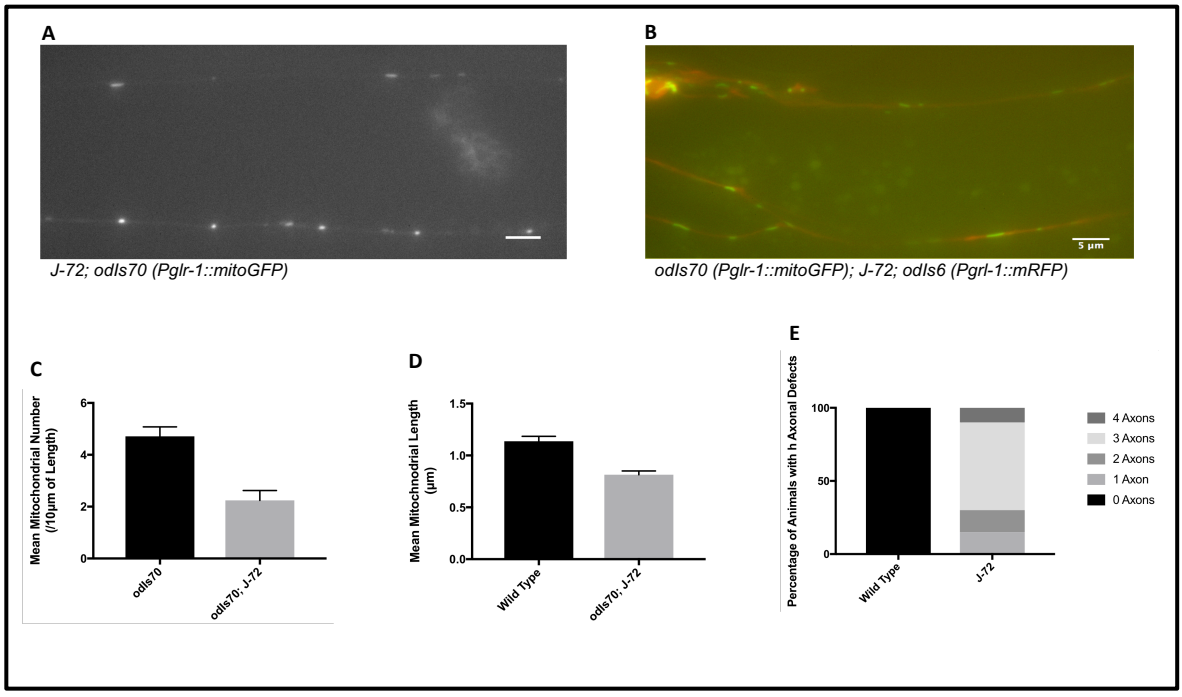


Figure 3-2

| Mutant Name | Rongo Lab Allele Designation |
|---|---|
| D-27 | od96 |
| B-104A | od99 |
| B-104B | od100 |
| J-72 | od101 |
| M-61 | od102 |
| N-64 | od97 |
| O-101 | od103 |
| P-94 | od98 |
| T-7 | od104 |
| T-17 | n/a |
| V-128 | od105 |

Table 3-5

| Crosses with Reporter | Genetic Map Position (cM) | F2 Non-Red Mutant | F2 Non-Red Wild Type | Percent Mutant/Total |
|---|---|---|---|---|
| EG7908; odIs70 | -22.29 | 2 | 86 | 2.3% |
| EG7911; odIs70 | 0.09 | 89 | 7 | 92.7% |
| EG7927; odIs70 | 4.47 | 30 | 18 | 62.5% |
| EG7934; odIs70 | 15.09 | 8 | 47 | 14.5% |

Table 3-6

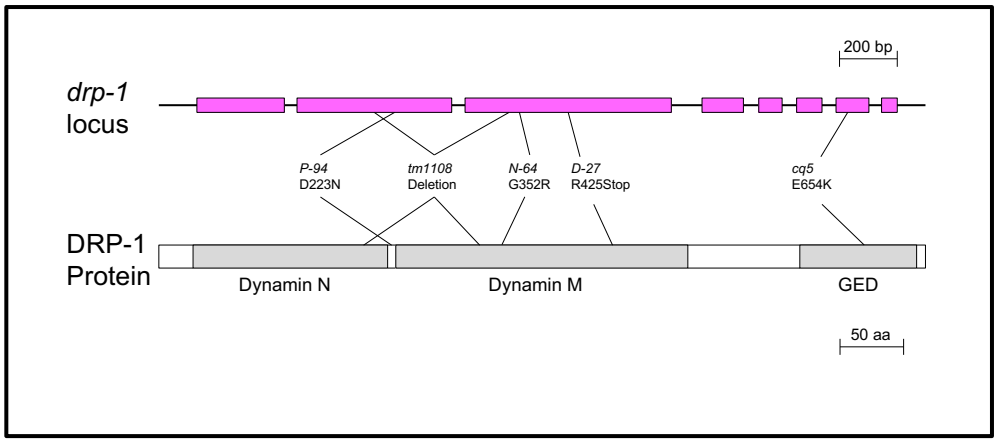


Figure 3-3

## VII. Figure legends

Table 3-1.

List of mutants that were isolated from the screen as well as their phenotypes and the times they have been outcrossed to wild-type N2.

Table 3-2

Chromosomal linkage mapping for the mutants isolated in the screen. We used the strains EG7835 I, EG7866 II, EG7898 III, EG7911 IV, EG7944 V, EG7943 V, EG7988 X that express the *Peft-3p::TdTomato::H2B::unc-54* reporter in the nuclei of the hypodermis. The mutants D-27, B-104A, B-104B, O-101, P-94, T-7 and T-17 were not mapped.

Table 3-3

Oligos used for the Sanger sequencing amplification of the *drp-1* gene in the mutants: D-27, P-94, N-64.

Table 3-4

Candidate UNC genes that are mapped to the Linkage Group IV and ones that had available known alleles. Some other known phenotypes were noted from each gene.

Figure 3-1

Mutants isolated from the forward genetic screen. (A) Mutants showing a strong elongation defect D-27, N-64, P-94. (B) Mutants showing a mild elongation defect B-

104A, T-7, and T-17. (C) Mutants showing a decrease in mitochondrial number, J-72, M-61, and V-128. Error bars are SEM.

Figure 3-2

Characteristics of the J-72 mutant. (A) J-72 mutant showing mitochondrial number decreased in the Ventral Nerve Cord as well as the axonal guidance defect out of the VNC bundle. (B) J-72 mutant with both the *Pglr-1::mito GFP (odIs70*) reporter as well as the *Pglr-1::mRFP(odIs6)* reporter showing that axons are indeed getting redirected out the VNC bundle. (C) Quantification of the Mitochondria Density for wild-type *odIs70* and the J-72 mutant. (D) Quantification for the Mitochondrial Size of the VNC for wild-type *odIs70* and the J-72 mutant. (E) Quantification of the numbers of axons getting redirected out of the cell body for 100 animals: 0, 1, 2, 3, or 4 axons. Numbers are either on the anterior part of the animal or both anterior and posterior.

Table 3-5

Rongo lab allele designations for the mutants from the screen.

Table 3-6

Mapping of the J-72 for reporters on either the right or left arm of the LGIV. Strains were crossed to the strains EG7908, EG7911, EG7927, EG7934 mapping to different genetic positions. Percentages were calculated to represent closer linkage to each marker.

Figure 3-3

Representative schematic of the new drp-1 alleles isolated in the screen and where their putative locations are with the protein domains.

# Chapter IV- Next Generation Sequencing Analysis of Mutants from Neuronal Forward Genetic Screen

## I. Abstract

Forward genetic screens have been a great tool for researchers who use *C. elegans* and other model organisms. Screens are designed to help in gene discovery and to go from mutant isolation to causative gene. Before the era of high-throughput DNA sequencing, identifying the causative gene was a very tedious process and required a lot of time. Now that we have the advantage and availability of high-throughput sequencing, we can use this tool to analyze forward genetic screens. In the following chapter, I will be describing how we have been able to use Next Generation Sequencing to analyze some of the mutants from our screen, with the hope that we can also use this approach to discovery the causative genes from all of our isolated mutants.

## II. Introduction

Our goal during the forward genetic screen was to isolate mutants that were defective in mitochondrial dynamics (fission/fusion) or mitochondrial transport. We were able to isolate 11 mutants overall: 6 mutants showed potential defects in mitochondrial fission (large mitochondria in the VNC), 3 mutants showed potential defects in mitochondrial transport (fewer mitochondria in the VNC), and 2 mutants isolated had non-mitochondrial phenotypes but had other phenotypes that made them of interest to our lab. As with any genetic screen, isolating mutants and outcrossing them to eliminate background mutations are only the first steps in understanding what genes are mutated to cause the mutant phenotype.

In the past, downstream analysis was time-consuming, especially when it came down to fine mapping the mutation. In the case of *C. elegans,* this is particularly the case because the genome is densely packed. The fact that our screen focuses on changes in the mitochondria, requiring screening for the phenotypes of interests under a higher

magnification microscope, adds to the time and labor needed for genetic mapping analysis. So far, we have been successful at the use of genetic markers and also transgenic markers for mapping and doing chromosomal linkage mapping as well as mapping to the right or left arm of the chromosomes for a few of our mutants.

With the advantage of Next Generation Sequencing becoming more available and new developing techniques, the *C. elegans* community has taken advantage of this approach to use Whole Genome Sequencing to map a causative mutation to smaller locations and clone the causative genes (*143-145*). Traditional mapping is still a useful tool to use in combination with NGS, because mutant strains can have multiple changes that cannot be ruled out with only using these new approaches. One of the major breakthroughs in *C. elegans* was the use of mapping-by-sequencing (*144*). In this approach, we use a strain, CB4846, a wild-type Hawaiian isolate known to have a variety of polymorphic loci, to probe at the genome-wide level and make use of the sequencing techniques to map the causative mutation.

Analysis of raw data from WGS can be the biggest challenge of this approach, especially for researchers who are not familiar with bioinformatic analysis. The Hobert lab, in addressing this concern, created a pipeline housed under the cloud-based Galaxy interface (*145, 146*). This mapping-by-sequencing pipeline is housed as CloudMap. It consists of tools that help the researcher take the raw data received, align it to a reference genome, process this data for variants, and filters those variants for ones that are present in the mutant strain. Cloudmap workflows work for both outcrossed and backcrossed strategies: Hawaiian Variant Mapping, EMS Density Mapping, and Variant Discovery Mapping. Hawaiian Variant mapping takes advantage of the Hawaiian polymorphic strain. In the EMS Density mapping, the mutant strain is not crossed to a polymorphic strain but rather this workflow will follow variants by using the EMS mutagenized strain variants versus variants in the starter strain. In the case of VDM, the

mutant strain is backcrossed to the starter strain and F2 homozygous are then pooled and bulked for sequencing to find *de novo* SNPs in the F2 recombinants not found in the reference genome (*147*). From all of these strategies, variants considered for analysis be given in both a tabular format and a graphical plot that delineates their locations (*147*).

Another pipeline workflow that is designed for analysis of *C. elegans* WGS data is called MiModD (*148*). This pipeline follows the example of CloudMap in that it can take the raw sequencing data and also provide the tools to make similar analysis including Variant Allele Frequency Mapping (VAF), Simple Variant Density Mapping (SVD), and Variant Allele Contrast Mapping (VAC). Both the VAF and VAC mapping strategies are used when analyzing non-isogenic segregant populations. With VAF specifically, you need to have variant information from the segregant population and at least one of the parental backgrounds used. In the case of our analysis, in *C. elegans,* we will be using the variants that are associated with the Hawaiian background, which is one of the parents used for mapping strategies of a few of our mutants. VAC is similar in that in needs additional information, but instead of the parental variant information, the analysis is performed with a second sample that has no variants that are used in the mapping. The last type of mapping analysis, SVD, is done when having nearly-isogenic populations. MiModD can also give a text report of the filtered variants in a tabular file as well as scatter plots for a visual identification of regions of linkage.

In this thesis, I used both of these pipelines, mainly because some of the CloudMap tools are not currently being updated or were not available at the time. We also installed a local version of MiModD and have a Galaxy interface that was installed via our Institute's server.

Our hopes were to use this approach and with the new bioinformatic tools available, to narrow down to a list of potential genes for each of our mutants that can be

used in future analysis. With such lists we can then pinpoint the causal mutation by using traditional techniques such as complementation crosses, phenocopy with available alleles, and performing rescue experiments to further confirm the gene.

## III. Materials and Methods

### Strains and reagents

Animals were grown at 20ºC on standard NGM plates seeded with OP50 *E. coli*. Some strains were provided by the *Caenorhabditis* Genetics Center. The following strains were used: *C. elegans* N2, *C. elegans* Hawaiian, *odIs70* (P*glr-1*:mitoGFP), B-104A, B-104B, J-72, M-61, N-64, T-7, T-17, O-101, V-128. For genomic DNA isolation we used: Qiagen's Gentra Puregene Core Kit A (4g) Cat #158667 and Thermo Scientific RNA Grade Glycogen Cat # R0551. For breaking up the worms during DNA isolation we used 0.5mm dia of Zirconia/Silica beads from BioSpec Cat #11079105Z.

### Hawaiian Mapping for Pooled Samples

Using published protocols and ones Hobert Lab's Protocols for Worm Genomic DNA Prep we adapted to our Hawaiian Mapping Approach (*149*). The mutants J-72 (*od101*), N-64(*od97*) and V-128(*od105*) were outcrossed to the Hawaiian Polymorphic Strain for analysis.

The N-64 (*od97*) and V-128 (*od105*) crosses started with male homozygous crossed into HA hermaphrodites. The F1 progeny were chosen via the *odIs70* marker to self-fertilize. 100 F2 progeny were then selected based on the *odIs70* marker and allowed to self-fertilize for 2-3 days. The F2 parents were then screened in a high magnification microscope using 5% agarose pads and 10nM Levamisole solution to anesthetize them. Any plates with F2 homozygous parents for the mutation were then allowed to propagate and the F3, F4, etc. progeny was allowed to starve for no more than one day for collection. As described in Doitsidou et al. 2010, 50 F2 plates were

needed, thus the vast amount of initial F2s set up for screening for homozygosity (*144*). Depending on time restrictions, multiple crosses were done to achieve the collection of the 50 F2 plates.

For the cross of J-72(*od101*) homozygous hermaphrodites were set up to be crossed to HA males. The non-unc progeny, considered the F1 generation, were selected for self-fertilization for a couple of days. Plates were scanned and selected F2 progeny that was Unc, Dpy and with the *odIs70* marker. These animals again were set up for self-fertilization and prepped for collection.

For collection of the F2 (containing the starved subsequent populations), collection was carried out on the day after plate starved. Since not all plates were ready for collection at the same time collections were done more than once, each time creating a new Eppendorf tube and storing at -80$^{o}$C until ready for genomic DNA prepping.

Using 5mL of M9 buffer we rinsed plates and collected into a 15mL Eppendorf tube using glass Pasteur pipettes to avoid loss of samples. After centrifuging for 2-3 minutes, worms were rinsed with 10mL fresh M9 and repeated washing 3 times. With the last wash, 15 mL of fresh M9 was added and then worms were incubated for 2 hours at 20$^{o}$C on a Nutator to get rid of food in the gut. After incubation M9 was added 5 more times for additional washes. After the last wash, tubes were centrifuged and M9 was carefully removed to not disturb the pellet of worms. Immediately, the worm sample was stored at -80$^{o}$C overnight or until ready for processing.

Collection of Non-Pooled Samples

Strains N2, *odIs70,* Hawaiian, B-104A, B-104B, M-61, T-7, T-17, and O-101 were collected without crossing to anything. Single animals were et up in 50 plates of OP50. Animals were left to propagate and similar to our other samples, plates were then collected the day after plate starved. The same protocol of 1) collection, 2) washing, 3)

incubation to remove gut bacteria and 4) subsequent washing was followed as with the prior strains. At the end of the final set of washes, worms were pelleted and M9 was removed as much as possible without disturbing the pellet. These pelleted worms were then stored at -80$^{o}$C overnight or until ready for processing.

## Genomic DNA Isolation

Following the Hobert Lab's Protocols for Worm Genomic DNA Prep and the protocol manual provided by the kit (*149*). Worm pellets were weighed of each sample (empty tube vs. tube with pellet). Using 9 of the 2mL Screw cap Microcentrifuge tubes beads were added to the 500uL mark. To the thawed worm pellet, 9mL of Cell Lysis Solution provided in the kit was added to break the pellet pipetting up and down was used. The solution of worms was then transferred to the next tube and so on until all pellets are in the same solution. 1mL of this cell lysis/worm mix was aliquoted into each labeled screw cap tube with beads. In the cold room, a bead beater was used to break up the worms. Pulsing 30 seconds and incubated on ice afterwards. At the bench 5 uL of Proteinase K (20mg/ml) were added to each tube and incubated in a 55$^{o}$C bath overnight vortexing the tubes every hour until leaving for the night.

On the next day, all supernatants were collected in 15 mL tubes making sure not to transfer beads. Samples were cooled to room temperature. After cooling down, 45uL RNase A were added and incubated at 37$^{o}$C on a nutator for 1 hour. Samples were then cooled on ice for 3 min. 3mL of protein Precipitation Solution was added and incubated on ice for 5 min. Samples were vortexed vigorously for 20 seconds at high speed and cooled 5 min. on ice. Then, samples were centrifuged at 4$^{o}$C and 4,000rpm for 15 min. (~2,000xg). The supernatant was then transferred to a clean tube without touching the white pellet.

To these new tubes, 9mL of Isopropanol were added and mixed by inverting 50 times. Following, 15uL of glycogen were added and incubated at -20°C for 1 hour. After incubation, samples were centrifuged for 3 min at 4,000rpm and supernatant was carefully discarded. For many samples a pellet is not visible so further work assumes there is a pellet. 3mL of 70% Ethanol were then added and invert several times to wash DNA pellet. Tubes were centrifuged for 3 min. at 4000rpm. Supernatant was removed and “pellet” allowed to air dry for 5 min. 450uL of DNA Hydrating Solution was then and pipetted up and down. This solution was then transferred to a new microcentrifuge tube and incubated at 65°C dry bath for 30 min. to dissolve DNA.

Afterwards, all samples were taken to measure DNA concentration (A260/A280). Using 10ng/ul of each sample in a 1% TAE gel and ran for 40 min at 100V to check for protein and RNA.

## Illumina sequencing

The RUCDR Infinite Biologics located in Rutgers University were contracted for library construction and sequencing. We provided 1ug of genomic DNA. We submitted 50uL of gDNA at 100ng/ul. Sequencing was done using the Illumina platform.

## Cloudmap Analysis

To gain access to the Cloudmap workflows: http:://usegalaxy.org/cloudmap. Using the *Shared Data* link, the *Data Libraries* were used to search for the CloudMap data library (*145*). The files used were: WS22-.64_chr.fa as well as the data files of the Hawaiian SNPs (to the reference genome) HA_SNPS_Filtered__1033346Varinats_WS220.vcf and HA_SNPS_Unfiltered__112061Varinats_WS220.64.vcf.

Using the FTP client Filezilla, upload the raw data that received from RUCDR. Quality control checks were ran using *FASTQC* on the raw sequence files. To change the file

type from “fastq” to “fastqsanger” *FASTQ Groomer* tool was then used. After these pre-analysis steps, all files are uploaded to the working history.

The *CloudMap Hawaiian Variant Mapping with WGS and Variant Calling workflow* was downloaded y searching in the Published Workflows tab. On the run page, all appropriate inputs were selected for each data set before selecting “Run Workflow” After the entire workflow is completed, files of interest given as a result. For the step “CloudMap: Hawaiian Variant Mapping with WGS…” the output PDF file containing the graphical output for this workflow can be downloaded. For the step “Homozygous variants annotated (snpEff)…” a tabular file of the variants associated with this mutant can be downloaded.

With the use of MS Excel or similar software, data from the tabular file can be filtered and sorted for variants mapped to linked chromosomes and within regions pinpointed by the graphical output. The narrowed-down list can be even further filtered by the type of DNA changes/effects that are putative changes for defects in protein translation and function such as. Some of these are: Stop gained, non-synonymous change, frame shift, Splice Site Donor etc.

MiModD Analysis

For installation instructions as well as the tutorials access: https://mimodd.readthedocs.io/en/latest/index.html. As a learning step, tutorials can be downloaded and analyzed using the Galaxy instance accessible to our institute. To do mapping-by-sequencing analysis the CloudMap paper data tutorial is the most beneficial to follow. For our sample analysis, the same *C. elegans* genome reference sequence file (in fasta format), a BAM file of NGS reads from an N2 laboratory sample (Illumina HiSeq 2000 paired-end sequenced), and a Hawaiian strain SNV file (in vcf format with

coordinates to reference genome version) from the tutorial are kept in each working history.

Raw data was uploaded using the FTP client Filezilla under a new history. Taking the raw fastq files, convert to usable BAM formats. Metadata was then added to the N2 proof of concept file using the tool *MiModD Reheader* with a unique read-group ID as well as a sample name. For example, for the N2 file: “Read-group ID: 001, Sample name: N2, Description: wt control”. For the raw data from RUCDR and using tool *MiModD Run Annotation*, metadata was created as a SAM format. For example, for mutant J72 the following information: “Read-group ID: 002, Sample name: J72, Description: J72 mutant”. Using the tool *MiModD Convert* files from a fastq paired-end are converted to  a BAM file using the previously appointed header.

Using the tool *MiModD Read Alignment* map the sequence reads to a reference genome using SNAP (Galaxy Version 0.1.8_0). Next, using the tool *MiModD Variant Calling* generate a BCF file of position-specific variant likelihoods and coverage information based on a reference sequence and reads aligned against it. Following this step, the tool *MiModD Extract Variants* to get the variants from the file previously created and in the case of J72 the additional VCF file option was selected with the Hawaiian SNPs file. For all of our other mutants this option is not necessary.

In order to extract variants that are associated with our only our mutant the tool *MiModD VCF Filter* can be used. Sample specific filters that would pinpoint homozygous variants found in the mutant and not in the N2 file can use these parameters: “Sample: J72, Genotype pattern: 1/1, and Depth of coverage: 3 and Sample: N2, Genotype pattern: 0/0 and Depth of Coverage: 3”. This same type of filtering can be done with the analysis in the other mutants, including ones that are aligned with multiple samples such as odI70.

For Hawaiian mapping, the tool *MiModD NacreousMap* with the option for Variant Allele Frequency Mapping was used using the VCF file of variants generated in the previous

steps and “external_source_1” as the unrelated parent sample. Same steps were then applied for the N2 sample, using the *MiModD VCF Filter* with *N2* only using “Sample: N2, Genotype pattern: 1/1 and Depth of Coverage: 3” to check for zero variants. After this, the tool *MiModD NacreousMap* was used with the VAF type option and VCF of Variants extracted and the input “Sample: J72, the Related Parent: N2, and the Unrelated pared: “external_source_1”. At that point, there is no need to generate graphs but to give Tabular per-variant report instead. This step in the analysis gives a text report showing the “bins” data for all of the chromosomes including the MtDNA and linkage data. The higher linkage value means the higher chance of mutation residing in that bin. Again, using the tool *MiModD NacreousMap* and the VAF mapping option, use the per-variant report file to get both scatter plots and histograms. With the information of these graphs, geographic linkage can be narrowed down to cM. Using *MiModD VCF Filter* extract from the VCF Filtered data using a region filter. In the case of J72, the VCF filter of J72 variants as input was used and the added region information was “Chromosome: chrIV, Region Start: 5000000, Region End: 70000000”.

To annotate these results, the tool *List Installed SnpEff Genomes* was first used. Then, the tool *MiModD Variant Annotation* with the input of the VCF file from the last filter and selection of SpnEff Genome “Caenorhabditis_elegans: WBcel235.86” was carried out. The final tool, *MiModD Report Variants* can be used to give a human-friendly format using the VCF input with the variants annotated from the previous step and an output in either HTML format or Tab-separated file.

Mutants that were not crossed into the Hawaiian Polymorphic strain for mapping were analyzed alongside with the starter strain *odIs70* as well as our own lab’s wild type N2 sequenced files. Follow a similar tool selection with minor changes. At the step of the variant calling, the variant extraction is performed without using any pre-calculate VCF file (like the HA SNPs). When filtering variants, employ filters such as: “Sample: M61,

Genotype pattern: 1/1, Depth of coverage: 3; Sample: N2, Genotype pattern: 0/0, Depth of coverage: 3; Sample: CGCN2, Genotype pattern: 0/0, Depth of coverage: 3; Sample: *odIs70*, Genotype pattern: 0/0, Depth of coverage: 3". When using the tool *MiModD NacreousMap,* select the Simple Variant Density mapping option. The downstream tools are similar to the analysis of the other described mutants.

## IV. Results

We were able to use Next Generation Sequencing to facilitate mapping the mutants that we isolated from the screen. We had two different mapping-by-sequencing strategies that we wanted to employ and that have been used in the mapping of genes in *C. elegans* WGS. In the previous chapter, I described how we took the majority of our mutants and outcrossed to the N2 wildtype strain to eliminate background mutations caused by the EMS mutagenesis. I also described how we used transgenic marker strains to do chromosomal linkage mapping. After working with the mutants for some of these crosses and becoming more familiar with their phenotypes, a few of these became of more interest to us: J-72(*od101*), N-64(*od97*) and V-128(*od105*) mutants. Because of our interest in mapping these genes we wanted to use the Hawaiian Polymorphic strain to cross and get recombinants to use this type of mapping-by-sequencing approach. For the rest of our mutants our strategy was use the outcrossed strains for preparation to do WGS.

### Genomic DNA Isolation

Fortunately, using both published data and protocols from the Hobert lab that were available on their lab's website we were able to adapt their protocol for our mutants during the worm genomic DNA preparation (*144, 149, 150*). Following the adapted protocol our genomic DNA concentrations ranged from 250-1,400ng/ul. Even though we

use a commercially available kit for gDNA extraction, we were able to adjust a few of the steps to help our needs. For example, changing to an overnight incubation at the step where Proteinase K is added gave us maximum yield as well as making sure all our animals were thoroughly broken up using the Bead Beater. Overall, we had more than enough genomic DNA isolated from our mutants and controls to give to the sequencing facility. Our DNA was also of high quality with no protein or RNA contaminants. After receiving our samples, the RUCDR facility used a Bioanalyzer to check the PCRfree DNA libraries they generated with our gDNA. The results of this test showed that the libraries were of good quality and that the size fragments are 470bp.

## WGS Sequencing Results

We received the sequencing raw data from RUCDR and we stored both local and server copies due to the size of all of the combined files. We then uploaded the sequencing files for the J-72 (*od101*), N-64 (*od97*) and V-128 (*od105*) mutants to use the CloudMap pipeline for analysis. The following is a description of each mutant analysis.

We analyzed the raw data for N-64 (*od97*) mutant and were able to generate a narrow list of variant sites that are linked to the chromosomal region that is pinpointed in the variant plots as well as the region that matched our chromosomal linkage mapping analysis. (Figure 4-1) We filtered variants in the Linkage Group IV region Between 4Mb and 7Mb. We found that five variants in this region have changes that can have a significant effect on gene function (Table 4-2). Our reasoning for analyzing this elongated mitochondrial mutant was that, despite its close linkage to *drp-1*, we had not found a variant in the *drp-1* gene via Sanger Sequencing. At the time we were preparing our mutants for gDNA isolation, we decided to also prepare this mutant to send it for WGS as well. Our WGS analysis shows that the *drp-1* gene is on the candidate gene list as having a Non-Synonymous Change that causes a G (GGA) to R (AGA) at position

352 change in the protein, despite missing this change in our original Sanger Sequencing Analysis. We decided to do complementation crosses with both available alleles of *drp-1* and found that our mutant N-64 (*od97*) failed to complement both alleles. With this information, we believe that this mutant is another one of the new alleles of *drp-1* that we were able to isolate from our screen. This N-64 mutant is now *drp-1* (*od97*) in our records.

Our next mutant that we analyzed was the J-72 (*od101*) mutant. Again, similar to our last analysis, we narrowed down to a list of variant sites that were in the region that was noted in the variant plots. (Figure 4-2) Our candidate list from this region is listed in (Table 4-2). These genes were the ones that showed DNA changes that would most obviously impact gene function. In this list, we see that the *unc-44* gene is present. From our own candidate gene screen approach of Unc genes, as well as complementation tests, we know that *unc-44* is a candidate gene that can affect mitochondrial density along dendrites. With this analysis, we now know the DNA change that is present in our mutant. In mutant J-72 (*od101*), we see an early Stop Codon created by the change Q (CAA) to Stop (TAA) at position 2152.

The next mutant we analyzed was the V-128 mutant. Our chromosomal linkage mapping results linked this mutation to chromosome III of the genome. When we analyzed the WGS data and the variant plots, we saw that indeed this mutation was linked to LGIII and that the area of linkage lies between 5Mb and 10Mb in that chromosome (Figure 4-3). The list of variants in this region was longer than what we saw in the previous analysis (Table 4-4). We ordered available alleles for the ones available through the *Caenorhabditis* Genetics Center. With the alleles for some of these candidates we performed crosses to our mitochondrial reporter to find a phenocopy of our V-128 mutant. After a few crosses we found that the *mtx-2* gene gave a phenocopy

to V-128. We then performed a complementation test and found that *mtx-2* fails to complement V-128 (Data not shown).

The mutants M-61, B-104A, T-7 and T-17 were analyzed using the MiModD pipeline. Because these were not crossed to the Hawaiian polymorphic strain, we opted to do their individual bioinformatic analysis alongside the our lab's N2 strain and the *odIs70* strain that were also sequenced. Again, some of these were backcrossed to the N2 wildtype strain but only a few times so our options are to use the Simple Variant Density Mapping. This mapping gives a different graphical output than what had for the previous mutants (Figure 4-5, 4-6, 4-7) In the case of M-61, we can use the graph and the information from the chromosomal linkage group mapping to narrow down the variants that may be potential candidates. For the remaining mutants: B-104A, T-7 and T-17 we cannot do this filtering because we haven't done chromosomal linkage mapping.

## V. Discussion

Gene discovery in *C. elegans* and other model organisms has improved by the use of Next-Generation sequencing approaches. We were able to implement WGS to help us map some of our mutants from our forward genetic screen. We adapted some protocols geared towards isolating genomic DNA for both pooled and non-pooled worm samples and were successful in doing so.

Overall, the protocols we adapted led us to have good quality genomic DNA as well as good concentrations to have enough material to the sequencing facility.

For the analysis of the raw WGS data received from RUCDR of our mutants, the N2 strain, the *odIs70* starter strain, and the Hawaiian strain, we employed the CloudMap pipeline for the bioinformatic analysis. This was designed to help researchers like me with little to no experience in bioinformatics and because it does the analysis in the Galaxy Platform. (*145*) At the time of our analysis, we used "workflow" tools that were

found under shared libraries, but these hadn't been updated or maintained for several years. We used it to analyze the published data and we were successful in mapping the gene from the publication. With this experience, we then took the data from the three strains, N-64 (*od97*), J-72 (*od101*) and V-128 (*od105*), that were crossed to the Hawaiian polymorphic strain and analyzed it using the workflow for "Hawaiian Variant Mapping with WGS Data and Variant Calling". For each of these three strains, the workflow gave us graphical variant plots as well as tabular files of the variants. The list of candidates for each of these (Table 4-1, 4-2, 4-3), ranged from 5-14 genes. This range of candidates was a much easier number to investigate and validate downstream and gave us confidence that the sequencing was of good quality.

In the case of mutant N-64, one of our strong elongated mitochondrial mutants and the only one of such that we were not able to confirm a change in the *drp-1* gene via Sanger sequencing, we were able to narrow the gene identity down to 5 candidates, one of which was *drp-1.* With further complementation testing, we confirmed that it was a new allele of *drp-1.* It is currently unclear why this change was not detected using our Sanger sequencing strategy. Nevertheless, with the confirmation that N-64 is a new allele, we named it *drp-1(od97)* for our records.

In the case of the J-72 (*od101*) mutant, which shows fewer mitochondria in the ventral nerve cord, axonal guidance defects, and an uncoordinated and dumpy phenotype, we narrowed down to 8 candidates and in that list we identified the *unc-44* gene. From the previous chapter, we had both the *unc-44* and the *unc-33* genes as potential candidates. Complementation testing suggested that the identity of J-72 (*od101*) was likely to be *unc-44,* and our WGS analysis supported this. After this analysis, we attempted to confirm this further by doing rescue experiments using combinations of genomic fosmids that contained the wild-type *unc-44* gene; however, all of the combinations of these were toxic and no animals resulted from the injections.

Because *unc-44* is a novel gene in the mitochondrial dynamics and/or transport field, we will need to make sure to confirm via an alternative rescue approach. The J-72 (*od101*) mutation is a nonsense mutation at Q2052, and the *unc-44* gene is over 30 kb and expressed through at least nine different isoforms. As an alternative approach to confirm the identify of J-72 (*od101*), we can use CRISPR gene editing to manipulate our mutant strain by reverting the nonsense mutations and manipulate a wild-type strain by introducing the J-72 (*od101*) change to rescue and phenocopy, respectively.

Finally, for the V-128 (*od105*) mutant, which also has fewer mitochondria along the axons, we narrowed down to a list of 14 genes. This list, although bigger than that of the last mutants analyzed, provided a more manageable amount to use for downstream analysis. We did a search and found that many of these had alleles that were available for order from the CGC. When we received these mutants and crossed them to our mitochondrial marker, we found that the deletion allele *mtx-2(gk444)* appeared to phenocopy V-128 (*od105*). Our next step was to perform a complementation test with *mtx-2(gk444)* and we were able to see that our mutant failed to complement the phenotype. The *mtx-2* gene is the orthologue for human Metaxin-2, which is a mitochondrial import protein, potentially connecting the mitochondrial import machinery and mitochondrial transport. We hypothesize that the Metaxin component of the import machinery plays an additional role of interacting with mitochondrial motors and their adaptors. The V-128 (the *mtx-2* allele) is a missense mutation G205R and the gene is small enough that we can use a transgenic rescue to confirm its identity.

As far as the pipeline itself, CloudMap was relatively easy to use but since their tools haven't been updated and even their tools input and names have slightly changed it took a lot of trial and error to make sure we were doing the correct preparation of data and the analysis steps themselves. We were able to reach Galaxy Application Support who helped us understand some of the bugs and error codes we would get with some of

these. After the analysis of the three mutants described earlier, we wanted to use this to continue analyzing the mutants that were not crossed to the HA strain for mapping but their tools would not work anymore. Ultimately, we reached out to the Hobert lab for further help before continuing use of it and were directed to use the MiModD pipeline instead. Transitioning pipelines took some time, because even in the initial stages as we attempted to download and set up our MiModD Galaxy instance we would get too many errors. Finally, with help from the IT department at our institute, we were able to obtain permanent access to a Galaxy instance at our institute's server for use of MiModD.

With the new MiModD pipeline we were able to analyze the data for the remainder list of mutants from our screen: B-104A, M-61, T-7, T-17. For one of them, we were able to narrow down to a list of candidates based on the chromosomal linkage mapping previously done. This list provides a smaller number of genes to work with in future analysis. For the remainder of the mutants, we will need to do some chromosomal mapping in order to narrow down to a smaller list of genes.

Ultimately, our focus for the future will be to take one or two of the genes isolated from this screen to confirm via rescue and then proceed to do further analysis. For example, in order to understand the molecular mechanism of either UNC-44 and/or MTX-2, we will need to address some basic questions, including whether these genes act cell autonomously, where in the cell are their protein products localized, and do they interact genetically with other known mutations that affect mitochondrial dynamics and/or transport.

# VI. Figures and Tables

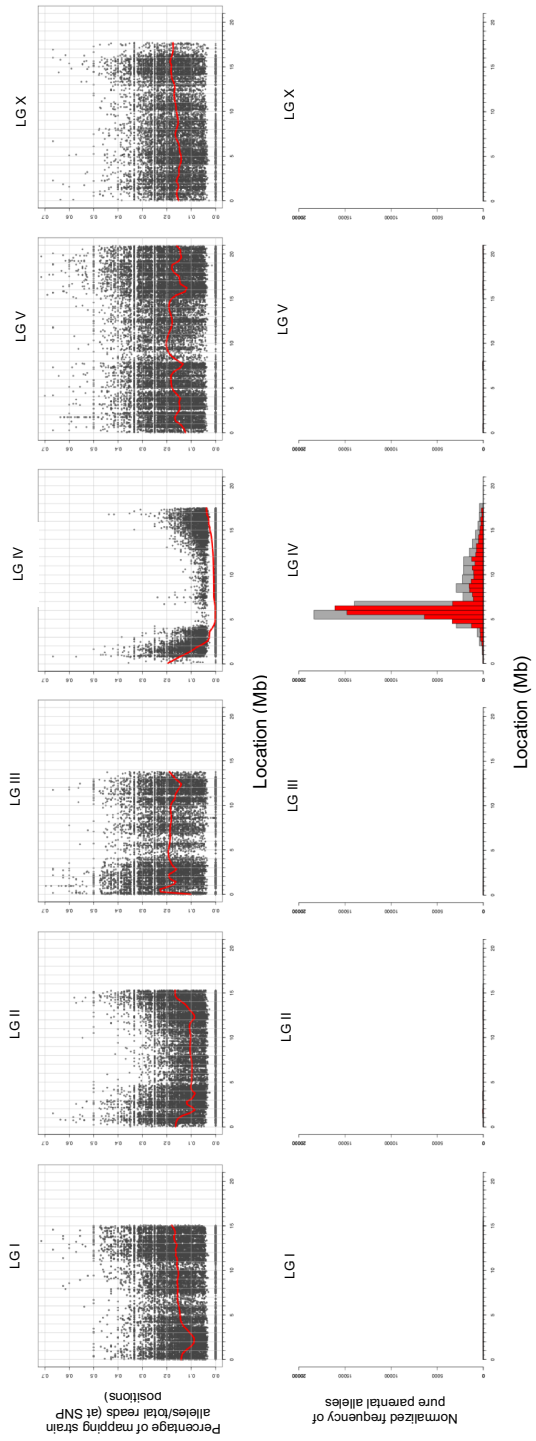


Figure 4.1

| Transcript | Gene | Type of DNA change |
|---|---|---|
| F36A4.7 | ama-1 | Non-Synonymous |
| F15E6.1 | set-9 | Non-Synonymous |
| W03F8.2 | W03F8.2 | Non-Synonymous |
| ZK616.8 | ZK616.8 | Frame Shift |
| T12E12.4 | drp-1 | Non-Synonymous |

Table 4-1

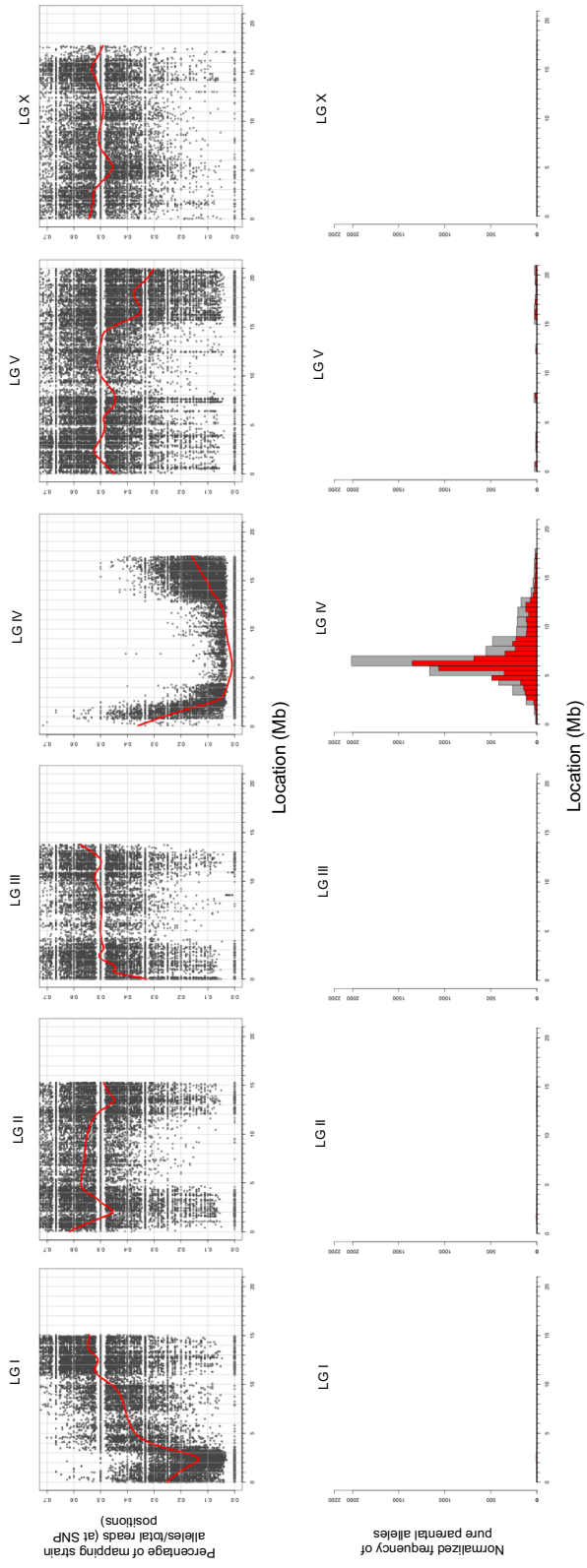
LG I
LG II
LG III
LG IV
LG V
LG X
Location (Mb)
Percentage of mapping strain alleles/total reads (at SNP positions)
Normalized frequency of pure parental alleles

Figure 4-2

| Gene Name | Effect |
|---|---|
| F41H10.3 | Non-Synonymous Change |
| ZK616.8 | Frame Shift |
| unc-44 | Stop Gained |
| sqd-1 | Non-Synonymous Change |
| pgl-1 | Non-Synonymous Change |
| nhr-105 | Non-Synonymous Change |
| tag-80 | Non-Synonymous Change |
| C50F7.5 | Stop Gained |

Table 4-2

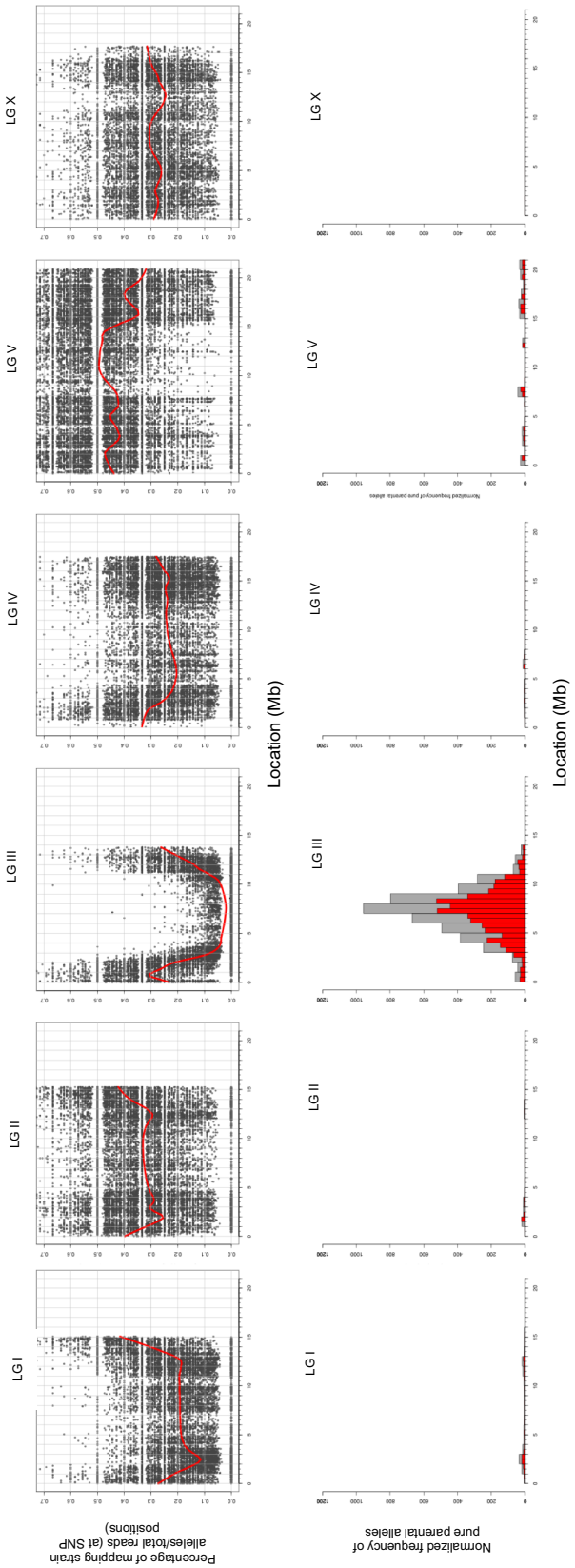
LG I
LG II
LG III
LG IV
LG V
LG X
Location (Mb)
Percentage of mapping strain alleles/total reads (at SNP positions)
Normalized frequency of pure parental alleles

Figure 4-3

| Gene Name | Effect |
|---|---|
| larp-1 | Frame Shift |
| F54D8.6 | Frame Shift |
| ced-6 | Frame Shift |
| psf-1 | Non-Synonymous Change |
| prk-1 | Splice Site Donor |
| ZK418.6 | Frame Shift |
| exos-9 | Non-Synonymous Change |
| R151.2 | Non-Synonymous Change |
| T04A6.4 | Frame Shift |
| flt-1/baz-2 | Non-Synonymous Change |
| mtx-2 | Non-Synonymous Change |
| flp-23 | Frame Shift |
| B0303.7 | Non-Synonymous Change |
| ZK507.1 | Non-Synonymous Change |

Table 4-3

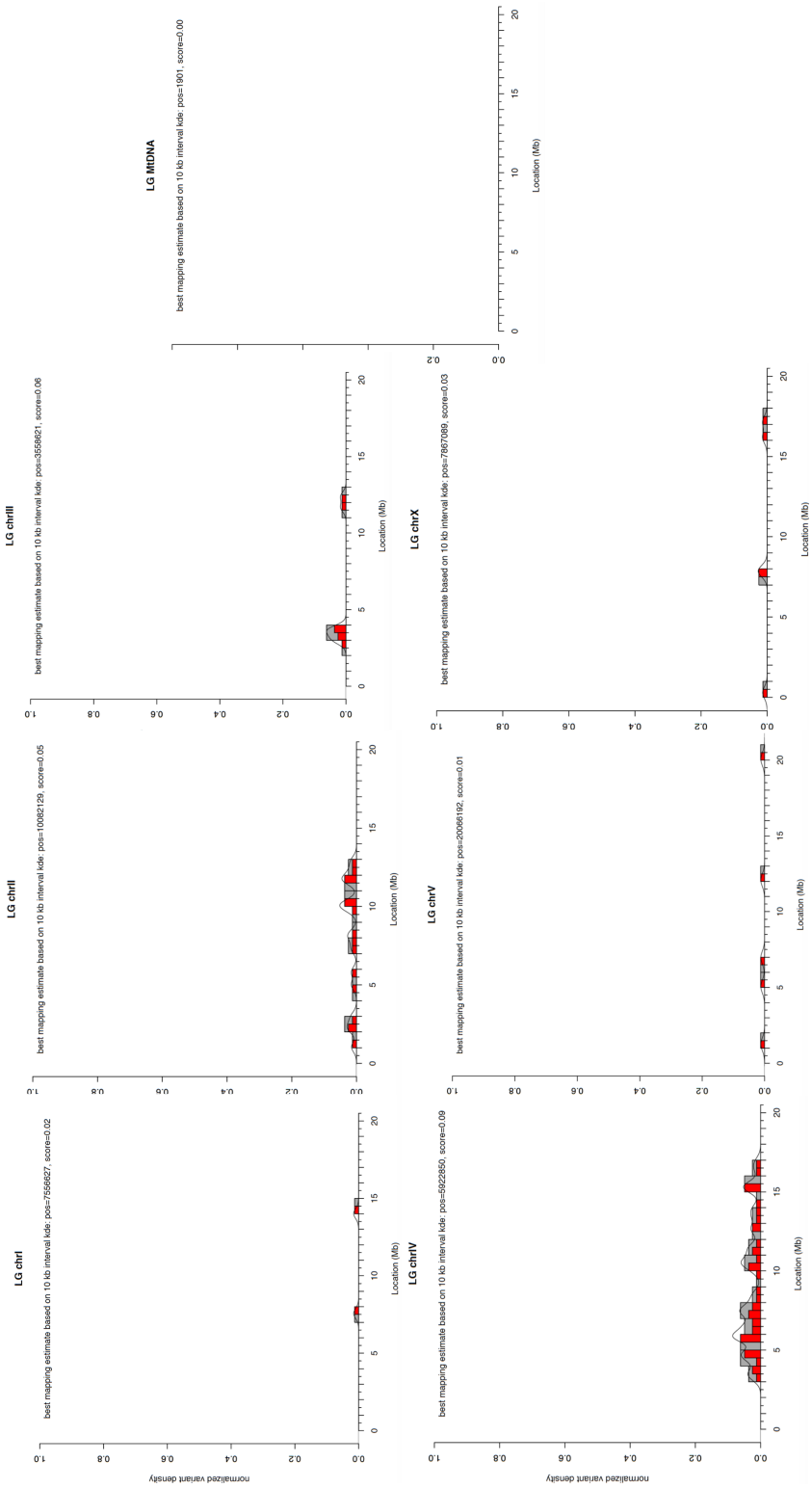
LG MtDNA
best mapping estimate based on 10 kb interval kde: pos=1901, score=0.00
LG chrIII
best mapping estimate based on 10 kb interval kde: pos=3558621, score=0.06
LG chrX
best mapping estimate based on 10 kb interval kde: pos=7867089, score=0.03
LG chrII
best mapping estimate based on 10 kb interval kde: pos=10082129, score=0.05
LG chrV
best mapping estimate based on 10 kb interval kde: pos=20066192, score=0.01
LG chrI
best mapping estimate based on 10 kb interval kde: pos=7556827, score=0.02
LG chrIV
best mapping estimate based on 10 kb interval kde: pos=5922650, score=0.09
Location (Mb)
normalized variant density

Figure 4-4

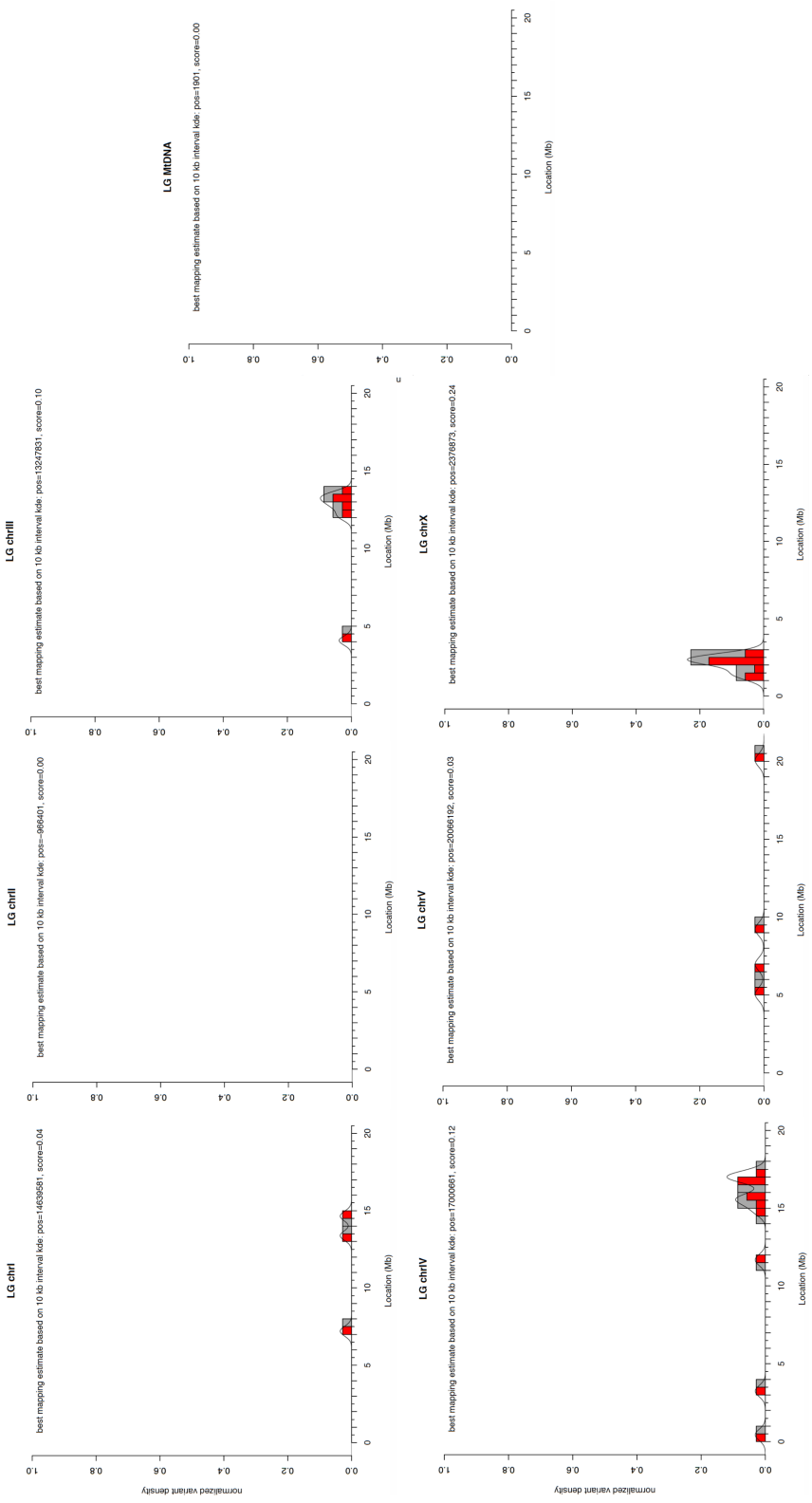
LG chrI
best mapping estimate based on 10 kb interval kde: pos=14630561, score=0.04
LG chrII
best mapping estimate based on 10 kb interval kde: pos=-9668401, score=0.00
LG chrIII
best mapping estimate based on 10 kb interval kde: pos=13247831, score=0.10
LG chrIV
best mapping estimate based on 10 kb interval kde: pos=17000661, score=0.12
LG chrV
best mapping estimate based on 10 kb interval kde: pos=20066192, score=0.03
LG chrX
best mapping estimate based on 10 kb interval kde: pos=2378873, score=0.24
LG MtDNA
best mapping estimate based on 10 kb interval kde: pos=1901, score=0.00
normalized variant density
Location (Mb)

Figure 4-5

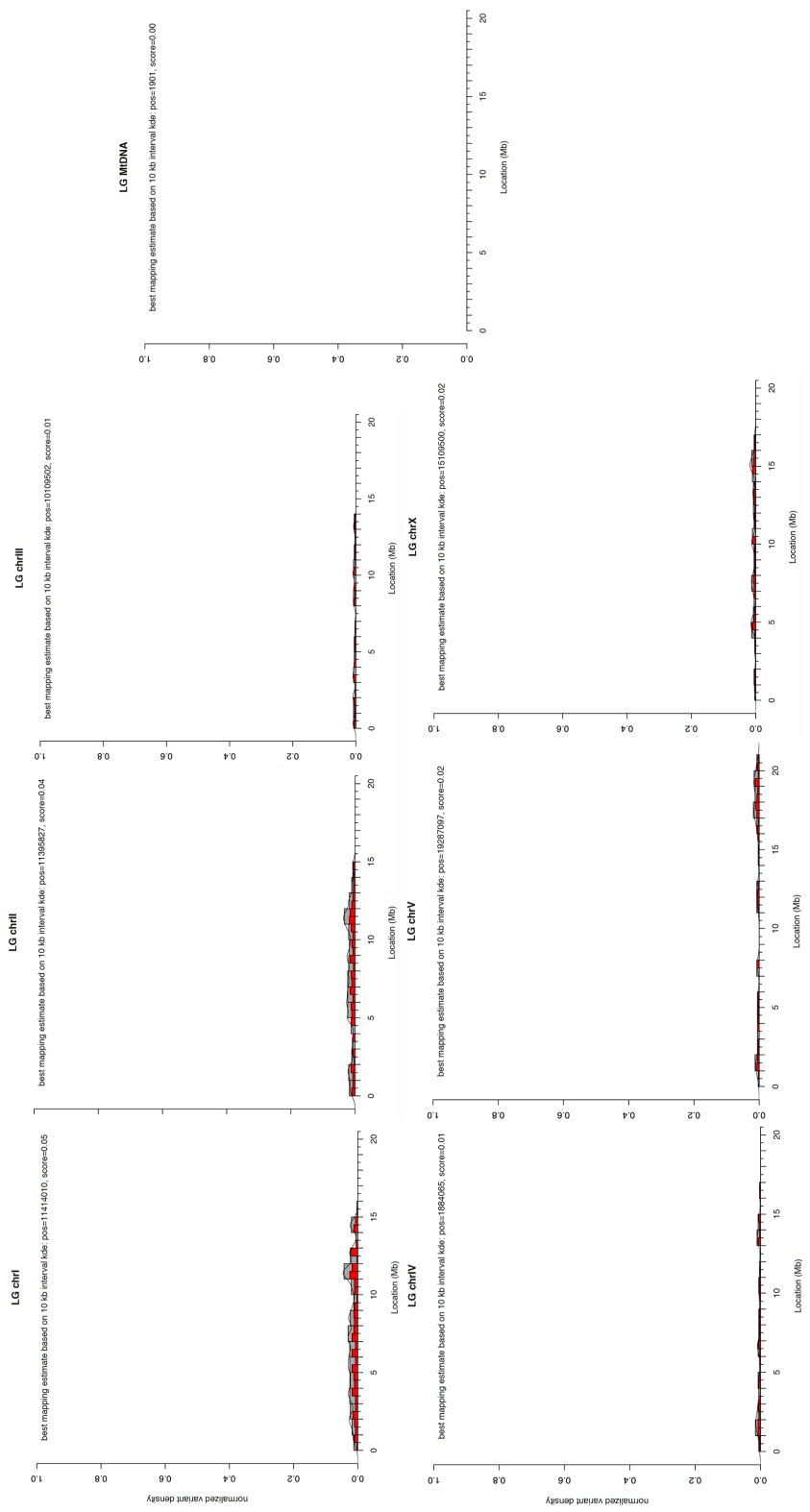
LG MtDNA
best mapping estimate based on 10 kb interval kde: pos=1901, score=0.00
LG chrI
best mapping estimate based on 10 kb interval kde: pos=11414010, score=0.05
LG chrII
best mapping estimate based on 10 kb interval kde: pos=11395827, score=0.04
LG chrIII
best mapping estimate based on 10 kb interval kde: pos=10109502, score=0.01
LG chrIV
best mapping estimate based on 10 kb interval kde: pos=16864065, score=0.01
LG chrV
best mapping estimate based on 10 kb interval kde: pos=19287097, score=0.02
LG chrX
best mapping estimate based on 10 kb interval kde: pos=15109500, score=0.02
normalized variant density
Location (Mb)

Figure 4-6

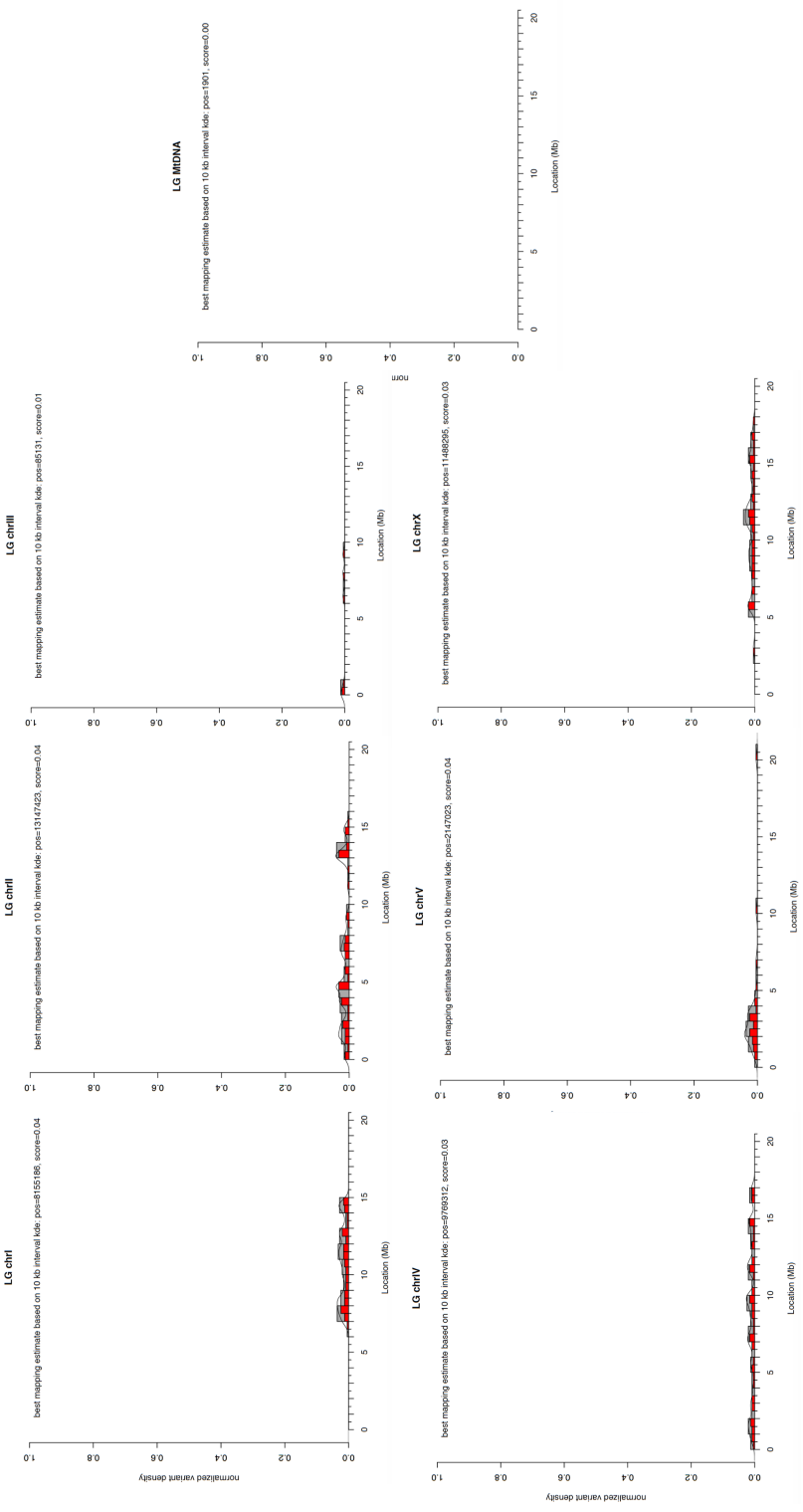
LG MtDNA
best mapping estimate based on 10 kb interval kde: pos=1901, score=0.00
LG chrIII
best mapping estimate based on 10 kb interval kde: pos=85131, score=0.01
LG chrX
best mapping estimate based on 10 kb interval kde: pos=11488295, score=0.03
LG chrII
best mapping estimate based on 10 kb interval kde: pos=13147423, score=0.04
LG chrV
best mapping estimate based on 10 kb interval kde: pos=21477023, score=0.04
LG chrI
best mapping estimate based on 10 kb interval kde: pos=8155186, score=0.04
LG chrIV
best mapping estimate based on 10 kb interval kde: pos=9789312, score=0.03
Location (Mb)
normalized variant density

Figure 4-7

## VII. Figure Legends and Table Legends

Figure 4-1

Graphical analysis of the N-64 mutant using Hawaiian Variant Mapping using the CloudMap Pipeline. Scattered plots and Frequency Allele plots are shown for linkage groups I, II, III, IV, V and X. A high peak is shown to map to the LG IV.

Table 4-1

Annotate variants and types of DNA changes present within the region of linkage shown in the LG IV based on the graphical analysis for the mutant N-64

Figure 4-2

Graphical analysis of the J-72 (*od101*) mutant using Hawaiian Variant Mapping using the CloudMap Pipeline. Scattered plots and Frequency Allele plots are shown for linkage groups I, II, III, IV, V and X. A high peak is shown to map to the LG IV.

Table 4-2

Annotate variants and types of DNA changes present within the region of linkage shown in the LG IV based on the graphical analysis for the mutant J-72 (*od101*).

Figure 4-3

Graphical analysis of the V-128 mutant using Hawaiian Variant Mapping using the CloudMap Pipeline. Scattered plots and Frequency Allele plots are shown for linkage groups I, II, III, IV, V and X. A high peak is shown to map to the LG III.

Table 4-3

Annotate variants and types of DNA changes present within the region of linkage shown in the LG III based on the graphical analysis for the mutant V-128 (od105).

Figure 4-4

Graphical analysis of the M-61 mutant using the Simple Variant Density using the MiModD Pipeline. Scattered plots and Frequency Allele plots are shown for linkage groups I, II, III, IV, V, X and the Mitochondria DNA.

Figure 4-5

Graphical analysis of the B-104A mutant using the Simple Variant Density using the MiModD Pipeline. Scattered plots and Frequency Allele plots are shown for linkage groups I, II, III, IV, V, X and the Mitochondria DNA.

Figure 4-6

Graphical analysis of the T-17 mutant using the Simple Variant Density using the MiModD Pipeline. Scattered plots and Frequency Allele plots are shown for linkage groups I, II, III, IV, V, X and the Mitochondria DNA.

Figure 4-7

Graphical analysis of the T-7 mutant using the Simple Variant Density using the MiModD Pipeline. Scattered plots and Frequency Allele plots are shown for linkage groups I, II, III, IV, V, X and the Mitochondria DNA.

# Chapter V- Interaction of Microtubule Motors with Mitochondrial Fission/Fusion Machinery in the *C. elegans* Neuron.

(Morsci et al., Manuscript in progress. Dr. Morsci is the primary author and has designed and conducted the majority of experiments and quantification. My contribution includes taking images of newly generated strains and videos for kymographs.)

## I. Abstract

Mitochondria are essential for all eukaryotic cells because they participate in functions that are necessary for cell survival. Mitochondrial function relies on the dynamic changes of morphology as well as the ability to be transported to different areas to meet cellular needs. In the case of the neuron, these specialized cells rely on the cellular energy provided by mitochondria because they do not have other reserves. Moreover, transport via the cytoskeleton to distal processes is needed for those localized areas. Many different neurodegenerative diseases have aspects of mitochondrial dysfunction, which is not surprising based on how important mitochondria are. Understanding how both of these processes work together, mitochondrial dynamics and mitochondrial transport, is fundamental in learning more about the neuron and the impact on health and disease.

## II. Introduction

Mitochondria are essential organelles that exist in every cell type. They provide the energy as well as participate in a variety of functions important for the cell; thus, they are necessary for cell survival. They are transported along the cytoskeleton to reach specific areas of the cell, where they can split apart or join up as necessary (fission and fusion), and when damaged they can also undergo removal in the form of mitophagy (*29*). These processes of mitochondrial dynamics and transport are important for all cell

types but particularly for the neuron. Specialized cells like the neuron can have very long processes; thus, mitochondria need to be transported to these areas and in the process of transport can also alter their morphology if needed. (*9, 29, 151, 152*)

The processes of fission and fusion are carried out by canonical machinery first studied in less complex models like yeast and *Drosophila* (*24, 33*). We now know that there are both resident proteins such as mitofusins that mediate fusion of mitochondria, combined with recruited proteins such as DRP-1 that mediate the process of fission. Even though these proteins are found in other model systems, they are highly conserved in mammals. (*153*) Fission and fusion are not only needed for helping mitochondria during cell division to generate new mitochondria for daughter cells but also in the case of stress response when mitochondria are damaged they fuse together to maintain function (*154*). Different cell types have different mitochondrial morphology, but they still use the fission and fusion machinery. For example, in *C. elegans* body wall muscle mitochondria appear as fiber-like networks, whereas in neurons mitochondria are tubular or small and round. *(22, 155)*

Neuronal mitochondria are not only regulated by the dynamics machinery and changes in fusion and fission but also by how they are moved throughout the cell. Proper distribution is important for basal function, but can also become employed for repair in the event of nerve damage (*51*). Movement of mitochondria in neurons is carried out by motor proteins such as Kinesin, which move mitochondria along microtubules (*39, 43*). Other motors and adaptors have also been found to be necessary for the interaction and transport of mitochondria. Some of these include Milton, Miro, and docking proteins such as Syntaphilin. (*37*)

Specialized cells like the neuron can have very long processes and thus mitochondria need to be transported to these areas and in the process can also alter their morphology if needed. (*9, 29, 151, 152*) Mitochondrial function is required for

proper neuronal function, for example, mitochondria are crucial for presynaptic function in a variety of ways. Synapses have been shown to have high energy demands and thus the cellular energy provided by mitochondria is directly used to: maintain membrane potential, prime synaptic vesicles, load synaptic vesicles, endocytosis of synaptic vesicles and even transport of such (*156*). Additionally, mitochondria has also been implicated in directly helping with proper buffering of $Ca^{2+}$ at the synapse, which is an essential during synapse firing. (*156, 157*)

Defects of mitochondria have been implicated in many neurodegenerative diseases including: Alzheimer's disease, Parkinson's disease, Familial amyotrophic lateral sclerosis (FALS), and Huntington's disease. (*158*) We also know that mutations of mitochondrial fusion and fission machinery itself can cause neurodegenerative diseases. There is still a lot that is not known about mitochondria in relation to neurological diseases, especially in relation to how mitochondrial dynamics and transport can contribute to other neurological diseases with unknown aetiology. For this, we need to further understand more about mitochondrial dynamics and transport, for example: is there a correlation between mitochondrial size and transport? Are these processes mediated independently? Or is there a functional link between mitochondrial dynamics and transport in neurons?

For this purpose, we are using the model organism *C. elegans* to study mitochondrial dynamics and transport in the intact neuron. With the worm we've been able to ask some of these questions.

## III. Material Methods

### Strains and Reagents

Animals were grown at 20$^{o}$C on standard NGM plates seeded with OP50 E. coli unless they had specific permissive temperature of 15$^{o}$C. Some strains were provided

by the Caenorhabditis Genetics Center. The following strains were used for this work*: drp-1(cq5), drp-1(tm1108), eat-3(ad426), fzo-1(tm1133), unc-116(e2310), ric-7 (n2657), odIs70*[P*glr-1*::MitoGFP, unc-119(+)], jsIs609 (*Pmec*-7::mito::GFP) (*159*), *C. elegans* N2. The transgenic strains generated by Dr. Morsci include: Ex[*Pglr-1::UNC-116::tagRFP],* and "MitoTruck" *Ex[Pglr-1::UNC-116::tagRFP::TOMM-7].* These strains are maintained with the *pha-1(e2123)*; *him-5(e1490)* background and the "MitoTruck" strain also has a Pttx-3::RFP reporter for maintenance.

## Fluorescence Microscopy

Pictures and videos were taken with Leica Epiflourescent Microscope at either 100x (for imaging), or at 63x (for kymograph movies). Imaging was done in a room with ambient temperature of around 20$^{o}$C in order to prevent temperature to influence morphology of transport. Animals were grown as indicated, picked and placed on 5% agarose pads on microscope slides. They were anesthetized for 4 minutes prior to adding a cover slip using a drop of 10nM Levamisole and M9 solution. Animals were positioned for imaging using an eyelash pick after becoming anesthetized. One animal was imaged at a time to prevent prolonged effects from being on a pad. Images and movies were taken using iVision software. Scripts were either written by former members of the lab or Dr. Morsci.

## Mitochondrial Quantification

The software ImageJ was used quantify mitochondrial size and density in both the ventral cord and the ALM neuron images. Each image was analyzed using the segmented line tool for length of the VNC or the ALM process for the image. As a point of reference for measurements, mitochondria in the image were used. Images were then analyzed using a threshold to select mitochondrial structures automatically. After this,

the outlines were cleaned up manually to quantifying errors by the threshold. Data for mitochondrial size (Feret) as well as other parameters are then transferred to MS Excel to calculate density of mitochondria in the VNC of the ALM process for each image.

## IV. Results

### Examining Mitochondrial Size and Movement

We characterized mitochondrial movement along neuronal axons (interneurons and mechanosensory). Under the wild type background we imaged both of our mitochondrial reporters *odIs70* [*Pglr-1::MitoGFP*] and *jsIs609 [Pmec-7::MitoGFP*] and observed that kymographs of these strains show mitochondria that are smaller in size are moving more than larger size mitochondria (Figure 5-1).

Using the mutant backgrounds for the dynamic machinery we observ

e that defects of either fission or fusion reduce mitochondrial transport but unlike what we saw in a wildtype background. We imaged the following strains as representatives of fusion and fission defects: *fzo-1(tm1133); odIs70* and *drp-1(cq5); odIs70*. Movies taken were used for kymographs and analysis. Quantification was done to determine the number of motile mitochondria as well as to measure the velocity of these mitochondria (Figure 5-2). What we found is that mitochondrial mutants lacking the ability to fuse, *fzo-1(tm1133); odIs70,* show reduced frequency of motile mitochondria despite having smaller sized and normal density of mitochondria along the VNC. Additionally, both mitochondrial run length and velocity is not affected and is comparable to wild type (Figure 5-2B)

In the case of fission mutants, we used the strain *drp-1(cq5); odIs70,* and as expected we observed that mutants show reduced frequency of motile mitochondria (Figure 5-2). As previously seen, our *drp-1(cq5);odIs70* mutants show a reduction of mitochondrial density (mitochondria number) (*22*), which might a contributing factor to

this measurement. During the analysis of motile mitochondria, we noticed a very interesting phenotype that so far has only been observed in *drp-1* mutants. Mitochondria in the ventral cord, especially longer mitochondria seem to initiate movement but abort it and we deemed this a “rubber-band” phenotype (Data not Shown). The mitochondrial velocity of these fission deficient animals shows that both the anterograde and retrograde movement types are reduced as well as the number of mitochondria moving (Figure 5-2B and C).

## Influence of Mitochondrial Motors on Mitochondrial Dynamics

Because we want to understand what the relationship between mitochondrial dynamics and mitochondrial transport is, a starting point is to investigate the key motor UNC-116, that uses mitochondria as cargo in the *C. elegans* neuron. In addition, because we see that even in *drp-1* mutants there are some small mitochondria present we want to understand if this is related to transport machinery or not. Are these small mitochondria, budding-off from larger ones caused as a result of “rubber-band” movement? Is this, caused by motors such as UNC-116 pulling off said mitochondria?

In order to address some of these questions we used double mutant strains of *drp-1(cq5); unc-116(rh24)* and a transgenic strain that overexpresses the UNC-116 motor in the interneurons, Ex[*Pglr-1::UNC-116::tagRFP]*. Preliminary work with the double mutant shows that when both genes are knocked out, there is no mitochondria along the ventral cord and we also see that longer mitochondria are in the cell body and the very proximal neurite (Data not shown). Next, we generated the single mutant *unc-116(rh24);* Ex[*Pglr-1::UNC-116::tagRFP]* and saw that by overexpressing the motor UNC-116, we are able to rescue the *unc-116* phenotype (Figure 5-3). Based on these results, we need to further investigate how the additional availability of motor proteins affects mitochondria in mutants with defects of fusion and fission.

We've generated a strain that in the mutant background *drp-1(cq5)* and the transgenic Ex[*Pglr-1::UNC-116::tagRFP]* and we see that the defects of mitochondrial motility in these animals is not rescued by the influx of motor (Data not shown). We need to investigate this in more detail and measure the motility and any changes in mitochondrial size and density.

## Influence of Mitochondrial Dynamic Machinery on Mitochondrial Motility

One of the questions we also wanted to address was how defects of the mitochondrial machinery affected motility. For this, we are using single and double mutants of the fission and fusion machinery and analyze for changes in mitochondrial density, spacing and ultimately motility of the mitochondria in the ALM neuron. From previous published data, we know that *drp-1(cq5)* mutants show increased mitochondrial size and decreased mitochondrial density along the VNC (*22*). Also both *eat-3(ad426)* and *fzo-1(tm1133*) show reduced size but normal spacing and for eat-3(ad426) slightly lower mitochondrial density (*159*). Double of either fusion proteins and the *drp-1(cq5)* allele show suppression of the elongated mitochondrial size present in *drp-1(cq5)* animals (Figure 5-4, and Data not Shown). Additionally, mitochondrial density in *drp-1(cq5); eat-3(ad426)* double mutants is the same as in *drp-1* levels and *drp-1(cq5); fzo-1(tm1133)* double mutants are the same as wildtype levels (Figure 5-4 and Data not Shown).

## Enhanced Motor Recruitment

In mammals, mitochondrial transport uses not only motor proteins but also adaptors that are used to connect the motors to the mitochondria. Our preliminary results show that overexpression of the UNC-116 motor in the worm might not necessarily rescue the mitochondria motility defects seen in the *drp-1* animals. Because

of this, perhaps these types of defects are caused by failure in the recruitment of the motor or in the adaptor. To bypass the recruitment and adaptors all together, we generated a transgenic strain that directly couples the mitochondria to the motor UNC-116 in the interneurons *Ex[Pglr-1::UNC-116::tagRFP::TOMM-7].* In order to validate this transgenic strain, we crossed it to both the *ric-7(n2657)* and *unc-116(e2310)* mutants and saw that it was able to rescue both phenotypes which means that direct recruitment of the motors can restore transport of some mitochondria (Figure 5-5). Quantification still needs to be done for this recent data.

## V. Discussion

We conducted this work looking at mitochondria in two different neuronal types in the worm, the interneurons and the mechanosensory neurons. These two types of neurons have slightly different characteristics and different functions in the animal. Asking some of these questions might be relevant to one type but not the other. For example, mitochondrial spacing has been well characterized before in mechanosensory ALM neuron (*159*). On the other hand what we learn from either or both might me important to understanding neuronal mitochondria globally in the animal.

Mitochondria transport in both the mammalian field has found that smaller mitochondria are more motile than larger mitochondria (*160*). We found that in the mechanosensory and the interneurons of the worm this hold true (Fig. 5-1). We saw this by analyzing kymographs of both our mitochondrial reporters, even in the interneuron where the ventral nerve cord is very dense of mitochondrial structures. Because our interest was to understand how mitochondrial dynamic machinery is working with transport proteins, we found that defects fission machinery causes an interesting phenotype of start-abort and stretch. This aborted transport was termed “rubber-band” to

help our descriptions. Only mutants of the fission machinery *drp-1(cq5)* was found to have this phenotype.

Mutants of the fission machinery was also found to have four times reduced frequency of motile mitochondria. Because, these are DRP-1 mutants we expected this due to their mitochondrial elongation. Mitochondrial velocity was also reduced in these mutants and this might due to the size of the mitochondria as well as the “rubber-band” phenotype we observed. This could also be due to structural changes in the DRP-1 proteins. As noted in earlier chapters, recent reports exploring the structure of DRP1 in mammalian field found that specific domains interact with adaptors in the cell such as MID49. Even though there is no ortholog for this adaptor, there is a possibility that specific domain in the worm DRP1 interact with similar adaptors that might play a role in the cargo-motor connections as well as membrane proteins for the process of fission.

The mutants of the fusion machinery, FZO-1 was found to have significantly less frequency of motile mitochondria but wild type levels of mitochondrial velocity. This is rather unexpected since mitochondrial size in the fusion mutants is by definition small. Again, we hypothesize that there could be structural defects causing the mitochondrial to move less frequently but more work will need to be done to address this question.

One aspect of the *drp-1* phenotype regarding mitochondrial transport that we wanted to address was the availability of motor proteins. Because fission mutants have longer mitochondria, less motile mitochondria and lower mitochondrial velocity we wanted to ask if more available UNC-116 motors could rescue the phenotype seen here. Preliminary analysis of double *drp*-1; *unc-116* mutants generated show no mitochondria along the VNC and long mitochondria that wraps around the cell body but doesn’t leave it as far as the very nearby region of the proximal axon. More images and quantification need to be done with this strain but if this holds true it might be that both motors and fusion machinery might be interacting indirectly or directly.

Using a transgenic line created in our lab which overexpresses UNC-116 in the interneurons. This transgenic strain was then used for crossing into *unc-116* mutants and we observed a recovery of the mitochondrial transport phenotype. With these results we then crossed the transgenic strain into the *drp*-1 mutants and preliminary imaging points to the fact that the mitochondrial transport defect is not recovered. This might mean that motor availability is not the reason for the transport defects but potentially, the connections between that adaptors make between motors and the mitochondrial cargo.

In the ALM neuron, defects of the fission machinery cause a decrease in mitochondrial density and an increase in mitochondrial size. When there are defects of the fusion machinery, in the ALM there is a slight decrease in mitochondrial density and size. But in double mutants of both fission and fusion (*drp-1; eat-3)* machinery, there is a restoration of the mitochondrial size but not of mitochondrial density. With these strains available we will begin to analyze for mitochondrial transport in the ALM.

One of the aspects that we hypothesize from the *drp-1* phenotypes and the overexpression of UNC-116 motor results is that adaptors might be playing a role in determining the link between dynamic machinery and transport. For this, we generated a transgenic reporter that couples the mitochondria directly to the UNC-116 motor. This was previous done in another report in the ALM neuron and was called “MitoTruck” (*51*). In this report they were able to use the “MitoTruck” transgene to move mitochondria to the axons of the ALM. There are two great examples of transport defects *unc-116* and the *ric-7* phenotypes. The *ric-7* mutant shows no mitochondria along the VNC. RIC-7 is a new protein that has been found to be having a role in mitochondrial transport. Initially, it was found in as a mutant “resistant to inhibitors of cholinesterase) and is required for neuropeptide secretion. As we’ve seen previously the *unc-116* phenotype shows very few and small mitochondria in the VNC. For both of these mutants *unc-116* and the *ric-7,* the “MitoTruck” reporter in the interneurons was able to rescue the transport defects.

With this information we believe that adaptors, rather than motors, are limiting transport. We still need to investigate if the “MitoTruck” transgene, can bypass the transport defects seen in the *drp-1* mutants.

Overall, with this data we are beginning to answer how does mitochondrial canonical fusion/fission machinery interact with the transport machinery in the worm neuron. We will need to continue analyzing strains generated and generate a few more to ask more robust questions regarding the direct interaction.

## VI. Figures

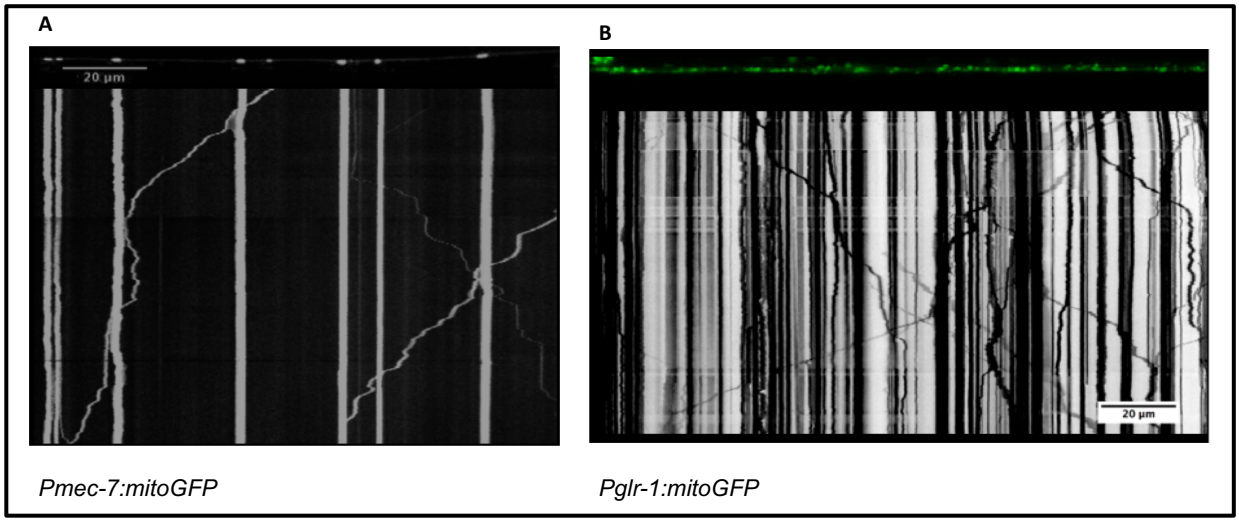


Figure 5-1

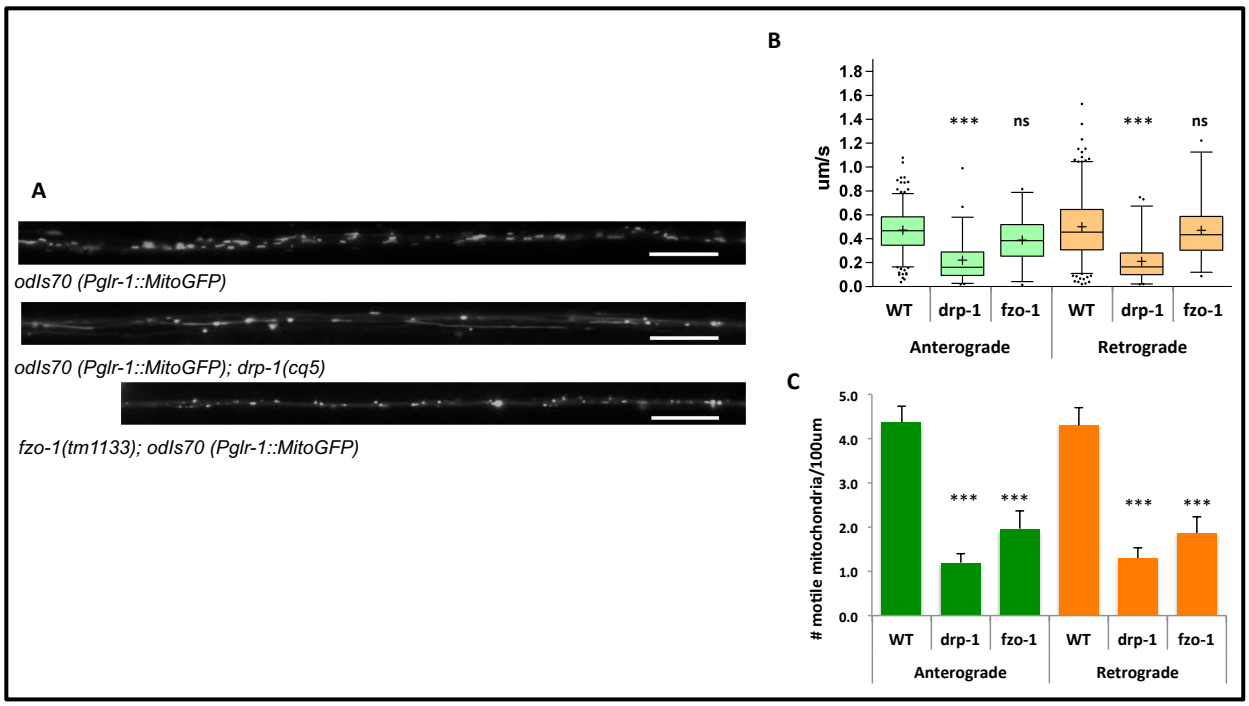


Figure 5-2

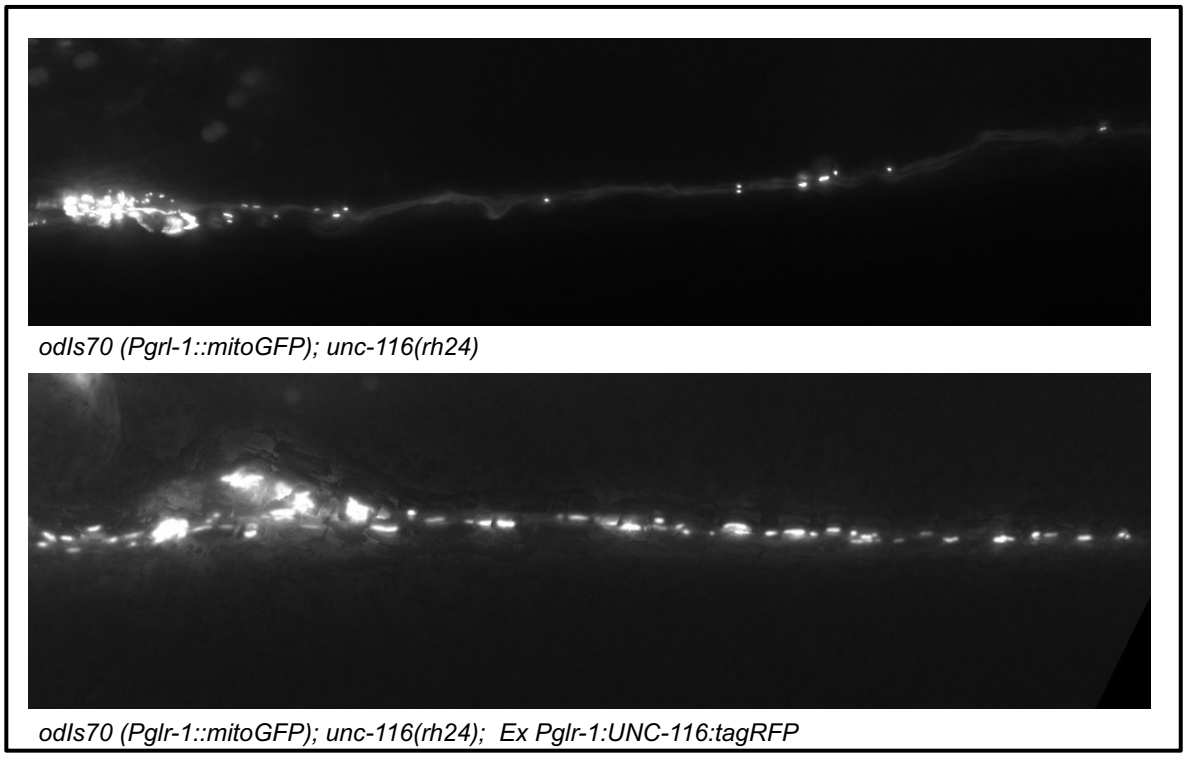


Figure 5-3

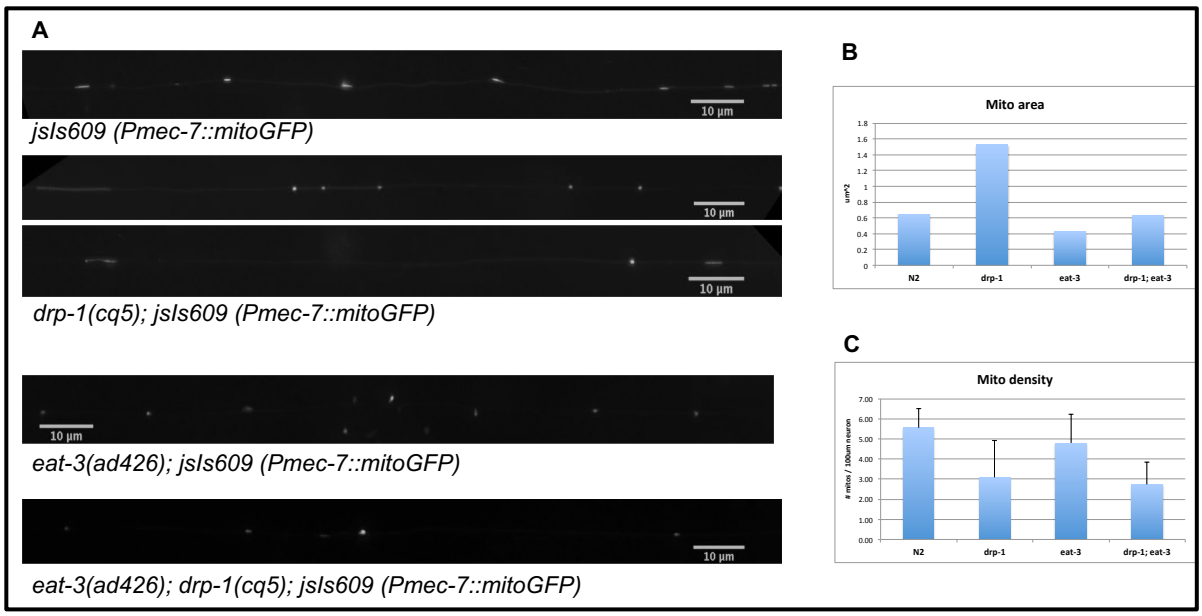


Figure 5-4

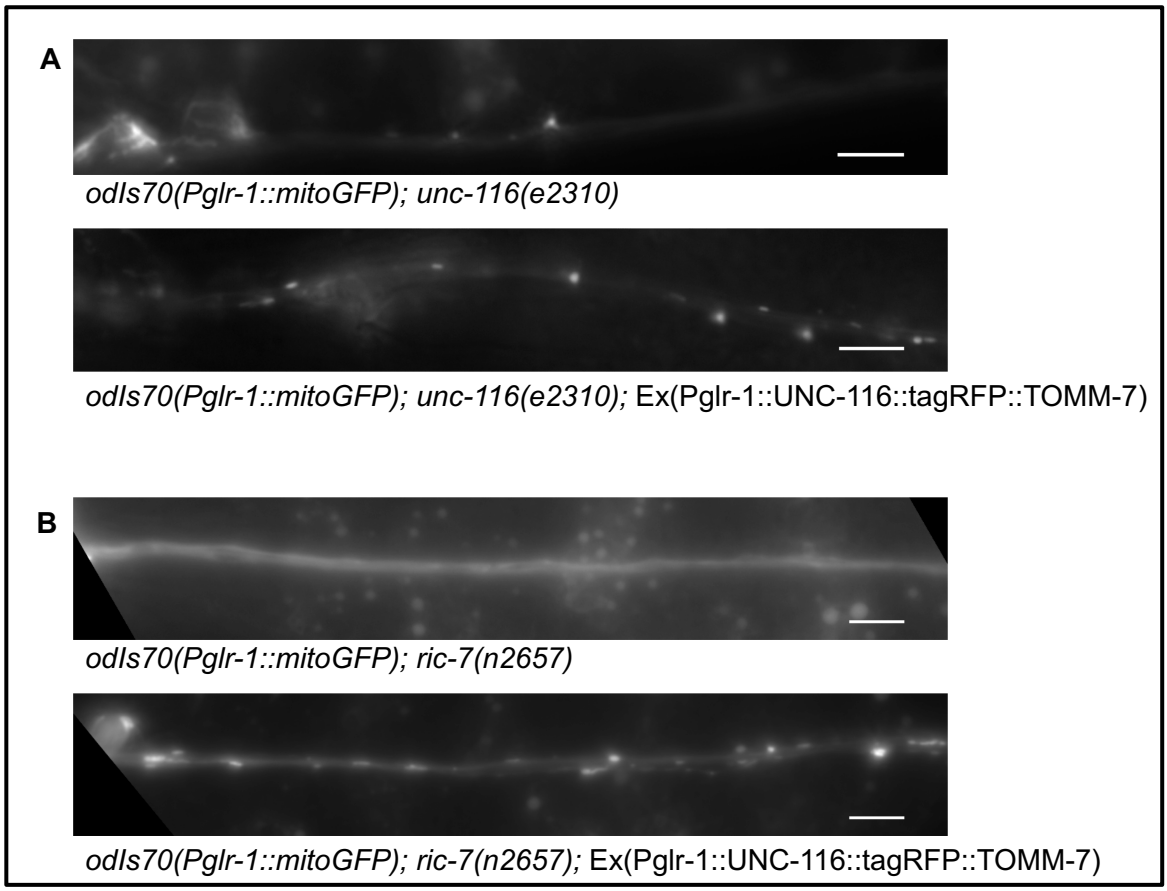


Figure 5-5

## VII. Figure Legends

Figure 5-1

Examining Mitochondrial Size and Movement in C. elegans neurons. (A) Distal ALM was imaged using the *Pmec-7::mitoGFP* reporter. Series of images spanning 5 minutes were taken to create a kymograph to analyze movement. Smaller mitochondria appear to be moving bigger distances than the larger mitochondria. (B) The ventral nerve cord was imaged using the reporter *Pglr-1::mitoGFP.* Images were taken for 5 minutes using 63x magnification and used to make a Kymograph. Mitochondria that are moving for longer distances and more often are smaller in size than larger mitochondria that are in the spot for the 5 minutes.

Figure 5-2

Mitochondria movement is influenced by fusion and fission machinery. (A). Representative images of strains generated used for motility assays. Strains used include: wild type *odIs70 (Pgrl-1::mitoGFP),* fission deficient *odIs70 (Pglr-1::MitoGFP); drp-1(cq5),* and fusion deficient *fzo-1(tm1133); odIs70 (Pglr-1::MitoGFP)*. (B) Mitochondrial velocity in the anterograde and retrograde direction for each strain. The *drp-1* strain shows significant decrease of both directions when compared to wild type. The *fzo-1* strains doesn't show a different velocity than wild type. (C) Number of motile mitochondria that are moving in both the anterograde and retrograde direction was measured and both the *drp-1* and the *fzo-1* strains show a significant decrease when compared to wild wild type.

Figure 5-3

Rescue of mitochondrial movement by overexpression of kinesin-1 motors. (Top) Representative image of the transport deficient *odIs70 (Pgrl-1::mitoGFP); unc-116(rh24)* showing the decrease of mitochondria density in the ventral nerve cord due to the mutation in the kinesin-1 motor UNC-116. (Bottom) An transgenic construct was introduced into the *odIs70 (Pgrl-1::mitoGFP); unc-116(rh24)* strain using a promotor for expression in the interneurons only. This representative image shows that mitochondria density seems to be rescued by the introduction of additional motors.

Figure 5-4

Influence of mitochondrial dynamic machinery on mitochondrial motility. (A) Representative images of the mechanosensory mitochondrial reporter *jsIs609 (Pmec-7::mitoGFP)* along with fission defective mutant *drp-1(cq5); jsIs609 (Pmec-7::mitoGFP)*, the fusion defective *eat-3(ad426); jsIs609 (Pmec-7::mitoGFP)*, and the double mutant *eat-3(ad426); drp-1(cq5); jsIs609 (Pmec-7::mitoGFP).* (B) Mitochondrial area was quantified for all four strains. Fusion mutant *drp-1* shows to have a bigger mitochondrial area when compared to wild type. The fusion mutant *eat-3* has less mitochondrial area than wild type. The double mutant *drp1-; eat-3* shows wild type levels of mitochondrial area and seems to rescue the defects seen in either single mutant.

Figure 5-5

Enhanced motor recruitment rescues mitochondrial transport defects. Transgenic constructs were generated to directly couple the mitochondrial UNC-116 motor to the mitochondria and bypassing adaptors for the cargo. Constructs were then introduced to the wild type *odIs70 (Pglr-1::mitoGFP )* strain to use for crosses. (A) Representative images analyzing the interneuron mitochondrial reporter with a transport deficient

mutation *odIs70(Pglr-1::mitoGFP); unc-116(e2310).* (Bottom of A) Representative image from strains generated from cross with transgenic construct above. The *odIs70(Pglr-1::mitoGFP); unc-116(e2310);* Ex(Pglr-1::UNC-116::tagRFP::TOMM-7) strain shows that there is a rescue of mitochondrial motility out of the cell body and into the VNC. (B) Representative images analyzing the interneuron mitochondrial reporter with a transport deficient mutation *odIs70(Pglr-1::mitoGFP); ric-1(n2657).* (Bottom of B) Representative of strain from cross with transgenic construct. This *odIs70(Pglr-1::mitoGFP); ric-7(n2657);* Ex(*Pglr-1::UNC-116::tagRFP::TOMM-7)* animals show that there is also a rescue of mitochondrial motility out of the cell body and into the VNC.

# Chapter VI- Discussion and Future Directions

## I. Investigating DRP-1 Stability and Function

We were able to isolate three new alleles of the fission gene *drp-1* from our forward genetic screen. These new alleles include *drp-1(od96)*, *drp-1(od97)* and *drp-1 (od98)*. Based on the DNA modifications and their location in the predicted putative protein, some of these alleles will be interesting to investigate as far as protein stability and activity. Structural analysis of mammalian Drp1 shows that key structures in the protein interact with specific proteins for recruitment and possible for the fission activity as well (*34*). Given this information and preliminary analysis of our alleles, both *drp-1(od97) and drp-1(od98)* are within critical structures of the protein. By studying how these mutations are affect activity of the protein and its interaction with other proteins during fission or other processes will help us understand how is DRP-1 working.

## II. Novel Genes Regulating Mitochondrial Transport

To date, we have mapped two of our mutants and found that these are novel genes and not part of the canonical mitochondrial transport machinery. We still need to validate their identity via gene editing rescue or transgenic rescue. Our mutant J-72 (*od101*), who has decreased mitochondrial density as well as axonal guidance defects and an uncoordinated and dumpy body, is a new allele of *unc-44.* The *unc-44* gene is the ankyrin gene in *C. elegans*, which is important for axonal guidance as well as anchoring membrane proteins to the cytoskeleton. Because of this, we believe that UNC-44 might be promoting or even regulating the kinesin motor or adaptors of mitochondria.

Our second mapped mutant V-128 (*od105*), which showed a decrease in mitochondrial density as well as partial sterility was mapped as well. We found that this

mutant is a new allele of the *mtx-2* gene. The *mtx-2* gene is the orthologue for human Metaxin-2, which is a mitochondrial import protein, potentially connecting the mitochondrial import machinery and mitochondrial transport. We hypothesize that the Metaxin component of the import machinery plays an additional role of interacting with mitochondrial motors and their adaptors.

Understanding how these genes directly influence mitochondrial transport starts by investigating more about their protein localization. For this we will generate transgenes that encode each protein fused in frame to GFP or tagRFP to determine in which tissues they are expressed, as well as their site of subcellular localization. We expect that they act cell autonomously in neurons, and we will test this directly by expressing their proteins only in neurons in otherwise mutant animals using tissue specific promoters. Given the large size of the *unc-44* gene, we will use CRISPR-based methods rather than standard transgenic arrays. If we observe that these proteins are expressed in other tissues (e.g., muscle, hypodermis, intestine), we already have transgenic lines in the lab that will allow us to examine mitochondria in these tissues.

Second, we will use known null mutants of mitochondrial dynamics and transport machinery, crossing them into our *mtx-2* and *unc-44* mutants to check for phenotypic changes that either suppress or enhance the mutant phenotype. We will examine mutants for other factors that have been implicated in either UNC-44 or MTX-2 function to see if they are involved in mitochondrial transport. We can also study impact of the proteins in the transport and mitochondrial dynamics by using tagged versions of DRP-1, EAT-3, and UNC-116. For our *unc-44* mutant, we can study if the movement of cargo that is transported by different known motors is also impaired in our mutants. For this, we can use tagged versions of GLR-1, which is transported by UNC-116/KIF5 motors, and SNB-1, which is transported by UNC-104/KIF1A motors, in the interneurons to see if our mutants disrupt their transport along the axons. We can also perform time lapse and

kymograph analysis to measure the fraction of mobile mitochondria and their rates of movement in our various single and double mutant combinations.

Finally, we developed a chimeric motor, UNC-116::TOMM-7, that directly tethers to the mitochondria rather than using adaptor proteins. Adaptors have often been found to be the limiting component for kinesin-based transport. Thus, with this reagent, we can address the question regarding if there are direct interactions between mitochondria, UNC-44, motor adaptors, and MTX-2. That is, by linking mitochondria directly to the motor, can we bypass the requirement for either UNC-44 or MTX-2.

We will use genetically encoded fluorescent reporters generated in our lab to interrogate mitochondrial function and quality in *unc-44* and *mtx-2* mutant interneurons. Defective mitochondria produce Reactive Oxygen Species (ROS). We will use a transgene that expresses MitoROGFP in the interneurons to determine if mitochondria are undergoing oxidative stress in our mutants. MitoROGFP is a mitochondrially-localized, GFP-based ROS detector that contains a pair of cysteines that become disulfide linked under oxidizing conditions and reorient the GFP's chromophore. This oxidation is reversible, making MitoROGFP reporter temporally dynamic. Oxidized MitoROGFP is excited at 400nm, whereas reduced MitoROGFP is excited at 490nm. The ratios of fluorescence excitation provide a readout of the local ROS environment (*22*) (*161*).

Damaged mitochondria undergo selective autophagy (mitophagy), including engulfment in autophagosomes, fusion with lysosomes, and breakdown in the low pH environment. This process can be monitored using a transgene that expresses MitoKeima in the interneurons. MitoKeima is a mitochondrially-localized fluorescent protein that is stable in the low pH environment of the lysosome. At neutral pH, MitoKeima is excited at 450nm, whereas at acidic pH, it is excited at 560 nm. The ratios of fluorescence excitation provide a dynamica and reversible readout of the local pH

environment surrounding the mitochondria, allowing us to monitor the uptake of mitochondria into autolysosomal structures. We can also examine the colocalization of MitoCherry with LGG-1::GFP, a marker for autophagosomes, to monitor mitophagy.

Taken together, these various reporters will allow us to determine whether mitochondria are undergoing oxidative stress and mitophagy, which could explain the decreased total mitochondrial load in the *unc-44* and *mtx-2* mutants. They will allow us to determine where in neurons these mitochondria are being removed (e.g., the soma versus the axons), and whether the mobility and direction of mitochondrial movement correlate with mitochondrial health or mitophagy.

Much remains to be understood with respect to mitochondrial dynamics and transport. Our forward genetic screen, although not carried to saturation, identified two new regulators participating in or regulating both processes. By characterizing these genes and their protein products, we hope to understand how these players work in conjunction with the known machinery or in parallel pathways in mitochondrial transport and/or dynamics.

Because of the polarity of neurons, mitochondria need to be mobilized to the dendrites and axons and this has been shown to carried out by using both the cell's cytoskeleton as well as combinations of motors, adaptors and docking proteins. A big aspect of mitochondrial function is the fact that this organelle undergoes morphological changes such as fission and fusion. We are beginning to answer how do both of these aspects interact in the intact neuron, fission/fusion and mitochondrial transport. At this point our data points to the fact that adaptors rather than motors are the limiting factor of transport. We also hypothesize that the fission machinery, DRP-1 might have structural features that interact with transport machinery as this is the one mutant that shows decreased velocity, decreased in frequency of motile mitochondria and also an aborted initiation term "rubber-band" movement. We need to continue generating strains to ask

additional questions in this story to find out more about how the transport and mitochondrial dynamics are interacting with one another.

In conclusion, the work shown in this thesis tries to address key questions that are still open in the field of mitochondrial dynamics and transport. From the published work, we now know how mitochondria change in response to anoxic stress and how it uses proteins in the hypoxia response and oxidative response pathway to do so. From our forward genetic screen, we have at least two novel genes that are playing a role in mitochondrial transport. From our last chapter, we are beginning to understand how the mitochondrial dynamic machinery interacts with mitochondrial transport machinery in vivo. These findings may help us further understand mitochondria in the neuron and can therefore help us understand the implications to human health.

References


1. D. F. Tapley, D. V. Kimberg, J. L. Buchanan, The Mitochondrion. *New England Journal of Medicine* **276**, 1124-1132 (1967).
2. M. W. Gray, G. Burger, B. F. Lang, Mitochondrial evolution. *Science (New York, N.Y.)* **283**, 1476-1481 (1999).
3. B. F. Lang, M. W. Gray, G. Burger, Mitochondrial genome evolution and the origin of eukaryotes. *Annual review of genetics* **33**, 351-397 (1999).
4. B. Lemire, Mitochondrial genetics. *WormBook*, 1-10 (2005).
5. S. Brenner, The Genetics of CAENORHABDITIS ELEGANS. *Genetics* **77**, 71-94 (1974).
6. I. E. Scheffler, in *Mitochondria,* I. E. Scheffler, Ed. (John Wiley & Sons, Inc., New York, NY, 1999), pp. 1-7.
7. I. E. Scheffler, A century of mitochondrial research: achievements and perspectives. *Mitochondrion* **1**, 3-31 (2001).
8. K. S. Dimmer *et al.*, Genetic basis of mitochondrial function and morphology in Saccharomyces cerevisiae. *Molecular biology of the cell* **13**, 847-853 (2002).
9. H. M. McBride, M. Neuspiel, S. Wasiak, Mitochondria: more than just a powerhouse. *Current biology : CB* **16**, R551-560 (2006).
10. M. Saraste, Oxidative phosphorylation at the fin de siecle. *Science (New York, N.Y.)* **283**, 1488-1493 (1999).
11. K. K. Gunter, T. E. Gunter, Transport of calcium by mitochondria. *Journal of bioenergetics and biomembranes* **26**, 471-485 (1994).
12. T. Pozzan, R. Rizzuto, High tide of calcium in mitochondria. *Nature cell biology* **2**, E25-E27 (2000).
13. J. A. Gilabert, in *Calcium Signaling,* M. S. Islam, Ed. (Springer Dordrecht Heidelberg, New York, 2012).
14. F. S. Sjostrand, Electron Microscopy of Mitochondria and Cytoplasmic Double Membranes: Ultra-Structure of Rod-shaped Mitochondria. *Nature* **171**, 30-31 (1953).
15. G. E. Palade, The fine structure of mitochondria. *Anat Rec* **114**, 427-451 (1952).
16. C. A. Mannella, Structure and dynamics of the mitochondrial inner membrane cristae. *Biochimica et biophysica acta* **1763**, 542-548 (2006).
17. V. C. Fogg, N. J. Lanning, J. P. Mackeigan, Mitochondria in cancer: at the crossroads of life and death. *Chin J Cancer* **30**, 526-539 (2011).
18. R. Rizzuto *et al.*, Close contacts with the endoplasmic reticulum as determinants of mitochondrial Ca2+ responses. *Science (New York, N.Y.)* **280**, 1763-1766 (1998).
19. D. A. Rube, A. M. van der Bliek, Mitochondrial morphology is dynamic and varied. *Mol Cell Biochem* **256-257**, 331-339 (2004).
20. R. Rossignol *et al.*, Energy substrate modulates mitochondrial structure and oxidative capacity in cancer cells. *Cancer Res* **64**, 985-993 (2004).
21. D. Tondera *et al.*, SLP-2 is required for stress-induced mitochondrial hyperfusion. *EMBO J* **28**, 1589-1600 (2009).
22. P. Ghose, E. C. Park, A. Tabakin, N. Salazar-Vasquez, C. Rongo, Anoxia-reoxygenation regulates mitochondrial dynamics through the hypoxia response pathway, SKN-1/Nrf, and stomatin-like protein STL-1/SLP-2. *PLoS Genet* **9**, e1004063 (2013).
23. D. Santos, S. M. Cardoso, Mitochondrial dynamics and neuronal fate in Parkinson's disease. *Mitochondrion* **12**, 428-437 (2012).
24. K. G. Hales, M. T. Fuller, Developmentally regulated mitochondrial fusion mediated by a conserved, novel, predicted GTPase. *Cell* **90**, 121-129 (1997).

25. A. Santel, M. T. Fuller, Control of mitochondrial morphology by a human mitofusin. *Journal of cell science* **114**, 867-874 (2001).
26. G. Marsboom *et al.*, Dynamin-related protein 1-mediated mitochondrial mitotic fission permits hyperproliferation of vascular smooth muscle cells and offers a novel therapeutic target in pulmonary hypertension. *Circ Res* **110**, 1484-1497 (2012).
27. T. Misaka, T. Miyashita, Y. Kubo, Primary structure of a dynamin-related mouse mitochondrial GTPase and its distribution in brain, subcellular localization, and effect on mitochondrial morphology. *The Journal of biological chemistry* **277**, 15834-15842 (2002).
28. T. Kanazawa *et al.*, The *C. elegans* Opa1 Homologue EAT-3 is Essential for Resistance to Free Radicals. *PLoS Genetics* **4**, (2008).
29. D. C. Chan, Mitochondrial fusion and fission in mammals. *Annu Rev Cell Dev Biol* **22**, 79-99 (2006).
30. T. Koshiba *et al.*, Structural basis of mitochondrial tethering by mitofusin complexes. *Science (New York, N.Y.)* **305**, 858-862 (2004).
31. B. DuBoff, J. Gotz, M. B. Feany, Tau Promotes Neurodegeneration via DRP1 Mislocalization In Vivo. *Neuron* **75**, 6180638 (2012).
32. E. Smirnova, L. Griparic, D. L. Shurland, A. M. van der Bliek, Dynamin-related protein Drp1 is required for mitochondrial division in mammalian cells. *Molecular biology of the cell* **12**, 2245-2256 (2001).
33. A. D. Mozdy, J. M. McCaffery, J. M. Shaw, Dnm1p GTPase-mediated mitochondrial fission is a multi-step process requiring the novel integral membrane component Fis1p. *The Journal of cell biology* **151**, 367-380 (2000).
34. R. Kalia *et al.*, Structural basis of mitochondrial receptor binding and constriction by DRP1. *Nature* **558**, 401-405 (2018).
35. M. P. Yaffe, The machinery of mitochondrial inheritance and behavior. *Science (New York, N.Y.)* **283**, 1493-1497 (1999).
36. M. P. Yaffe *et al.*, Microtubules mediate mitochondrial distribution in fission yeast. *Proceedings of the National Academy of Sciences of the United States of America* **93**, 11664-11668 (1996).
37. Q. Cai, Z. H. Sheng, Mitochondrial transport and docking in axons. *Experimental neurology* **218**, 257-267 (2009).
38. C. L. Zhang, P. L. Ho, D. B. Kintner, D. Sun, S. Y. Chiu, Activity-dependent regulation of mitochondrial motility by calcium and Na/K-ATPase at nodes of Ranvier of myelinated nerves. *The Journal of neuroscience : the official journal of the Society for Neuroscience* **30**, 3555-3566 (2010).
39. A. D. Pilling, D. Horiuchi, C. M. Lively, W. M. Saxton, Kinesin-1 and Dynein are the primary motors for fast transport of mitochondria in Drosophila motor axons. *Molecular biology of the cell* **17**, 2057-2068 (2006).
40. R. S. Stowers, L. J. Megeath, J. Gorska-Andrzejak, I. A. Meinertzhagen, T. L. Schwarz, Axonal transport of mitochondria to synapses depends on milton, a novel Drosophila protein. *Neuron* **36**, 1063-1077 (2002).
41. X. Guo *et al.*, The GTPase dMiro is required for axonal transport of mitochondria to Drosophila synapses. *Neuron* **47**, 379-393 (2005).
42. J. S. Kang *et al.*, Docking of axonal mitochondria by syntaphilin controls their mobility and affects short-term facilitation. *Cell* **132**, 137-148 (2008).
43. K. Tanaka, Y. Sugiura, R. Ichishita, K. Mihara, T. Oka, KLP6: a newly identified kinesin that regulates the morphology and transport of mitochondria in neuronal cells. *Journal of cell science* **124**, 2457-2465 (2011).

44. D. Pathak, K. J. Sepp, P. J. Hollenbeck, Evidence that myosin activity opposes microtubule-based axonal transport of mitochondria. *The Journal of neuroscience : the official journal of the Society for Neuroscience* **30**, 8984-8992 (2010).
45. Y. Tanaka *et al.*, Targeted disruption of mouse conventional kinesin heavy chain, kif5B, results in abnormal perinuclear clustering of mitochondria. *Cell* **93**, 1147-1158 (1998).
46. R. D. Vale, The molecular motor toolbox for intracellular transport. *Cell* **112**, 467-480 (2003).
47. M. Nangaku *et al.*, KIF1B, a novel microtubule plus end-directed monomeric motor protein for transport of mitochondria. *Cell* **79**, 1209-1220 (1994).
48. N. Patel, D. Thierry-Mieg, J. R. Mancillas, Cloning by insertional mutagenesis of a cDNA encoding Caenorhabditis elegans kinesin heavy chain. *Proceedings of the National Academy of Sciences of the United States of America* **90**, 9181-9185 (1993).
49. N. Hirokawa, R. Takemura, Molecular motors and mechanisms of directional transport in neurons. *Nature reviews. Neuroscience* **6**, 201-214 (2005).
50. J. Yan *et al.*, Kinesin-1 regulates dendrite microtubule polarity in Caenorhabditis elegans. *eLife* **2**, e00133 (2013).
51. R. L. Rawson *et al.*, Axons degenerate in the absence of mitochondria in C. elegans. *Current biology : CB* **24**, 760-765 (2014).
52. G. R. Sure *et al.*, UNC-16/JIP3 and UNC-76/FEZ1 limit the density of mitochondria in C. elegans neurons by maintaining the balance of anterograde and retrograde mitochondrial transport. *Scientific reports* **8**, 8938 (2018).
53. R. J. Youle, D. P. Narendra, Mechanisms of mitophagy. *Nature reviews. Molecular cell biology* **12**, 9-14 (2011).
54. A. M. Pickrell, R. J. Youle, The roles of PINK1, parkin, and mitochondrial fidelity in Parkinson's disease. *Neuron* **85**, 257-273 (2015).
55. T. Kitada *et al.*, Mutations in the parkin gene cause autosomal recessive juvenile parkinsonism. *Nature* **392**, 605 (1998).
56. E. M. Valente *et al.*, Hereditary early-onset Parkinson's disease caused by mutations in PINK1. *Science (New York, N.Y.)* **304**, 1158-1160 (2004).
57. T. Kanki, K. Furukawa, S. Yamashita, Mitophagy in yeast: Molecular mechanisms and physiological role. *Biochimica et biophysica acta* **1853**, 2756-2765 (2015).
58. V. Contamine, M. Picard, Maintenance and integrity of the mitochondrial genome: a plethora of nuclear genes in the budding yeast. *Microbiology and molecular biology reviews : MMBR* **64**, 281-315 (2000).
59. I. J. Holt, A. E. Harding, J. A. Morgan-Hughes, Deletions of muscle mitochondrial DNA in patients with mitochondrial myopathies. *Nature* **331**, 717-719 (1988).
60. J. Finsterer, Inherited mitochondrial neuropathies. *J Neurol Sci* **304**, 9-16 (2011).
61. A. Olichon *et al.*, Mitochondrial dynamics and disease, OPA1. *Biochimica et biophysica acta* **1763**, 500-509 (2006).
62. G. Zivkovic, L. T. Buck, Regulation of AMPA Receptor Currents by Mitochondrial ATP-Sensitive K+ Channels in Anoxic Turtle Neurons. *Journal of Neurophysiology* **104**, 1913-1922 (2010).
63. M. E. Pamenter, D. S.-H. Shin, M. Cooray, L. T. Buck, Mitochondrial ATP-sensitive K+ channels regulate NMDAR activity in the cortex of the anoxic western painted turtle. *The Journal of Physiology* **586**, 1043-1058 (2008).
64. Damian Seung-Ho Shin, Leslie Thomas Buck, Effect of Anoxia and Pharmacological Anoxia on Whole-Cell NMDA Receptor Currents in Cortical Neurons from the Western Painted Turtle. *Physiological and Biochemical Zoology* **76**, 41-51 (2003).

65. C.-D. Zhu, Z.-H. Wang, B. Yan, Strategies for hypoxia adaptation in fish species: a review. *Journal of Comparative Physiology B* **183**, 1005-1013 (2013).
66. A. B. Zepeda *et al.*, Cellular and molecular mechanisms in the hypoxic tissue: role of HIF-1 and ROS. *Cell Biochem Funct*, (2013).
67. A. Corcoran, J. J. O'Connor, Hypoxia-inducible factor signalling mechanisms in the central nervous system. *Acta Physiol (Oxf)*, (2013).
68. F. W. Marcoux, R. B. Morawetz, R. M. Crowell, U. DeGirolami, J. H. Halsey, Jr., Differential regional vulnerability in transient focal cerebral ischemia. *Stroke* **13**, 339-346 (1982).
69. F. Liu, L. D. McCullough, Interactions between age, sex, and hormones in experimental ischemic stroke. *Neurochem Int* **61**, 1255-1265 (2012).
70. K. Abe *et al.*, Ischemic delayed neuronal death. A mitochondrial hypothesis. *Stroke* **26**, 1478-1489 (1995).
71. R. P. Singh, K. Franke, B. Wielockx, Hypoxia-mediated regulation of stem cell fate. *High Alt Med Biol* **13**, 162-168 (2012).
72. Y. Kim, Q. Lin, P. M. Glazer, Z. Yun, Hypoxic tumor microenvironment and cancer cell differentiation. *Curr Mol Med* **9**, 425-434 (2009).
73. S. Sen Banerjee *et al.*, HIF-prolyl hydroxylases and cardiovascular diseases. *Toxicol Mech Methods* **22**, 347-358 (2012).
74. S. K. Goswami, D. K. Das, Oxygen Sensing, Cardiac Ischemia, HIF-1alpha and Some Emerging Concepts. *Curr Cardiol Rev* **6**, 265-273 (2010).
75. H. K. Eltzschig, T. Eckle, Ischemia and reperfusion--from mechanism to translation. *Nat Med* **17**, 1391-1401 (2011).
76. J. J. Lemasters, T. P. Theruvath, Z. Zhong, A. L. Nieminen, Mitochondrial calcium and the permeability transition in cell death. *Biochim Biophys Acta* **1787**, 1395-1401 (2009).
77. E. Murphy, C. Steenbergen, Mechanisms underlying acute protection from cardiac ischemia-reperfusion injury. *Physiol Rev* **88**, 581-609 (2008).
78. P. S. Brookes, Y. Yoon, J. L. Robotham, M. W. Anders, S. S. Sheu, Calcium, ATP, and ROS: a mitochondrial love-hate triangle. *Am J Physiol Cell Physiol* **287**, C817-833 (2004).
79. T. E. Shutt, H. M. McBride, Staying cool in difficult times: mitochondrial dynamics, quality control and the stress response. *Biochimica et biophysica acta* **1833**, 417-424 (2013).
80. X. Liu, G. Hajnoczky, Altered fusion dynamics underlie unique morphological changes in mitochondria during hypoxia-reoxygenation stress. *Cell Death Differ* **18**, 1561-1572 (2011).
81. K. Itoh, K. Nakamura, M. Iijima, H. Sesaki, Mitochondrial dynamics in neurodegeneration. *Trends Cell Biol* **23**, 64-71 (2013).
82. B. DuBoff, M. Feany, J. Gotz, Why size matters - balancing mitochondrial dynamics in Alzheimer's disease. *Trends Neurosci* **36**, 325-335 (2013).
83. G. L. Anderson, D. B. Dusenbery, Critical-Oxygen Tension of Caenorhabditis elegans. *J Nematol* **9**, 253-254 (1977).
84. W. A. Van Voorhies, S. Ward, Broad oxygen tolerance in the nematode Caenorhabditis elegans. *J Exp Biol* **203**, 2467-2478 (2000).
85. J. A. Powell-Coffman, Hypoxia signaling and resistance in C. elegans. *Trends Endocrinol Metab* **21**, 435-440 (2010).
86. R. Pocock, O. Hobert, Oxygen levels affect axon guidance and neuronal migration in Caenorhabditis elegans. *Nature neuroscience* **11**, 894-900 (2008).
87. A. J. Chang, C. I. Bargmann, Hypoxia and the HIF-1 transcriptional pathway reorganize a neuronal circuit for oxygen-dependent behavior in Caenorhabditis

elegans. *Proceedings of the National Academy of Sciences of the United States of America* **105**, 7321-7326 (2008).
88. B. H. Cheung, M. Cohen, C. Rogers, O. Albayram, M. de Bono, Experience-dependent modulation of C. elegans behavior by ambient oxygen. *Curr Biol* **15**, 905-917 (2005).
89. D. K. Ma, R. Vozdek, N. Bhatla, H. R. Horvitz, CYSL-1 interacts with the O2-sensing hydroxylase EGL-9 to promote H2S-modulated hypoxia-induced behavioral plasticity in C. elegans. *Neuron* **73**, 925-940 (2012).
90. E. C. Park *et al.*, Hypoxia regulates glutamate receptor trafficking through an HIF-independent mechanism. *EMBO J* **31**, 1379-1393 (2012).
91. P. A. Padilla, M. L. Ladage, Suspended animation, diapause and quiescence: arresting the cell cycle in C. elegans. *Cell Cycle* **11**, 1672-1679 (2012).
92. A. R. Mendenhall, B. LaRue, P. A. Padilla, Glyceraldehyde-3-phosphate dehydrogenase mediates anoxia response and survival in Caenorhabditis elegans. *Genetics* **174**, 1173-1187 (2006).
93. A. R. Mendenhall, M. G. LeBlanc, D. P. Mohan, P. A. Padilla, Reduction in ovulation or male sex phenotype increases long-term anoxia survival in a daf-16-independent manner in Caenorhabditis elegans. *Physiol Genomics* **36**, 167-178 (2009).
94. D. L. Miller, M. B. Roth, C. elegans are protected from lethal hypoxia by an embryonic diapause. *Current biology : CB* **19**, 1233-1237 (2009).
95. G. H. Fong, K. Takeda, Role and regulation of prolyl hydroxylase domain proteins. *Cell Death Differ* **15**, 635-641 (2008).
96. J. Aragones, P. Fraisl, M. Baes, P. Carmeliet, Oxygen sensors at the crossroad of metabolism. *Cell Metab* **9**, 11-22 (2009).
97. A. C. Epstein *et al.*, C. elegans EGL-9 and mammalian homologs define a family of dioxygenases that regulate HIF by prolyl hydroxylation. *Cell* **107**, 43-54 (2001).
98. R. K. Bruick, S. L. McKnight, A conserved family of prolyl-4-hydroxylases that modify HIF. *Science (New York, N.Y* **294**, 1337-1340 (2001).
99. G. L. Semenza, Regulation of oxygen homeostasis by hypoxia-inducible factor 1. *Physiology (Bethesda)* **24**, 97-106 (2009).
100. J. Fandrey, M. Gassmann, Oxygen sensing and the activation of the hypoxia inducible factor 1 (HIF-1)--invited article. *Adv Exp Med Biol* **648**, 197-206 (2009).
101. T. Hayakawa *et al.*, Regulation of anoxic death in Caenorhabditis elegans by mammalian apoptosis signal-regulating kinase (ASK) family proteins. *Genetics* **187**, 785-792 (2011).
102. B. A. Scott, M. S. Avidan, C. M. Crowder, Regulation of hypoxic death in C. elegans by the insulin/IGF receptor homolog DAF-2. *Science (New York, N.Y* **296**, 2388-2391 (2002).
103. B. L. LaRue, P. A. Padilla, Environmental and genetic preconditioning for long-term anoxia responses requires AMPK in Caenorhabditis elegans. *PloS one* **6**, e16790 (2011).
104. P. A. Padilla, T. G. Nystul, R. A. Zager, A. C. Johnson, M. B. Roth, Dephosphorylation of cell cycle-regulated proteins correlates with anoxia-induced suspended animation in Caenorhabditis elegans. *Molecular biology of the cell* **13**, 1473-1483 (2002).
105. J. Nunnari, A. Suomalainen, Mitochondria: in sickness and in health. *Cell* **148**, 1145-1159 (2012).
106. C. Darby, C. L. Cosma, J. H. Thomas, C. Manoil, Lethal paralysis of Caenorhabditis elegans by Pseudomonas aeruginosa. *Proceedings of the*

*National Academy of Sciences of the United States of America* **96**, 15202-15207 (1999).
107. H. Jiang, R. Guo, J. A. Powell-Coffman, The Caenorhabditis elegans hif-1 gene encodes a bHLH-PAS protein that is required for adaptation to hypoxia. *Proceedings of the National Academy of Sciences of the United States of America* **98**, 7916-7921 (2001).
108. C. Shen, Z. Shao, J. A. Powell-Coffman, The Caenorhabditis elegans rhy-1 gene inhibits HIF-1 hypoxia-inducible factor activity in a negative feedback loop that does not include vhl-1. *Genetics* **174**, 1205-1214 (2006).
109. Z. Shao, Y. Zhang, Q. Ye, J. N. Saldanha, J. A. Powell-Coffman, C. elegans SWAN-1 Binds to EGL-9 and regulates HIF-1-mediated resistance to the bacterial pathogen Pseudomonas aeruginosa PAO1. *PLoS Pathog* **6**, (2010).
110. N. Wiedemann, S. B. Stiller, N. Pfanner, Activation and degradation of mitofusins: two pathways regulate mitochondrial fusion by reversible ubiquitylation. *Mol Cell* **49**, 423-425 (2013).
111. L. A. Pon, Mitochondrial fission: rings around the organelle. *Current biology : CB* **23**, R279-281 (2013).
112. H. Otera, N. Ishihara, K. Mihara, New insights into the function and regulation of mitochondrial fission. *Biochim Biophys Acta* **1833**, 1256-1268 (2013).
113. G. T. Hanson *et al.*, Investigating mitochondrial redox potential with redox-sensitive green fluorescent protein indicators. *J Biol Chem* **279**, 13044-13053 (2004).
114. M. B. Cannon, S. J. Remington, Redox-sensitive green fluorescent protein: probes for dynamic intracellular redox responses. A review. *Methods Mol Biol* **476**, 51-65 (2008).
115. J. H. An, T. K. Blackwell, SKN-1 links C. elegans mesendodermal specification to a conserved oxidative stress response. *Genes Dev* **17**, 1882-1893 (2003).
116. J. Paek *et al.*, Mitochondrial SKN-1/Nrf mediates a conserved starvation response. *Cell Metab* **16**, 526-537 (2012).
117. H. Inoue *et al.*, The C. elegans p38 MAPK pathway regulates nuclear localization of the transcription factor SKN-1 in oxidative stress response. *Genes Dev* **19**, 2278-2283 (2005).
118. R. P. Oliveira *et al.*, Condition-adapted stress and longevity gene regulation by Caenorhabditis elegans SKN-1/Nrf. *Aging cell* **8**, 524-541 (2009).
119. W. Niu *et al.*, Diverse transcription factor binding features revealed by genome-wide ChIP-seq in C. elegans. *Genome research* **21**, 245-254 (2011).
120. Y. Wang, J. S. Morrow, Identification and characterization of human SLP-2, a novel homologue of stomatin (band 7.2b) present in erythrocytes and other tissues. *J Biol Chem* **275**, 8062-8071 (2000).
121. N. Tavernarakis, M. Driscoll, N. C. Kyrpides, The SPFH domain: implicated in regulating targeted protein turnover in stomatins and other membrane-associated proteins. *Trends Biochem Sci* **24**, 425-427 (1999).
122. R. Ichishita *et al.*, An RNAi screen for mitochondrial proteins required to maintain the morphology of the organelle in Caenorhabditis elegans. *J Biochem* **143**, 449-454 (2008).
123. S. Gandre, A. M. van der Bliek, Mitochondrial division in Caenorhabditis elegans. *Methods Mol Biol* **372**, 485-501 (2007).
124. H. M. Cocheme, M. P. Murphy, Complex I is the major site of mitochondrial superoxide production by paraquat. *J Biol Chem* **283**, 1786-1798 (2008).
125. N. Tavernarakis, S. L. Wang, M. Dorovkov, A. Ryazanov, M. Driscoll, Heritable and inducible genetic interference by double-stranded RNA encoded by transgenes. *Nat Genet* **24**, 180-183. (2000).

126. C. Shen, D. Nettleton, M. Jiang, S. K. Kim, J. A. Powell-Coffman, Roles of the HIF-1 hypoxia-inducible factor during hypoxia response in Caenorhabditis elegans. *The Journal of biological chemistry* **280**, 20580-20588 (2005).
127. Z. Shao, Y. Zhang, J. A. Powell-Coffman, Two distinct roles for EGL-9 in the regulation of HIF-1-mediated gene expression in Caenorhabditis elegans. *Genetics* **183**, 821-829 (2009).
128. J. M. Gray *et al.*, Oxygen sensation and social feeding mediated by a C. elegans guanylate cyclase homologue. *Nature* **430**, 317-322 (2004).
129. R. S. Branicky, W. R. Schafer, Oxygen homeostasis: how the worm adapts to variable oxygen levels. *Curr Biol* **18**, R559-560 (2008).
130. W. A. Van Voorhies, S. Ward, Genetic and environmental conditions that increase longevity in Caenorhabditis elegans decrease metabolic rate. *Proc Natl Acad Sci U S A* **96**, 11399-11403 (1999).
131. P. Hajek, A. Chomyn, G. Attardi, Identification of a novel mitochondrial complex containing mitofusin 2 and stomatin-like protein 2. *J Biol Chem* **282**, 5670-5681 (2007).
132. D. A. Christie *et al.*, Stomatin-like protein 2 binds cardiolipin and regulates mitochondrial biogenesis and function. *Mol Cell Biol* **31**, 3845-3856 (2011).
133. C. R. Hackenbrock, Ultrastructural bases for metabolically linked mechanical activity in mitochondria. I. Reversible ultrastructural changes with change in metabolic steady state in isolated liver mitochondria. *J Cell Biol* **30**, 269-297 (1966).
134. S. G. Rolland *et al.*, Impaired complex IV activity in response to loss of LRPPRC function can be compensated by mitochondrial hyperfusion. *Proceedings of the National Academy of Sciences of the United States of America* **110**, E2967-2976 (2013).
135. G. Twig *et al.*, Fission and selective fusion govern mitochondrial segregation and elimination by autophagy. *EMBO J* **27**, 433-446 (2008).
136. P. A. Parone *et al.*, Preventing mitochondrial fission impairs mitochondrial function and leads to loss of mitochondrial DNA. *PloS one* **3**, e3257 (2008).
137. G. Esposito, E. Di Schiavi, C. Bergamasco, P. Bazzicalupo, Efficient and cell specific knock-down of gene function in targeted C. elegans neurons. *Gene* **395**, 170-176 (2007).
138. T. J. Collins, ImageJ for microscopy. *BioTechniques* **43**, 25-30 (2007).
139. E. M. Jorgensen, S. E. Mango, The art and design of genetic screens: caenorhabditis elegans. *Nature reviews. Genetics* **3**, 356-369 (2002).
140. E. Smirnova, L. Griparic, D.-L. Shurland, A. M. van der Bliek, Dyanmin-related Protein Drp-1 is Required for Mitochondrial Division in Mammalian Cells. *Molecular biology of the cell* **12**, 2245-2256 (2001).
141. E. M. Hedgecock, J. G. Culotti, J. N. Thomson, L. A. Perkins, Axonal guidance mutants of Caenorhabditis elegans identified by filling sensory neurons with fluorescein dyes. *Developmental biology* **111**, 158-170 (1985).
142. P. Boontrakulpoontawee, A. J. Otsuka, Mutational analysis of the Caenorhabditis elegans ankyrin gene unc-44 demonstrates that the large spliceoform is critical for neural development. *Molecular genetics and genomics : MGG* **267**, 291-302 (2002).
143. S. Sarin, S. Prabhu, M. M. O'Meara, I. Pe'er, O. Hobert, Caenorhabditis elegans mutant allele identification by whole-genome sequencing. *Nat Methods* **5**, 865-867 (2008).

144. M. Doitsidou, R. J. Poole, S. Sarin, H. Bigelow, O. Hobert, C. elegans mutant identification with a one-step whole-genome-sequencing and SNP mapping strategy. *PloS one* **5**, e15435 (2010).
145. G. Minevich, D. S. Park, D. Blankenberg, R. J. Poole, O. Hobert, CloudMap: a cloud-based pipeline for analysis of mutant genome sequences. *Genetics* **192**, 1249-1269 (2012).
146. E. Afgan *et al.*, The Galaxy platform for accessible, reproducible and collaborative biomedical analyses: 2018 update. *Nucleic acids research* **46**, W537-w544 (2018).
147. M. Doitsidou, S. Jarriault, R. J. Poole, Next-Generation Sequencing-Based Approaches for Mutation Mapping and Identification in Caenorhabditis elegans. *Genetics* **204**, 451-474 (2016).
148. W. Maier. (https://mimodd.readthedocs.io/en/latest/index.html#, 2014-2018), vol. 2018.
149. O. Hobert. (http://hobertlab.org, 2013), vol. 2016.
150. A. Jaramillo-Lambert, A. S. Fuchsman, A. S. Fabritius, H. E. Smith, A. Golden, Rapid and Efficient Identification of Caenorhabditis elegans Legacy Mutations Using Hawaiian SNP-Based Mapping and Whole-Genome Sequencing. *G3 (Bethesda, Md.)* **5**, 1007-1019 (2015).
151. J. Bereiter-Hahn, M. Voth, Dynamics of mitochondria in living cells: shape changes, dislocations, fusion, and fission of mitochondria. *Microsc Res Tech* **27**, 198-219 (1994).
152. D. Safiulina, A. Kaasik, Energetic and Dynamic: How Mitochondria Meet Neuronal Energy Demands. *PLOS Biology* **11**, e1001755 (2014).
153. B. Westermann, Mitochondrial fusion and fission in cell life and death. *Nature reviews. Molecular cell biology* **11**, 872-884 (2010).
154. R. J. Youle, A. M. van der Bliek, Mitochondrial fission, fusion, and stress. *Science (New York, N.Y.)* **337**, 1062-1065 (2012).
155. S. Sarasija, K. R. Norman, Analysis of Mitochondrial Structure in the Body Wall Muscle of Caenorhabditis elegans. *Bio-protocol* **8**, (2018).
156. C. V. Ly, P. Verstreken, Mitochondria at the synapse. *The Neuroscientist : a review journal bringing neurobiology, neurology and psychiatry* **12**, 291-299 (2006).
157. P. J. Hollenbeck, Mitochondria and neurotransmission: evacuating the synapse. *Neuron* **47**, 331-333 (2005).
158. A. B. Knott, G. Perkins, R. Schwarzenbacher, E. Bossy-Wetzel, Mitochondrial fragmentation in neurodegeneration. *Nature Reviews Neuroscience* **9**, 505 (2008).
159. N. S. Morsci, D. H. Hall, M. Driscoll, Z. H. Sheng, Age-Related Phasic Patterns of Mitochondrial Maintenance in Adult Caenorhabditis elegans Neurons. *The Journal of neuroscience : the official journal of the Society for Neuroscience* **36**, 1373-1385 (2016).
160. K. E. Miller, M. P. Sheetz, Axonal mitochondrial transport and potential are correlated. *Journal of cell science* **117**, 2791-2804 (2004).
161. P. I. Merksamer, A. Trusina, F. R. Papa, Real-time redox measurements during endoplasmic reticulum stress reveal interlinked protein folding functions. *Cell* **135**, 933-947 (2008).